COMPARISON OF FIELD BEHAVIOR WITH RESULTS FROM NUMERICAL ANALYSIS OF A GEOSYNTHETIC REINFORCED SOIL-INTEGRATED BRIDGE SYSTEM SUBJECT TO THERMAL EFFECTS

A THESIS SUBMITTED TO THE GRADUATE DIVISION OF THE UNIVERSITY OF HAWAI'I AT MĀNOA IN PARTIAL FULFILLMENT OF THE REQUIRMENTS FOR THE DEGREE OF

MASTER OF SCIENCE

IN

CIVIL ENGINEERING

DECEMBER 2019

By

Arshia Taeb

Thesis Committee:

Phillip S.K. Ooi, Chairperson
Horst G. Brandes
Ningjun Jiang

ABSTRACT

Geosynthetic Reinforced Soil (GRS) consists of alternating layers of geosynthetic reinforcement and compacted soil. Geosynthetic Reinforced Soil – integrated bridge system (GRS-IBS) has been promoted by Federal Highway Administration (FHWA). It consists of an integral bridge superstructure and sub-structure supported on a GRS abutment. The abutment consists of a reinforced soil foundation (RSF) underlying a GRS abutment. At the ends of the superstructure are approach fills that are also geosynthetically reinforced. The main advantage of GRS abutments over traditional concrete abutment is the savings in time and cost of construction. Unlike traditional concrete abutments, GRS abutments do not require formwork and waiting time for the concrete to set. Moreover, the superstructure can be prefabricated beforehand and quickly placed on the GRS abutments leading to savings in both time and money.

Being integral bridges whereby the superstructure is structurally connected to the sub-structure GRS-IBS will undergo volume changes causing movements in the sub-structure and foundation soil during ambient temperature changes. In a previous monitoring study of a 109.5-ft-long GRS-IBS in Lahaina, Maui, a GRS-IBS was observed to undergo cyclic straining. The upper and lower reaches of the superstructure experienced the highest and lowest strain fluctuation, respectively. These non-uniform strains impose not only axial loading of the superstructure but also bending, which in turn cause the vertical pressures beneath the footing and lateral pressures behind the end walls and facing to fluctuate cyclically. Measured vertical footing pressure closest to the stream experienced the greatest daily pressure fluctuation (≈ 2,500 – 3,000 psf), while the one nearest the end wall experienced the least. The toe pressure fluctuations seem rather large. The larger these pressure fluctuations are, the greater will be the cyclic-induced deformations of the GRS abutment.

In this study, a finite element analysis of the same GRS-IBS was performed by applying an equivalent temperature and gradient to the superstructure over the coldest and hottest periods of a day to see if the field measured values of pressures are reasonable and verifiable, which indeed they were. This methodology is novel in the sense that the effects of axial load and bending of the superstructure are simulated using measured strains rather than measured temperatures. This simple methodology can be useful to engineers who are interested in estimating thermally-induced cyclic bearing pressures of GRS-IBS and the associated cyclic-induced settlement in the GRS abutment, which can purportedly be more prominent in longer span bridges.

FHWA currently suggests limiting the span length of GRS-IBS to 140 ft. This is because it is generally believed that the longer the span length, the more severe the thermal effects will be on the sub-structure behavior and GRS abutment settlement. With modifications to the material and geometric properties of the same GRS-IBS model, the behavior of a bridge that is twice as long was studied. After being subject to temperature loading the average bearing pressures of the 220-ft-long bridge remained within its shakedown limit. The results of this study showed that a GRS abutment is capable of supporting superstructures with a longer span than previously envisioned.

ACKNOWLEDGEMENTS

The author would like to thank the State of Hawaii Department of Transportation (HDOT) for its financial support in cooperation with the Federal Highway Administration (FHWA). The author would also like to thank KSF, Inc. in particular Dr. Harold Hamada and Mr. David Fujiwara, for developing the structural model. Advice and consultation provided by Professor Ooi throughout the entire investigation is greatly appreciated.

The author acknowledges Dr. Ahad Kolahi of LUSAS for help in troubleshooting the many finite element runs. The review of this work by my thesis committee consisting of professors Phillip Ooi, Horst Brandes, and Ningjun Jiang is most greatly appreciated.

Table of Contents

List of Figures

List of Tables

1 INTRODUCTION

1.1 Overview

According to the Federal Highway Administration (FHWA), many regions do not have enough funds to repair and replace more than 60,000 bridges that are suffering from functional and structural deficiency (Adams et al., 2011). Thus, a more cost-efficient bridge construction technology seems necessary, as bridges and roadways are integral pieces of infrastructure that every community relies on.

Geosynthetic Reinforced Soil (GRS) was first used for building retaining walls for roads by the United States Forest Service in 1970s. Since then, GRS technology has been used in a variety of engineering and earth work applications (Adams 2011). Geosynthetic Reinforced Soil-Integrated Bridge System (GRS-IBS) was developed by FHWA's Turner-Fairbank Highway Research Center, which promoted the technology through its Every Day Counts (EDC) program in 2011 (Alzamora, 2018). GRS-IBS is an accelerated method of bridge construction which consists of a reinforced soil foundation (RSF), a GRS abutment, and an integrated approach which connects to the superstructure (Lawrence 2014). As Adams describes, the abutment uses a 1-2-3 process that includes: "(1) a row of facing blocks, (2) a layer of compacted granular fill, and (3) a layer of geosynthetic reinforcement. The 1-2-3 process is repeated until the required abutment height is reached" (Adams 2011). A typical GRS-IBS is shown in Figure1. In a GRS-IBS, the superstructure is usually integral with the substructure.

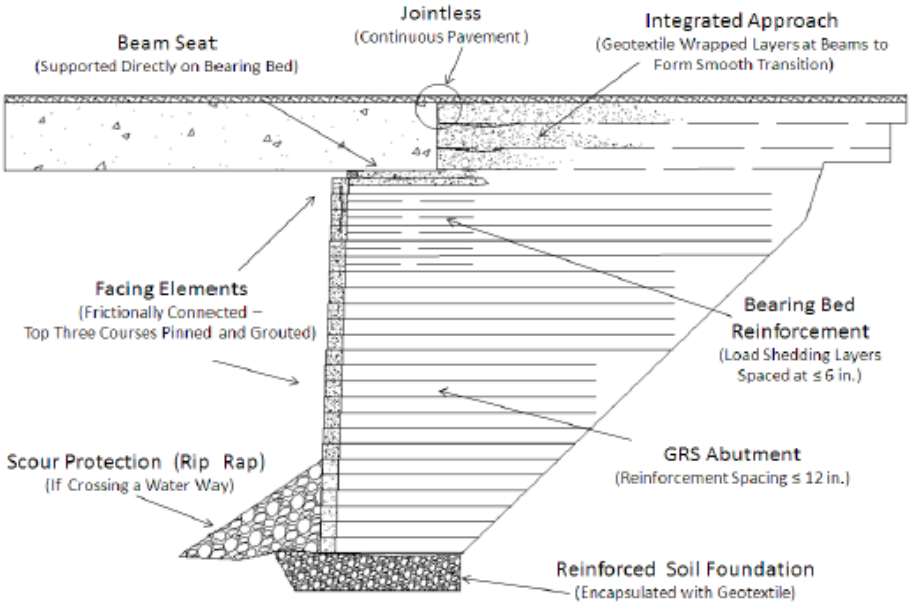

Figure 1 Typical GRS-IBS section

1.2 Benefits of GRS IBS

Advantages of GRS-IBS include cost efficiency, construction speed, wide availability of material and usage variety. Since the facing element is not a structural element, the user can choose between a variety of materials such as concrete, timber, rock, automobile tires, gabion baskets, etc. (Adams et al.2011). There are more requirements for the GRS backfill since it is an important structural element. The backfill should be hard and durable granular particles that can be compacted easily, drain and workable. Most state transportation departments have aggregate specifications that meet these requirements, and in most cases, these aggregates can be found in the local area (Adams et al. 2011). Construction cost and speed are two major factors of a successful engineering project. According to the St. Lawrence County Department of Highways in New York, GRS-IBS has reduced the cost by 50% and shortened the construction duration by 5 to 6 weeks (Alzamora, 2018). These cost and time reductions have been reported in almost all regions using GRS-IBS. This technology has also been designed and constructed for a variety of loading and usage conditions. It was designed for use in low volume roads as well as bridges with average daily traffic (ADT) of 2,000 to 34,000. GRS-IBS has also been designed and constructed over streams and rail roads which typically require higher embankments and longer span lengths and in regions of high seismicity such as Utah, Puerto Rico and Hawaii (Alzamora, 2018).

1.3 Objective

Since the superstructure is integral with the substructure in a GRS-IBS, substructure behavior is influenced by thermal effects as discussed by Ooi et al. (2019a and 2019b). Ooi et al. (2019b) showed that the vertical bearing stress daily fluctuation in the footing of the first GRS-IBS in Hawaii located in Lahaina, Maui fluctuated by as much as 2,500 to 3,000 psf from peak-to-trough. This thesis aims to mimic the field behavior through numerical modeling. Specifically, the objectives of this research project include:

a. Perform a literature review on the effects of confining stress on the stiffness of geosynthetic reinforcement in granular fills, an important input parameter in numerical analysis.
b. Perform a Finite Element (FE) analysis of the GRS-IBS in Lahaina, Maui, to investigate thermal effects on the bridge behavior.
c. Compare the FE results to the field data.
d. Analyze the effects of variation of bridge span length on the bearing pressure fluctuation in a similar GRS abutment due to thermal effects.

1.4 Thesis Organization

The organization of this report is as follows:

- Chapter 2 includes a literature reviews on: 1) the effects of confining pressure on geosynthetic reinforcement, 2) the constitutive model that will be used in the FE analysis, and 3) effects of repeated loading on granular soils.

- Chapter 3 describes the GRS-IBS construction sequence and contains a description of the instrumentation used and the data collected.
- Chapter 4 describes the finite element analysis conducted with all the material properties, boundary conditions and loadings.
- Chapter 5 discusses the results of the finite element analysis and comparison to the field data.
- Chapter 6 presents the results of an investigation of bridge span length on the bearing pressure fluctuation.
- Chapter 7 contains a summary of the report with conclusions and recommendations for future studies.
- The Appendix contains boring logs at site of the bridge studied and the data sheet for the geotextile used.

2 LITERATURE REVIEW

2.1 Effects of Confining Pressure on Geotextile Stiffness

In modeling a GRS-IBS using numerical analysis, the geosynthetic reinforcement stiffness is usually determined by an unconfined or "in-air" wide width tensile test. A geotextile with a wide width is necessary for testing because geotextiles tend to neck down if narrow strips are tested. ASTM standard such as ASTM D4595 do not require the geotextile to be tested under a confining stress. However, Christopher et al. (1986) showed that geotextiles have different stress-strain properties when confined (Christopher et al., 1986). A summary of several publications that investigate the effects of confinement on the stiffness of geotextiles is provided below.

2.1.1 McGown et al. (1982)

Since the 1980s, there have been tests conducted by several researchers to determine the effects of confining pressure on the in-soil stiffness of geotextile. In 1982, McGown et al. developed an in-soil test apparatus which places the geotextile sample between two layers of soil and the confining pressure is applied using rubber pressure bellows on either side of the sample (Figure 2). The bellows can be pressurized to a maximum stress of 250 kN/m^2 (5221 psf). The fabrics tested by McGown et al. (1982) are shown in Table 1. Lotrack 16/15 was the only woven geotextile tested and in comparison, to the other three non-woven fabrics, it had an insignificant increase in stress-strain curve gradient due to increasing confining pressure (Figure 3).

Table 1 McGown et al.'s (1982) geotextile samples tested

Characteristic	Lotrak 16/15	Terram 1000	BIDIM U24	Propex 6067
Method of Construction	Woven tapes	Non-woven melt bonded filaments	Non-woven needle punched filaments	Composite Woven and needle punched
Polymer(s) Composition	100% Polypropylene	67% Polypropylene 33% Polyethylene	100% Polyester	100% Polypropylene
Specific Gravity	0.91	0.9	1.39	0.91
Weight/Unit Area(g/m^2)	120	140	210	650
Nominal Thickness (mm)	0.3	0.7	1.9	3.5

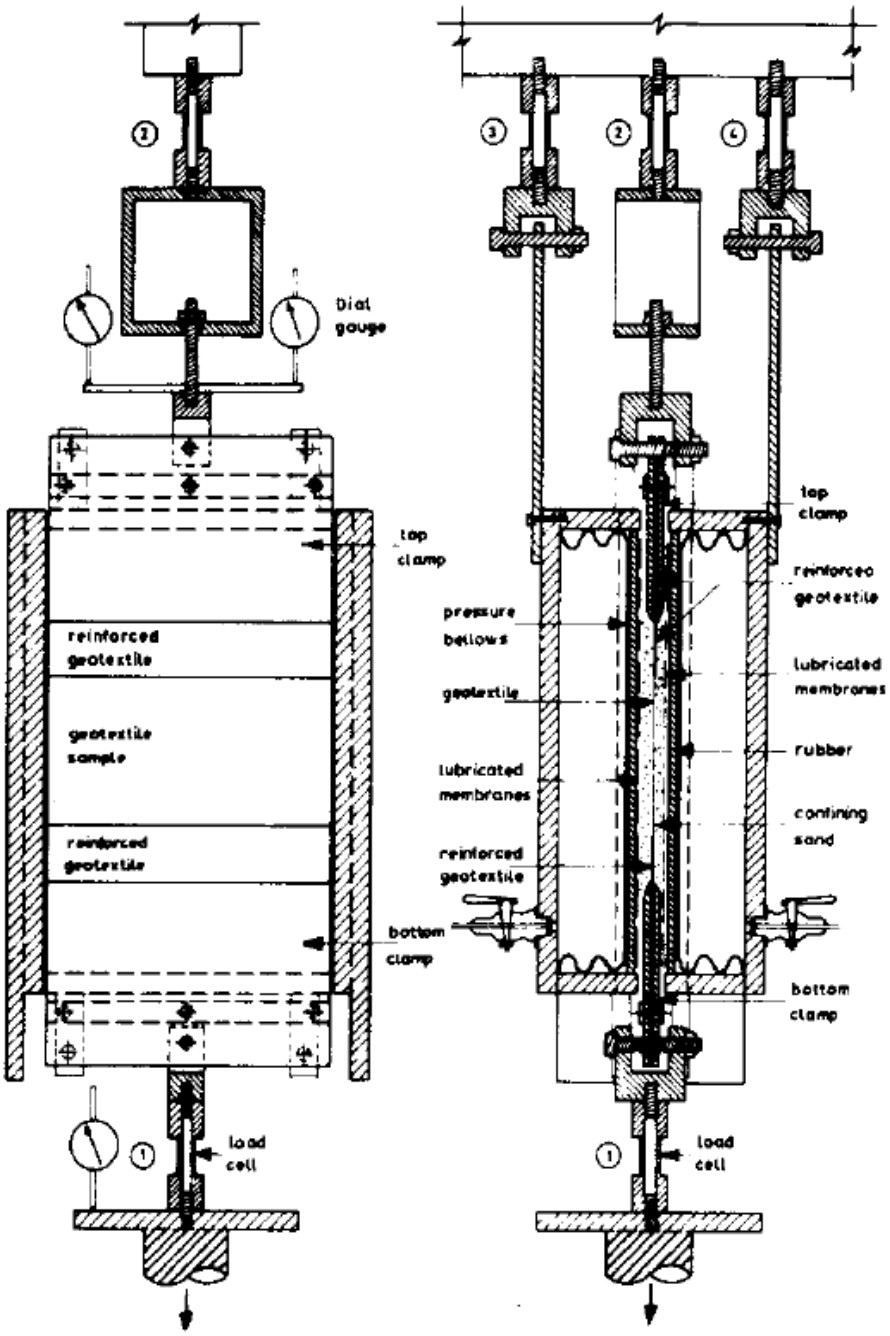

Figure 2 McGown et al.'s (1982) in-soil test apparatus

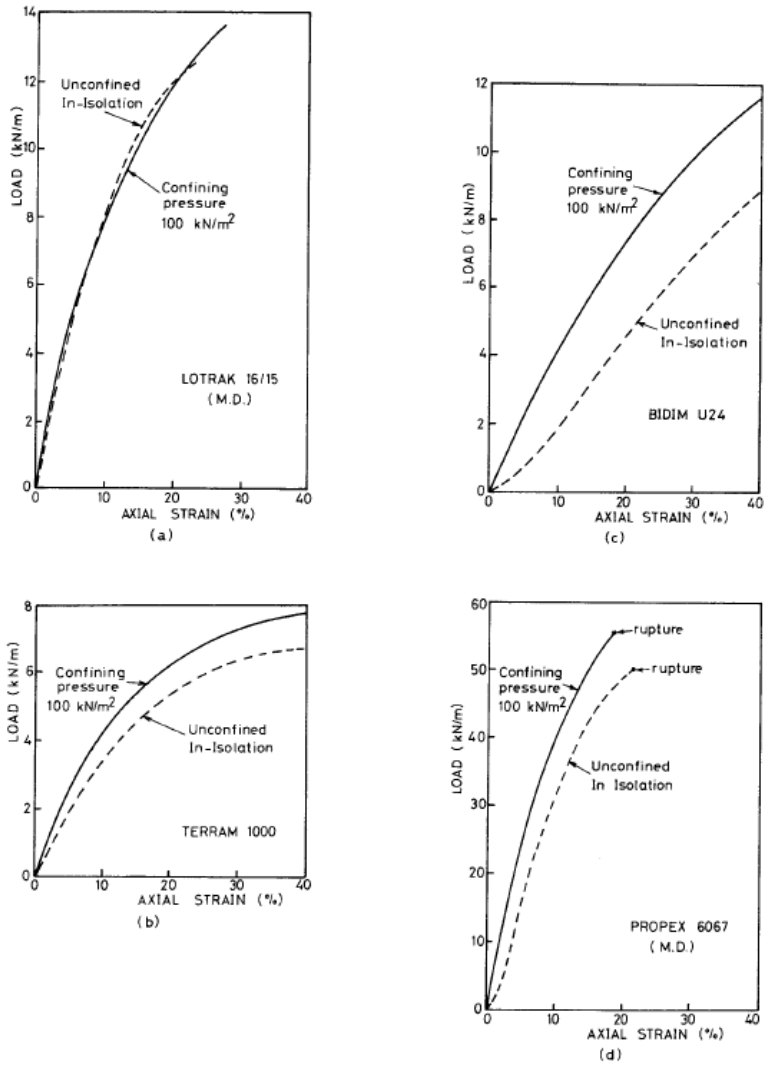

Figure 3 McGown et al.'s (1982) in soil test results

2.1.2 Christopher et al. (1986)

In 1986, Christopher et al. developed a zero-span confined tension test to simulate the effects of soil confinement on geotextiles. The test set up consists of a set of pneumatic tension clamps that are air regulated to control the clamping pressure on the sample (Figure 4). "The test procedure consists of centering a 75 mm by 75 mm specimen between the clamps, with clamps placed at zero gage length" (Christopher et al., 1986). Tests were conducted on three samples: 1. A polypropylene continuous filament needle punched non-woven, with a unit weight of 280 gm/m^2; 2. A polyester spunbonded needle punched non-woven, with a unit weight of 238 gm/m^2; and 3. A polypropylene slit film woven with a unit weight of 215 gm/m^2. As with the McGown et al. (1982) study, the woven geotextile experienced the least amount of change in stiffness between in-air and in-confinement values (Figure 5).

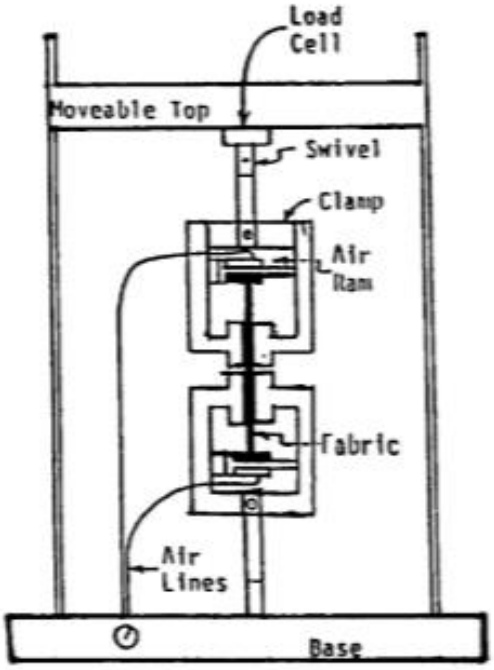

Figure 4 Christopher et al.'s (1986) zero-span tension apparatus

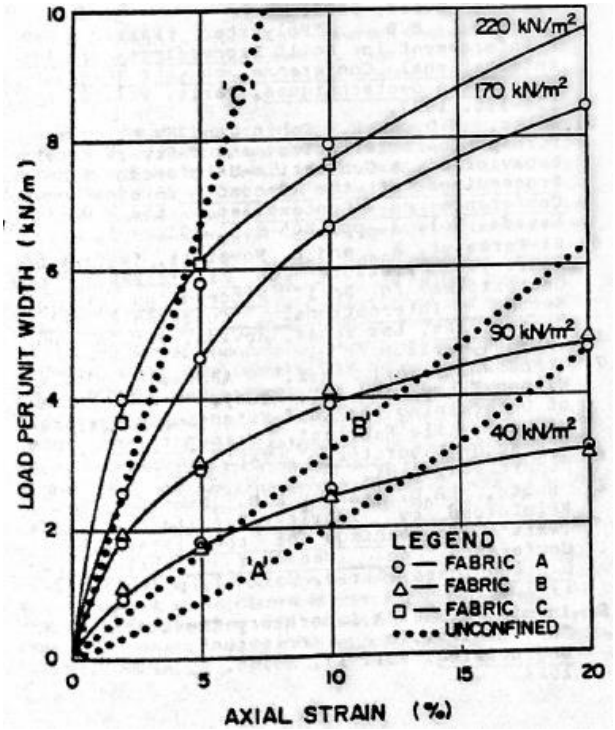

Figure 5 Christopher et al.'s (1986) tension test results

2.1.3 Kokkalis and Papacharisis (1989)

Kokkalis and Papacharisis (1989) developed a modified shear box apparatus to test the behavior of geotextile samples. The reasons for using a modified shear box include: 1. Simplicity in operation and in any required modification to the geotextile specimen in the box; 2. Inherent potential to apply any normal pressure on the geotextile through soil layers; and 3. Availability of shear box in most soil and road laboratories (Kokkalis and Papacharisis, 1989). The modifications applied to the shear box and the test results are shown in figures 6 and 7, respectively. All the geotextiles used in this test are non-woven (Table 2).

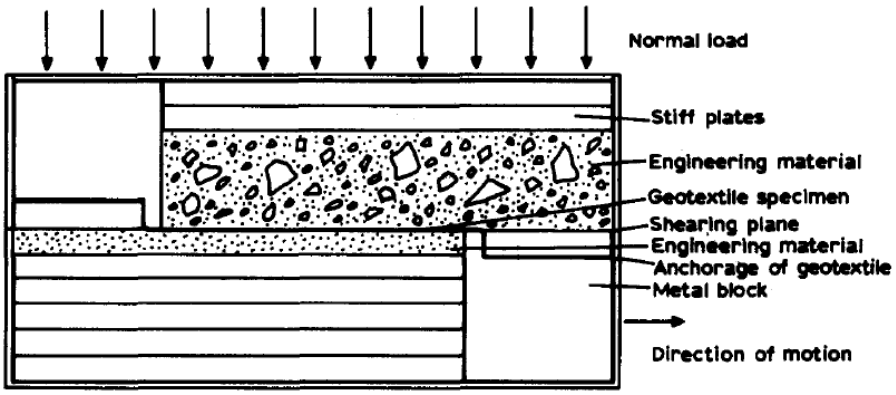

Figure 6: Kokkalis and Papacharisis' (1989) modified shear box

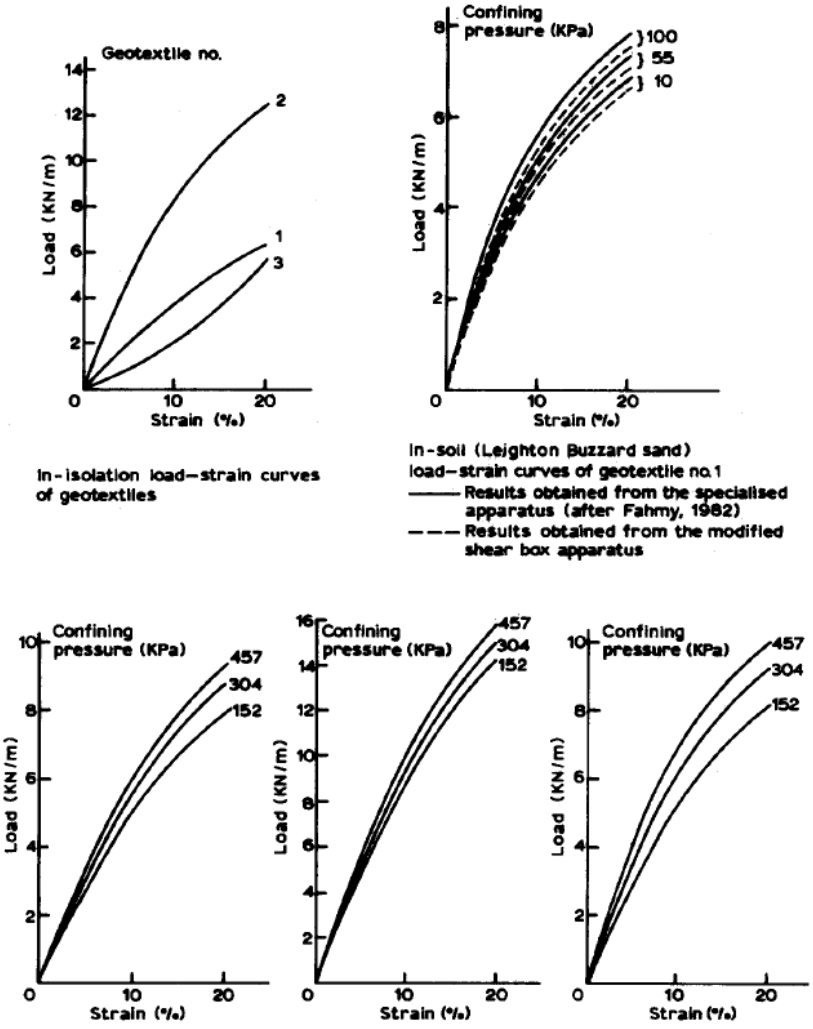

Figure 7 Kokkalis and Papacharisis' (1989) shear box test results

Table 2 Kokkalis and Papacharisis' (1989) geotextile characteristics

Composition	Type of Construction	Unit weight (g/m^2)	Thickness (mm)	Identification number
67% polypropylene+33% polyethylene	Non-woven Melt-bonded	140	0.7	1
67% polypropylene+33% polyethylene	Non-woven Melt-bonded	230	1.0	2
100% polyester	Non-woven Needle-punched	270	2.3	3

2.1.4 Ling et al. (1991)

Ling et al. (1991) designed an apparatus to measure the strength and deformation characteristics of geotextiles under unconfined conditions, when confined with a rubber membrane, and when confined with soil. Figure 8 shows the apparatus that connects to the loading machine for testing and the configuration of the geotextile specimen within the test apparatus. Ling et al. (1991) tested three specimens manufactured using different bonding processes as summarized in Table 3. Figure 9 shows the load per unit width-strain relationships for the three fabrics tested.

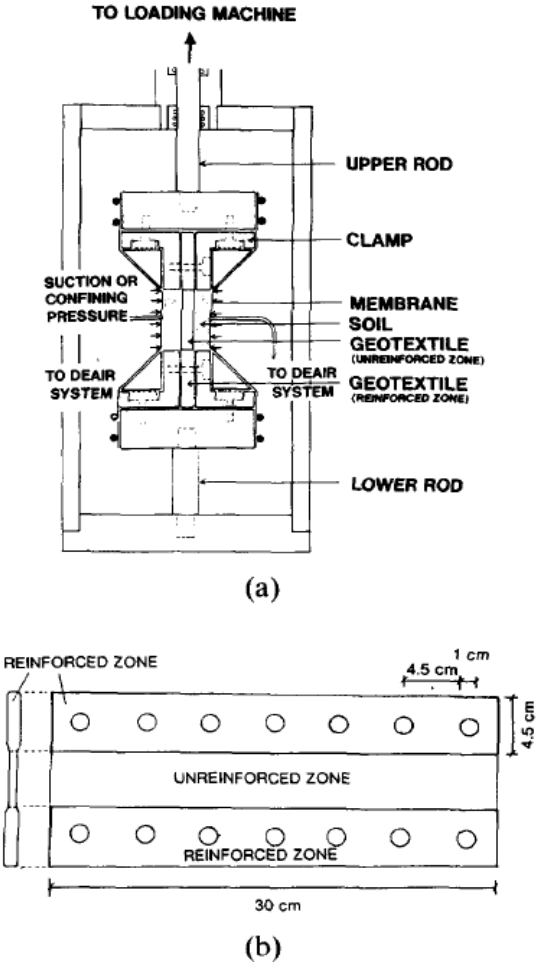

Figure 8 a) Ling et al.'s (1991) tension test apparatus, b) configuration of geotextile within the apparatus

Table 3 Ling et al.'s (1991) geotextile sample properties

Geotextile	Composition	Bonding Process	Unit weight (g/m^2)	Thickness (mm)
Bidim b5	Polyester	Non-woven Needle-punched	235	3
Tafnel R-90k	Polypropylene	Non-woven Spun-bonded	300	3
Typar	Polypropylene	Non-woven Heat-bonded	105	0.5

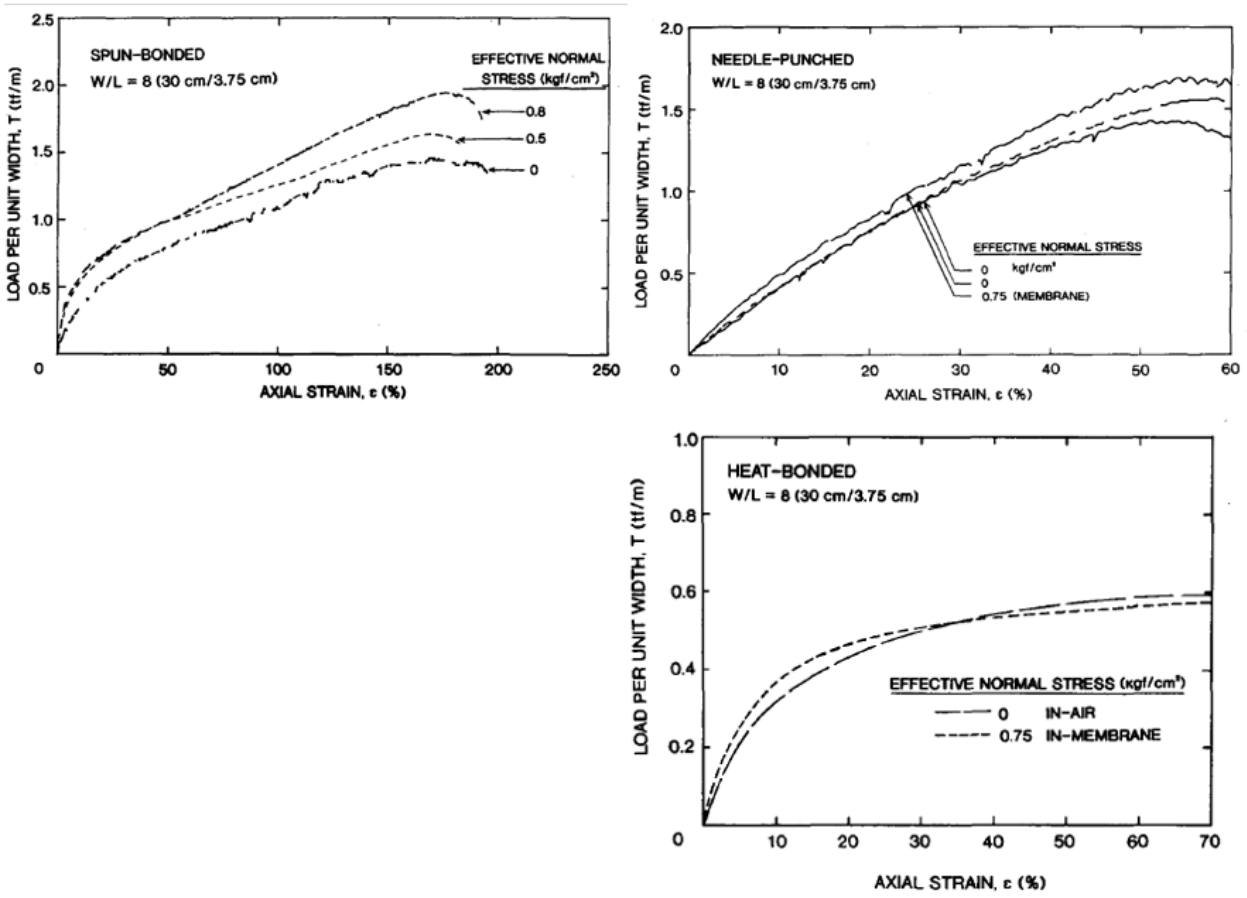

Figure 9 Ling et al.'s (1991) tension test results

A summary plot of all the geotextile stiffness at 5% strain is shown in Figure 10. The test results clearly show an increase in stiffness with confining pressure in non-woven geotextiles. However, due to a lack of woven geotextile test data and since it is not known how much of the increase in stiffness is due to friction between the geotextile and the confining medium, the effect of confining pressure on geotextile is not considered for this project.

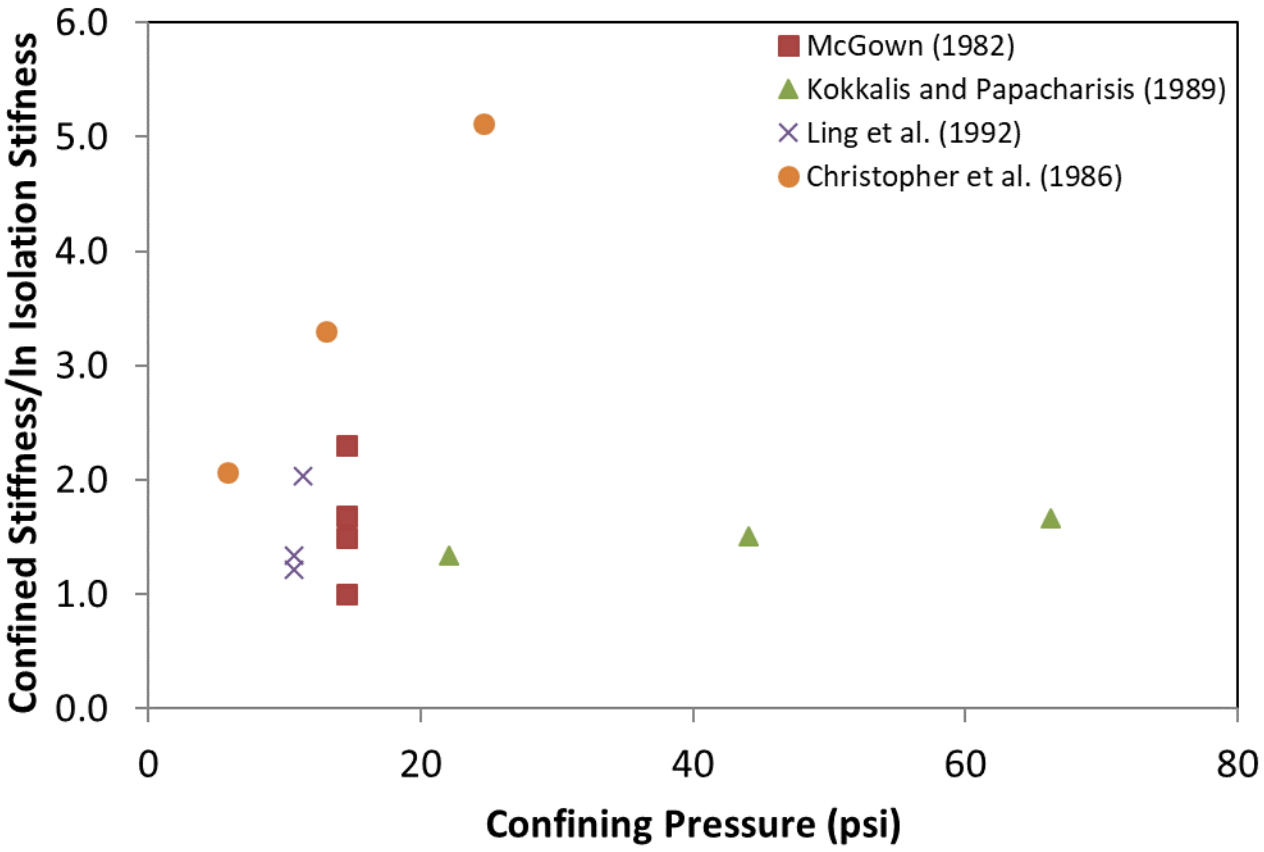

Figure 10 Summary of confining pressure effects on geotextile stiffness

2.2 Constitutive Soil Model

In this research, the finite element software LUSAS (2016) which stands for London University Structural Analysis System, was used to model the bridge behavior. In LUSAS, the soil's stress strain behavior was modeled using the Mohr-Coulomb model. The Mohr-Coulomb model parameters can be easily related to those from the Duncan and Chang (1970) model. A description of both models is provided in this section.

2.2.1 Mohr-Coulomb Model

The Mohr-Coulomb model (MC) uses the Mohr-Coulomb failure criterion to determine the stress conditions of the material upon failure. The MC model assumes an elastic-perfectly plastic material whereby the material will behave elastically until a critical stress or yield stress is reached, after which the material behaves perfectly plastically when failure occurs. Figure 11 shows the stress-strain behavior. In Figure 11, ε^e and ε^p denote the elastic and plastic strains, respectively. A yield function (f) is required to determine if the material has yielded (LUSAS, 2016) as follows where τ is the shear stress, σ_n is the normal stress, c is the cohesion and ϕ is the friction angle of the soil.

$$f = \tau - (c + \sigma_n \tan\phi) = 0 \quad (1)$$

The yield function can also be expressed in terms of the second deviator stress invariant, J_2, and the Lode angle, θ, as follows (LUSAS, 2016):

$$f = \sigma_n \sin\phi + J_2^{½}[\cos\theta - \frac{1}{\sqrt{3}} \sin\theta \cos\phi] - c\cos\phi \quad (2)$$

where,

$$J_2 = \frac{1}{6}[(\sigma_1 - \sigma_2)^2 + (\sigma_2 - \sigma_3)^2 + (\sigma_3 - \sigma_1)^2] \quad (3)$$

and

$$\theta = \tan^{-1}[\frac{1}{\sqrt{3}}(2\frac{\sigma_2 - \sigma_3}{\sigma_1 - \sigma_3} - 1)] \quad (4)$$

J_2 "provides a measure of the distance of the current stress state from the space diagonal in the deviatoric plane and θ defines the orientation of the stress state within this plane" (Potts et al., 1999). A plastic potential function (g) is used to estimate the relative magnitude of the plastic strain increment. In PLAXIS (2014), g is expressed as follows in which ψ is the dilatancy angle of the soil.

$$g = r - s\sin\psi - c\cos\psi \quad (5)$$

where r = radius of Mohr circle at the current stress state and s = distance of center of Mohr circle to the origin.

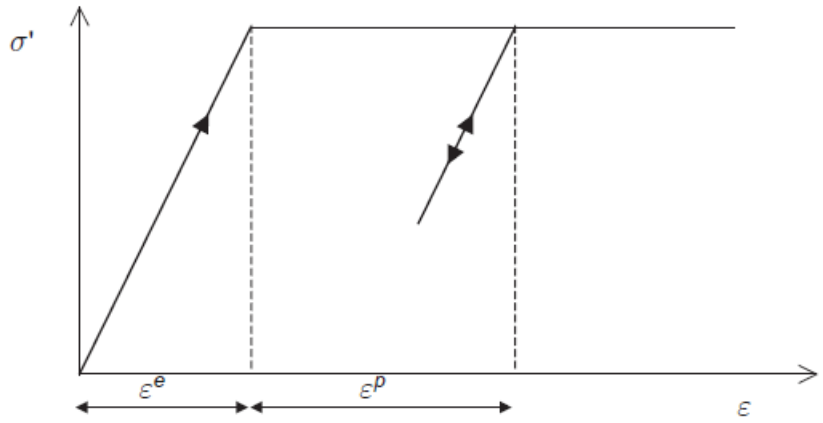

Figure 11 Elastic-perfectly plastic stress-strain behavior.

However, LUSAS does not provide any expression for g nor does it describe the stress-strain and volume change behavior in detail. In PLAXIS, the yield function has a similar form as the plastic potential function except that the friction angle replaces the angle of dilation as shown in Equation 5. The plastic potential function in LUSAS should also be different than the yield function because an angle of dilation must be specified. When the yield and plastic potential functions are dissimilar, the plasticity is non-associated.

The volume change behavior can be divided into two parts. At stresses below the yield strength, the material behaves elastically. During this phase, the material compresses and the volumetric strain is related to the axial strain as follows:

$$\frac{\varepsilon_v}{\varepsilon_a} = 1 - 2\upsilon \tag{6}$$

After the yield stress is reached, the material behaves plastically and the slope of the volumetric strain vs axial strain (tan α) can be estimated as follows:

$$\tan\alpha = \frac{2\sin\psi}{1-\sin\psi} \tag{7}$$

To check if the Mohr-Coulomb formulation in LUSAS is consistent with Equations 6 and 7, a simple drained triaxial test with a confining pressure of 2000 psf was simulated using an axi-symmetric soil configuration with a height of 1 ft and a radius of 1 ft. The vertical axis of symmetry and the bottom of the sample are on rollers. The results of the simulation are compared to hand calculations in Figure 12. It can be seen that the stress-strain and volume change behavior of the MC material in LUSAS agrees quite well with hand calculations with a small discrepancy in the volume change behavior when the soil dilates. In Figure 12, E_{50} and υ are the Young's modulus at 50% of the yield stress and Poisson's ratio, respectively, of the soil.

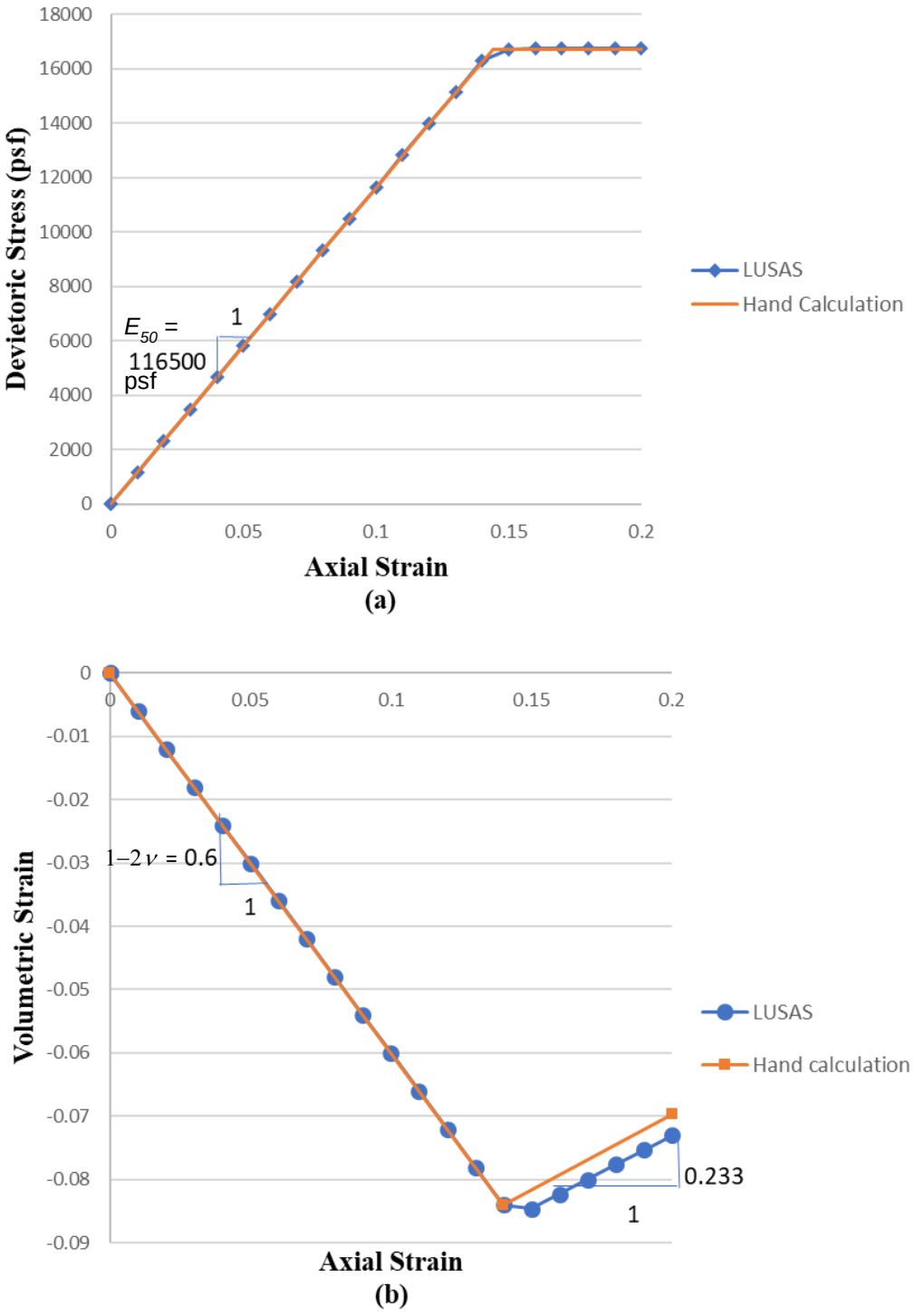

Figure 12 LUSAS and hand calculation comparison of (a) stress-strain and (b) volumetric change of Mohr-Coulomb material

2.2.2 Duncan-Chang (1970) Hyperbolic Model

The MC model provides a simple bi-linear approximation of a soil's stress-strain behavior but in reality, the actual behavior is highly nonlinear. Duncan and Chang (1970) proposed the use of a hyperbolic function to model soil nonlinearity (Figure 13) where q = deviator stress, σ_1 and σ_3 are the major and minor principal stresses, respectively and ε is the axial strain. Constants a and b are related to the initial tangent modulus (E_i) and the deviator stress at failure, q_f, respectively.

$$q = (\sigma_1 - \sigma_3) = \frac{\varepsilon}{a+b\varepsilon} \tag{8}$$

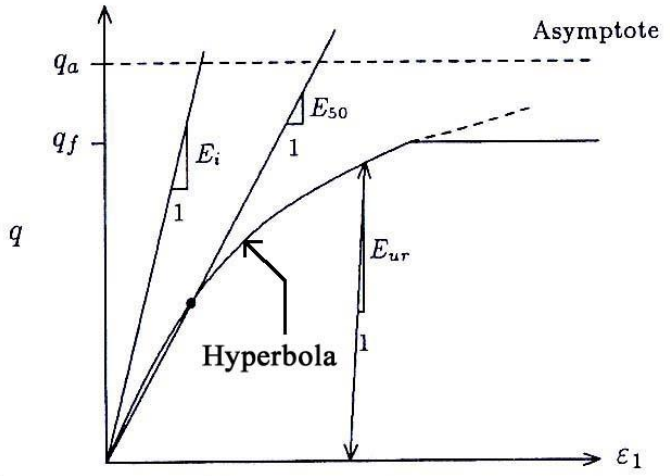

Figure 13 Hyperbolic stress-strain curve (PLAXIS, 2014)

In the Duncan-Chang (1970) model, E_i is related to the confining pressure, σ_3, as follows:

$$E_i = k\, p_a\, (\sigma_3 / p_a)^{\,n} \tag{9}$$

where k = modulus number and n = modulus exponent. Values of k and n have been widely publicized for a variety of soil types and values of relative compaction (Table 4). The Mohr-Coulomb E_{50} is commonly assumed to be one half of E_i.

Table 4 Hyperbolic soil parameters k and n as a function of soil type and relative compaction (Duncan et al., 1980)

Unified Classification	RC Stand. AASHTO	γ_m k/ft³	ϕ_o deg	$\Delta\phi$ deg	C k/ft²	k	n	R_f	K_b	m
GW, GP SW, SP	105	0.150	42	9	0	600	0.4	0.7	175	0.2
	100	0.145	39	7	0	450	0.4	0.7	125	0.2
	95	0.140	36	5	0	300	0.4	0.7	75	0.2
	90	0.135	33	3	0	200	0.4	0.7	50	0.2
SM	100	0.135	36	8	0	600	0.25	0.7	450	0.0
	95	0.130	34	6	0	450	0.25	0.7	350	0.0
	90	0.125	32	4	0	300	0.25	0.7	250	0.0
	85	0.120	30	2	0	150	0.25	0.7	150	0.0
SM-SC	100	0.135	33	0	0.5	400	0.6	0.7	200	0.5
	95	0.130	33	0	0.4	200	0.6	0.7	100	0.5
	90	0.125	33	0	0.3	150	0.6	0.7	75	0.5
	85	0.120	33	0	0.2	100	0.6	0.7	50	0.5
CL	100	0.135	30	0	0.4	150	0.45	0.7	140	0.2
	95	0.130	30	0	0.3	120	0.45	0.7	110	0.2
	90	0.125	30	0	0.2	90	0.45	0.7	80	0.2
	85	0.120	30	0	0.1	60	0.45	0.7	50	0.2

2.3 Repeated Loading of Granular Soils

This topic is relevant to this research because cyclic loading of the GRS backfill was observed during field monitoring. When an unbounded granular material (UGM) is subjected to repeated loading, it typically experiences two types of strains: 1. A recoverable (resilient) strain; and 2. An irrecoverable (permanent) strain. According to Werkmeister (2003) "the resilient deformation is mainly attributable to the deformation of the individual grains. On the other hand, permanent deformation is primarily due to particle re-orientation."

According to shakedown theory (Werkmeister, 2003), at low deviator stress, a UGM will experience resilient deformation after a large number of load applications. At high deviator stress, the UGM will experience permanent deformation (PD) that continues to increase until failure or collapse occurs. These two responses imply that there must exist a limiting stress below which the material experiences only resilient deformation. This is referred to as the plastic shakedown limit (Werkmeister, 2003).

Based on these observations, Werkmeister (2003) defined three ranges of PD behavior of UGMs. They are:

Range A: Plastic shakedown is the range where the applied load is smaller than the plastic shakedown limit and PD approaches a constant value as the number of load cycles increase. At this range the deformation becomes entirely resilient. This is a desired range for UGMs.

Range C: Incremental collapse is the range in which the applied load is too high, and the material fails quickly. This situation should be avoided in design.

Range B: Plastic creep is between incremental collapse and shakedown. In this range, the applied load is larger than the plastic shakedown limit but smaller than the plastic creep limit. The material will eventually fail at large number of cycles.

In 2010, Song and Ooi (2010) performed single-stage PD testing on a virgin aggregate (VA) which is a crushed Type B basalt from Makakilo on the island of Oahu, Hawaii. Figure 14 shows the results of these tests. It is clear that the material shakes down at deviator stresses of 210 kPa (4380 psf) or less. Figure 14 is relevant to this research as will be discussed later.

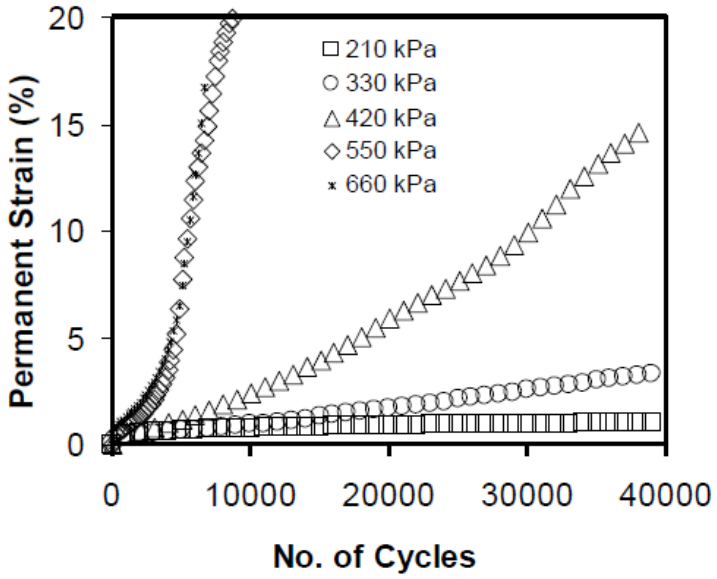

Figure 14 Single-stage permanent deformation test results for a basalt aggregate from Makakilo, Hawaii

3 KAUAULA STREAM BRIDGE PROJECT

3.1 Project Overview

The 109.5–ft-long single-span Kauaula Stream Bridge was completed in 2013 and is part of the Lahaina bypass road in Lahaina, Maui (Figure 15). The bridge is skewed (31°), super elevated (4%) and has a 0.5% downward slope from Abutment 1 to Abutment 2 (Figure 16). The tub girders are connected by precast planks that are smoothed over with a concrete topping. As an integrated system, the superstructure and end wall are integral with the concrete footing (Lawrence, 2014). This integration creates a full moment connection between the superstructure and the sub-structure. During construction, instruments including earth pressure cells (EP), fatbacks (FB), inclinometers (I), and strain gages (SG) were installed to monitor the behavior of the GRS-IBS.

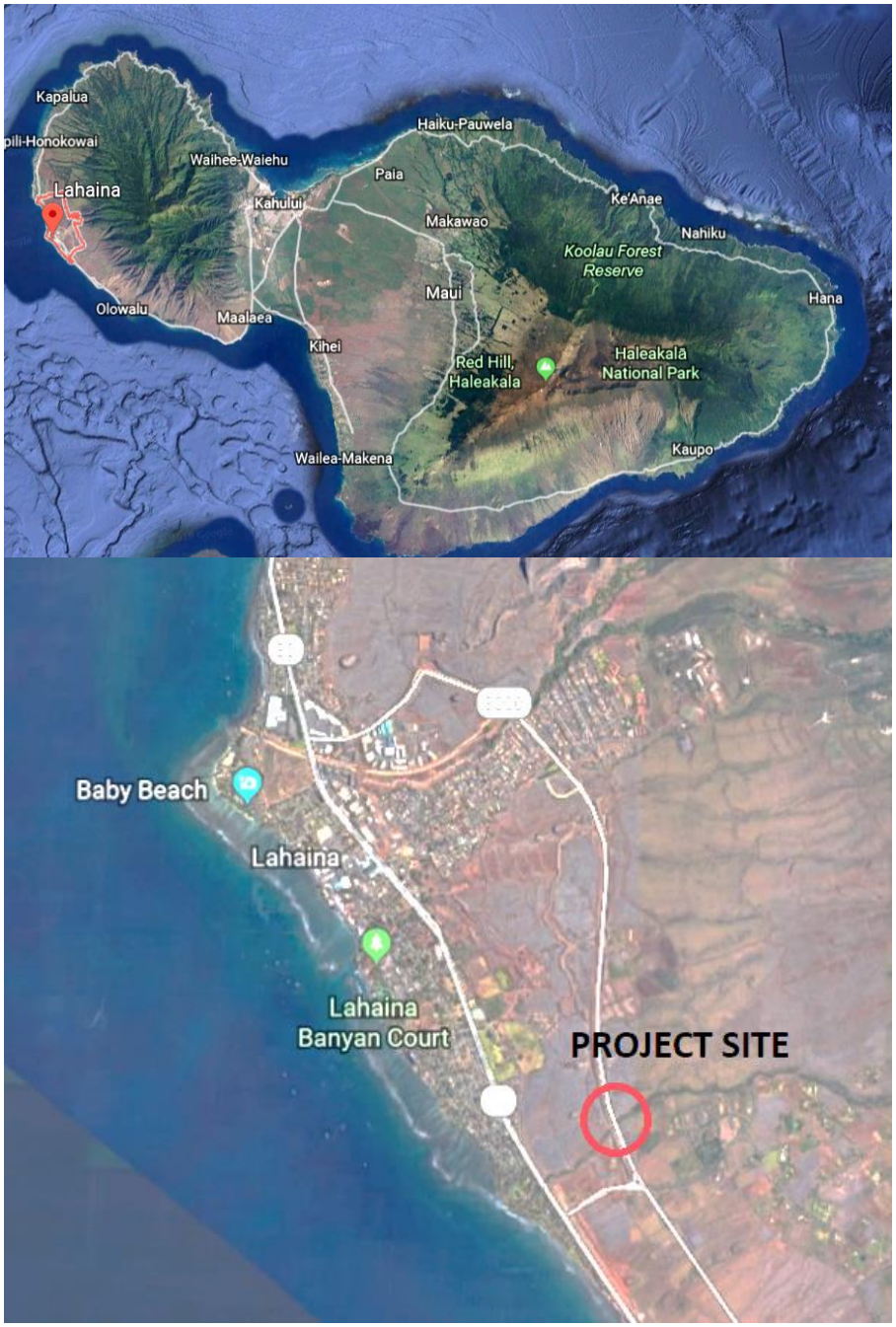

Figure 15 Location of Kauaula Stream bridge

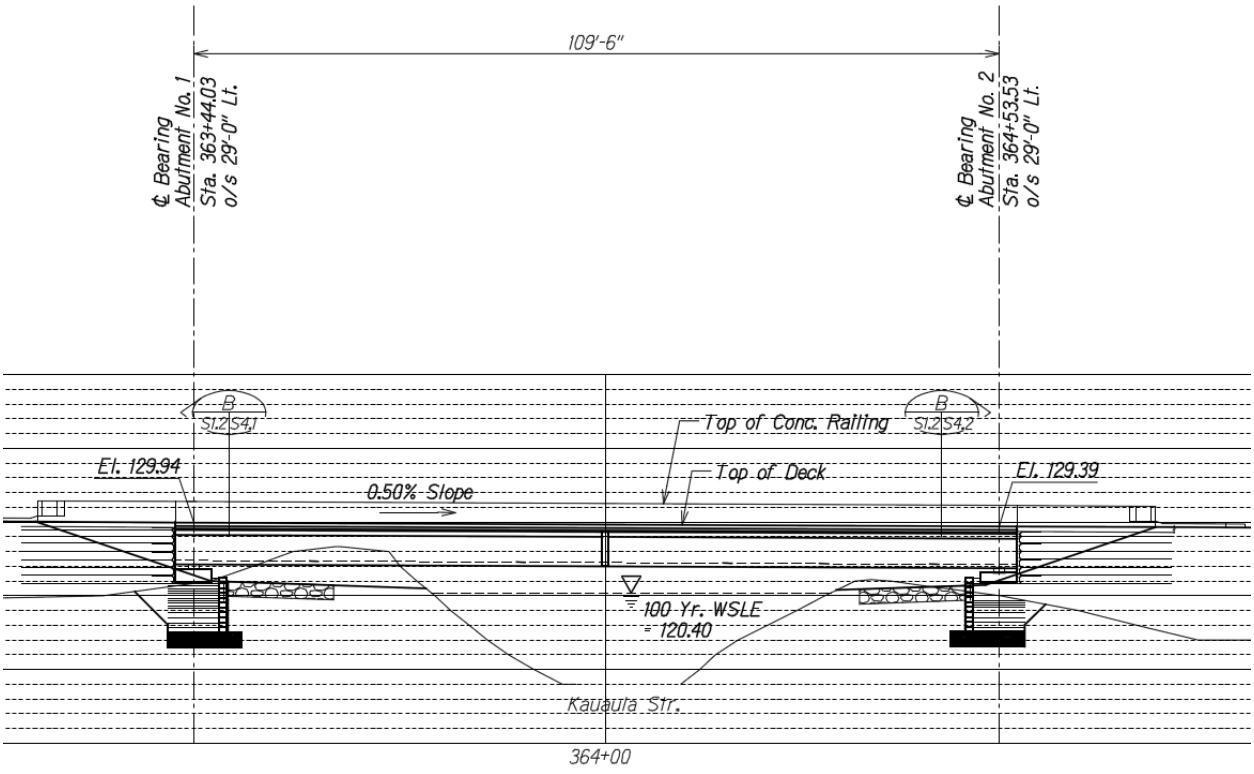
109'-6"
℄ Bearing
Abutment No. 1
Sta. 363+44.03
o/s 29'-0" Lt.
℄ Bearing
Abutment No. 2
Sta. 364+53.53
o/s 29'-0" Lt.
B
S1.2 S4.1
Top of Conc. Railing
B
S1.2 S4.2
El. 129.94
0.50% Slope
Top of Deck
El. 129.39
100 Yr. WSLE
= 120.40
Kauaula Str.
364+00

(a)

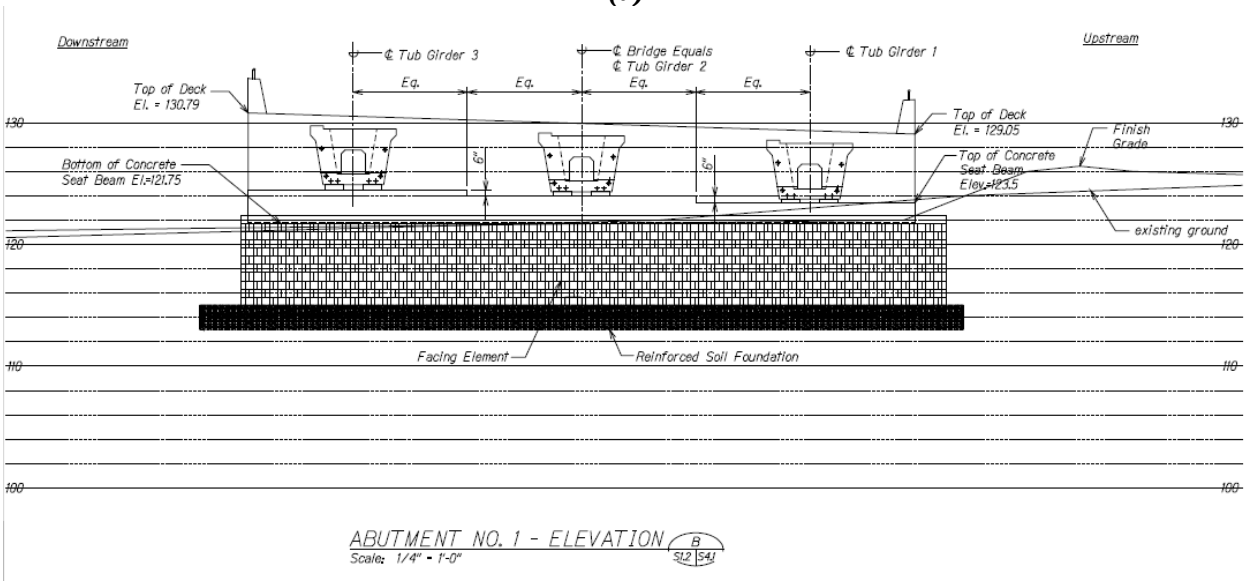
Downstream
Upstream
℄ Tub Girder 3
℄ Bridge Equals
℄ Tub Girder 2
℄ Tub Girder 1
Eq.
Eq.
Eq.
Eq.
Top of Deck
El. = 130.79
Top of Deck
El. = 129.05
Finish
Grade
Bottom of Concrete
Seat Beam El.=121.75
Top of Concrete
Seat Beam
Elev.=123.5
existing ground
130
120
110
100
Facing Element
Reinforced Soil Foundation
ABUTMENT NO. 1 - ELEVATION
Scale: 1/4" = 1'-0"
B
S1.2 S4.1

(b)

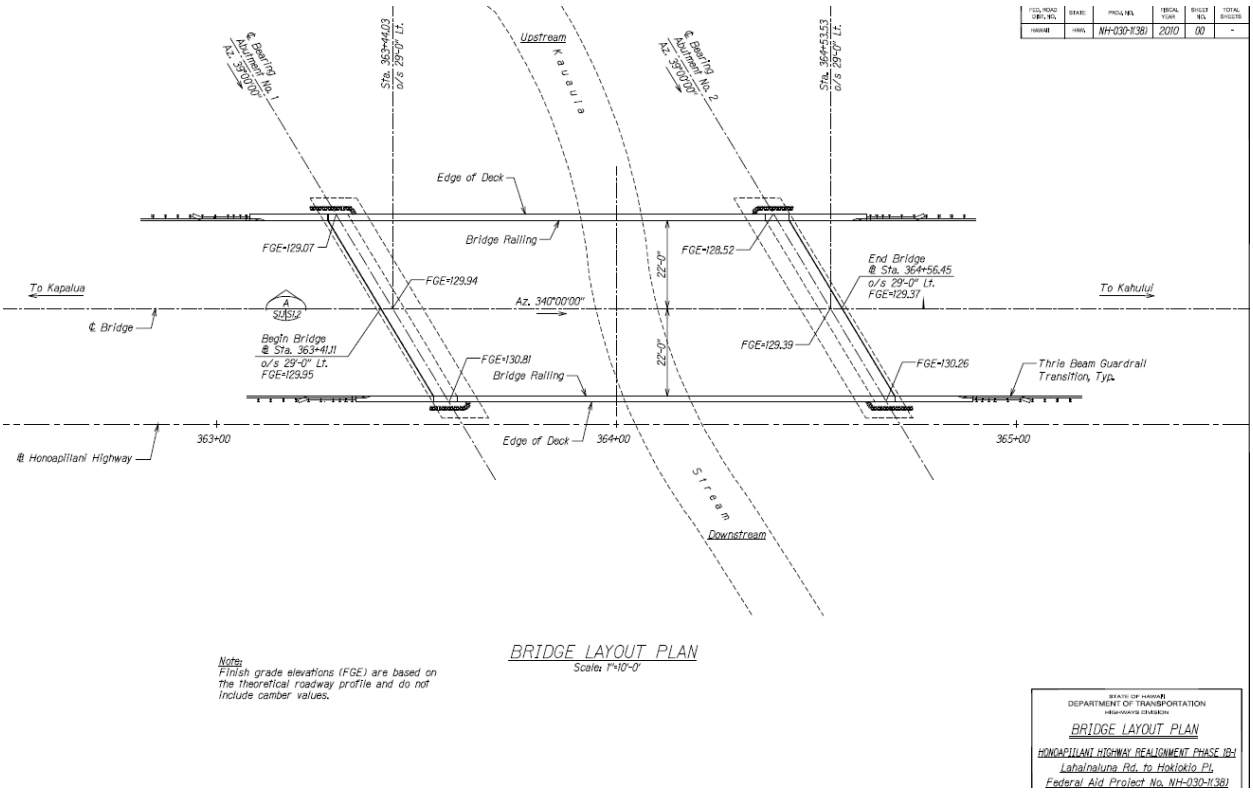

(c)

Figure 16 Kauaula Stream bridge design (KSF Inc., 2011)

3.2 Materials

Subsurface Soil

According to borings B-22 through B-25 drilled by Hirata and Associates, Inc. (2009, Appendix A), the subsurface soils at the abutment locations consisted of clayey silt and silty clay (ML) which extends to a depth of 4.5 feet below the ground surface underlain by an older alluvium (consisting of cobbles and boulders) to a depth of at least 85 feet, corresponding to the maximum drilling depth.

Backfill

A Class B basalt, which met the State of Hawaii Department of Transportation's specifications for 1.5-inch maximum untreated base course, was used as backfill. Figure 17 shows a sample of the material.

Figure 17 Class B basalt sample (Lawrence, 2014)

FHWA's Turner-Fairbank Highway Research Center conducted a grain size distribution test (ASTM D6913), Standard Proctor test (ASTM D698 method C), and large-scale direct shear tests on fully saturated specimens (ASTM D3080) of the backfill.

From the grain size distribution test, it was concluded that the backfill was a GW, based on the Unified Soil Classification System (USCS) and A-1-a based on the AASHTO soil classification system. The grain size distribution curve (Figure 18) yielded the following: D_{60} = 0.37 in., D_{30} = 0.13 in., D_{10} = 0.021 in., C_u = 2.2 and % fines = 3%.

From the standard Proctor test, the optimum water content, w_{opt}, was estimated to be 9% and the maximum dry unit weight, $\gamma_{d\,max}$, was 136 pcf (Figure 19). Since the materials larger than ¾ inch were removed for this test, the onsite optimum water content should be lower, and the maximum dry unit weight should be higher. Subsequently, "HDOT-approved values of maximum dry unit weight and optimum water content were 145 pcf and 7%, respectively" for field compaction control (Lawrence, 2014).

Using the results of the large-scale direct shear test and a linear regression of the Mohr-Coulomb failure envelope, the peak friction angle, ϕ_{peak}, and cohesion intercept, c', of the backfill were estimated to be 53.8° and 1885 psf, respectively (Figure 20). The cohesion is an artifact of the non-linearity of the Mohr-Coulomb failure envelope for granular soils and is neglected in this research because the Mohr-Coulomb model assumes that the failure envelope is linear.

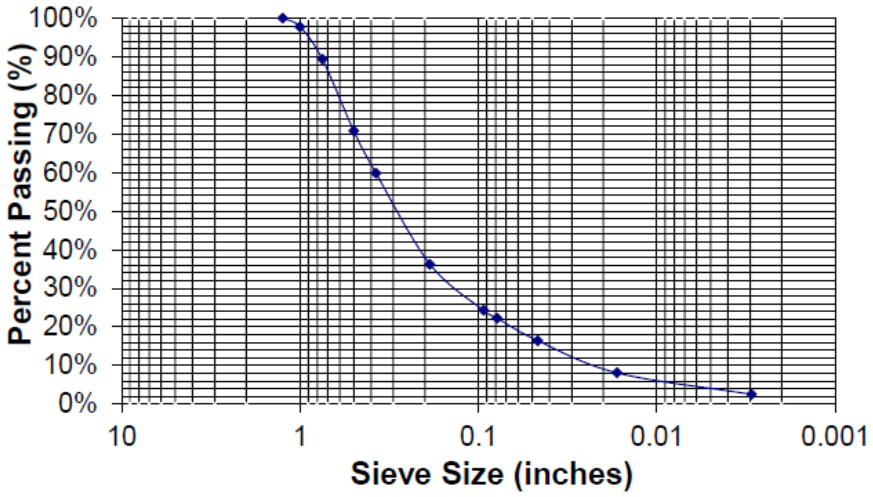

Figure 18 Grain size distribution of the backfill (Lawrence, 2014)

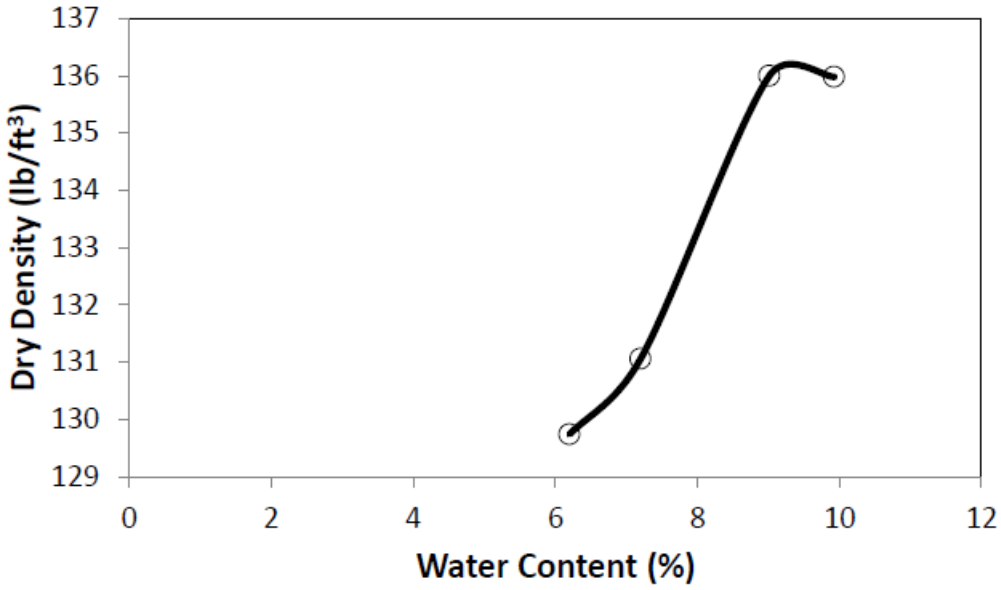

Figure 19 Compaction curve of the backfill with grains finer than ¾ inch (Lawrence, 2014)

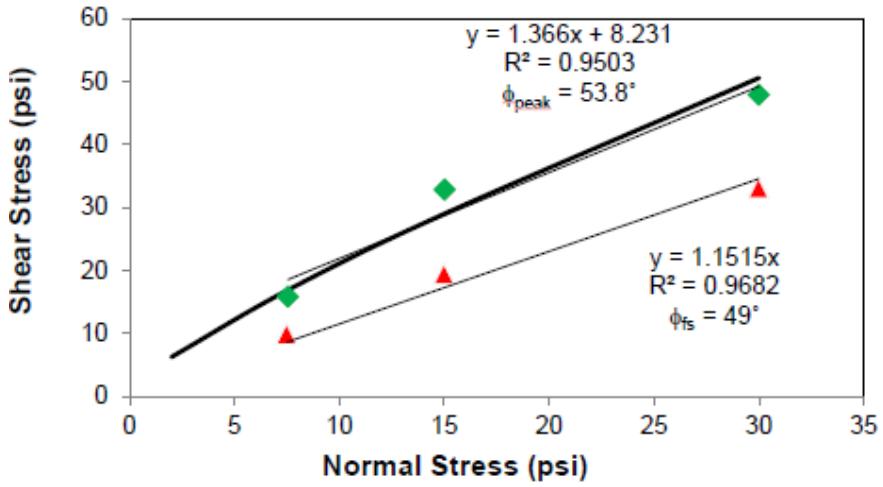

Figure 20 Direct shear test results (Lawrence, 2014)

Geosynthetic Fabric

A woven Mirafi® PET 70/70 was used as the geosynthetic reinforcement. According to the manufacturer's technical datasheet (Appendix B), it is made of high-tenacity polypropylene multifilament yarns with a wide-width tensile strength, T_f, of 4,800 lbs/ft in both the machine and cross-machine directions.

Facing Elements

The facing elements consisted of 12–in.-wide, 16–in.-long and 8–in.-high Maui Concrete Masonry Unit (CMU), each with a weight of approximately 75 lbs (Figure 21).

Figure 21 CMU blocks

3.3 Construction Sequence and Schedule

Construction of Kauaula Stream GRS-IBS began in January 2012 and was completed in May 2013, following the schedule shown in Table 5.

Table 5 Construction sequence and schedule (Lawrence, 2014)

Construction Event	Date
Construction of the reinforced soil foundation	January 2012
Completion of GRS abutments	March 2012
Rip rap placed in front of GRS abutments	April 2012
Footings Poured	July 2012
First tub girder completed	July 30, 2012
Second tub girder completed	September 15, 2012
Precast planks poured	October 2012
First tub girder launched	December 12, 2012
Second tub girder launched	December 27, 2012
Third tub girder launched	January 3, 2013
Precast planks placed on girders	January 2013
End walls, wing walls, and top deck completed	February 2013
Integral approach completed	March 2013
Bridge Completed	May 2013

The two GRS abutments were constructed using the CMU blocks as a form. Each lift was first backfilled to the top of the CMU blocks (Figure 22), then compacted to at least 95% relative compaction (Figure 23), and lastly geosynthetic fabric was placed on top. These steps were repeated for the first 5 layers. For the top 5 layers of the abutments, "the height of each lift was halved with a fabric placed over each lift; i.e.; the geosynthetic frequency was doubled" (Lawrence, 2014). As Figure 24 shows, the geosynthetic between the CMUs was burnt off to allow for the top 4 blocks to be grouted and pinned.

After placing the riprap in front of the GRS abutment, a 54-ft-long by 5-ft-wide concrete footing, with an average thickness of 2.25 ft, was poured on each abutment (Figure 25). The three tub girders were then launched across the stream. Construction of the end wall, top deck, and wing walls occurred after placement of the precast planks on the three tub girders (Figure 26).

Using the same backfill material as the GRS abutments, an integrated approach was placed and compacted to 95% relative compaction, with a 12–in. spacing between the geotextiles. Figure 27 shows the completed Kauaula Stream bridge.

Figure 22 Placement of backfill behind a row of CMU blocks (Lawrence, 2014)

Figure 23 Compaction of backfill (Lawrence, 2014)

Figure 24 Burning geosynthetic between top 4 CMU blocks (Lawrence, 2014)

Figure 25 Concrete footing on GRS abutment (Lawrence, 2014)

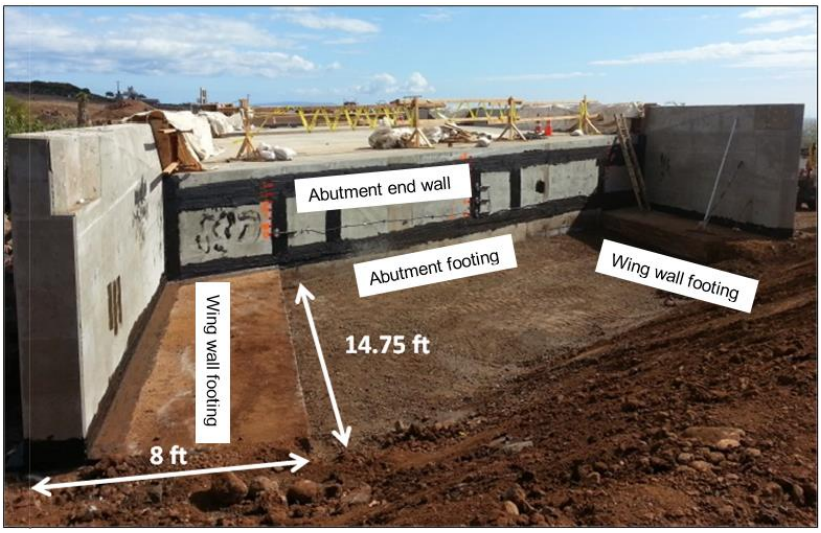

Figure 26 Completed end wall and wing walls (Lawrence, 2014)

Figure 27 Completed GRS-IBS over Kauaula Stream (Lawrence, 2014)

3.4 Instrumentation

As indicated in Section 3.1, the superstructure and substructure of the GRS-IBS were instrumented to monitor the behavior during and after construction. Strain gauges (SG) were installed at the third point of each tub girder to measure the concrete strains in the superstructure (Figure 28).

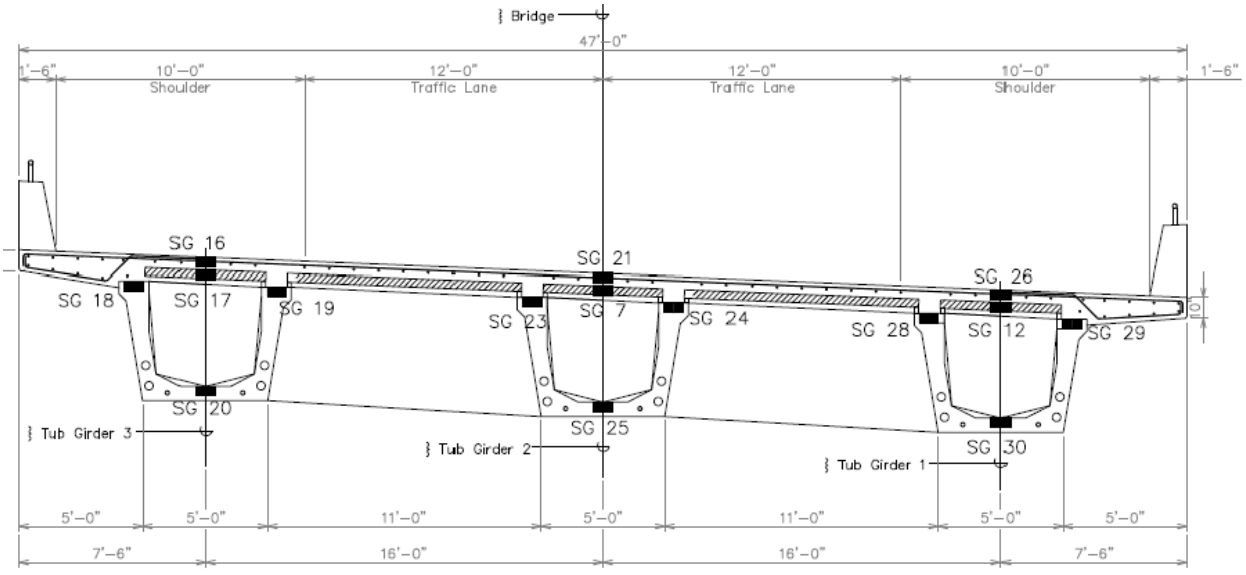

Figure 28 Strain Gage (SG) layout at the third point closest to Abutment 2 (KSF, Inc. 2011)

To measure the vertical pressure on the abutment, three earth pressure (EP) cells were installed along the centerline of the middle tub girder on Abutment 2, below the toe, middle and heel of the concrete footing.

Three lateral earth pressure or fatback (FB) cells were installed behind the end wall at the middle tub girder at each abutment, and three FBs were installed behind the first, fifth and ninth CMU blocks below the middle tub girder.

To monitor the movement of the CMU facing, inclinometers (I) were installed through the CMUs in the middle of the abutments. The inclinometers were spaced 2 ft apart in the upper 10 ft of the GRS (zone of interest) and every 4 feet below that. Figure 29 shows the layout of the monitoring instruments at Abutment 2.

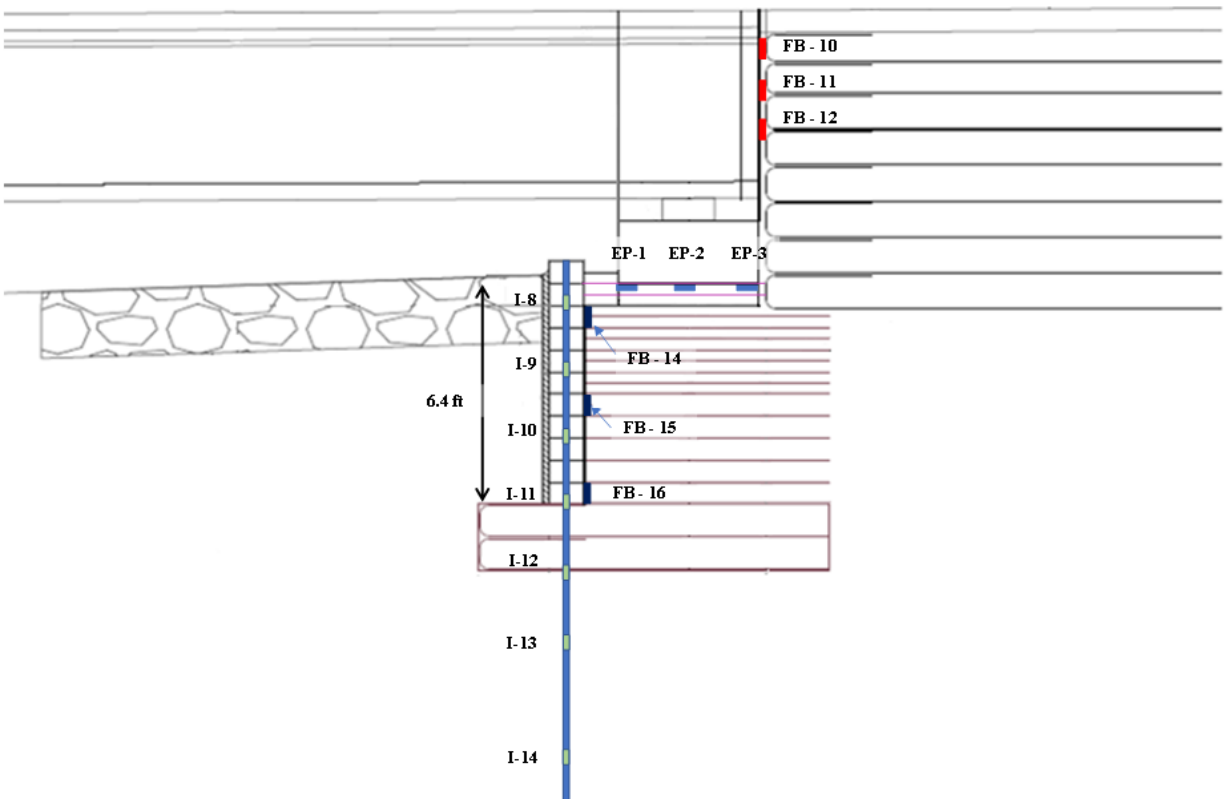

Figure 29 Instrumentation layout at Abutment 2

3.5 Instrumentation results

The results of the instrumentation, described in the previous section, are shown in Figure 30 (a through f) and the following conclusions can be surmised.

1. Based on strain gage readings, the temperature in the bridge deck surface fluctuated the most due to direct sun exposure while that at the base of the tub girder, being in the shade, fluctuated the least (Figure 30a). As the temperature increases, the concrete superstructure expands decreasing the compressive strain and vice versa when the temperature decreases.

2. Strain fluctuations in the bridge deck surface were greatest while those in the base of the tub girder were least (Figure 30b). Uneven strain fluctuations at the top and bottom suggests that the superstructure may be experiencing bending (cycles of hogging and sagging) during thermal expansion and contraction. Furthermore, the bridge ends are significantly restrained from rotation by the pair of wing-walls that run longitudinally at the ends of the bridge abutments. In terms of magnitude, the largest compressive strains (negative values) were observed in the tub girder floor. The compressive strains decreased upward to a minimum in the wearing surface. This is counterintuitive because normally, a beam sags under its own weight causing the top and bottom to be in

compression and tension, respectively. This strain distribution is attributable to the effects of post-tensioning that resulted in a reversal in curvature of the superstructure.

3. The measured vertical pressures cycled daily (Figure 30c). As the temperature increased, the bridge superstructure expands and hogs causing the footing to rotate about a transverse axis whereby the stream-side portion of the footing "lifts off". The EP cell closest to the facing experienced the largest daily pressure fluctuation (from 2,500 to 3,000 psf) while the one farthest from the facing saw the smallest. Also, the average of the 3 measured vertical pressures fluctuates during each thermal cycle and does not remain constant at the stress corresponding to the bridge dead load (4,030 psf). This stress signature implies that the point of rotation lies within the wing-wall footings rather than within the abutment footing.

4. The lateral pressures on the CMU facing peaked when cold and troughed when hot daily (Figure 30d). It follows the same trend as the vertical footing pressure and is consistent with the lateral facing displacement (see 6 below).

5. The end-wall lateral pressures peak when hot as a result of the end wall moving towards the approach fill during superstructure expansion and vice-versa when cold (Figure 30e).

6. The abutment face moves outward and inward in response to increased and decreased vertical footing pressures, respectively (Figure 30f).

In summary, trends in field observations all corroborate each other. Ooi et al. (2019b) showed that bridge settlement continued to occur even after the bridge is completed. They postulated that the bridge footing settlement is a result of daily bearing pressure fluctuations. Large fluctuations in vertical footing pressures can cause significant cyclic-induced deformation. Therefore, the main question is whether the observed magnitudes of daily bearing pressure fluctuation are reasonable and correct. The following sections will attempt to shed light on this question.

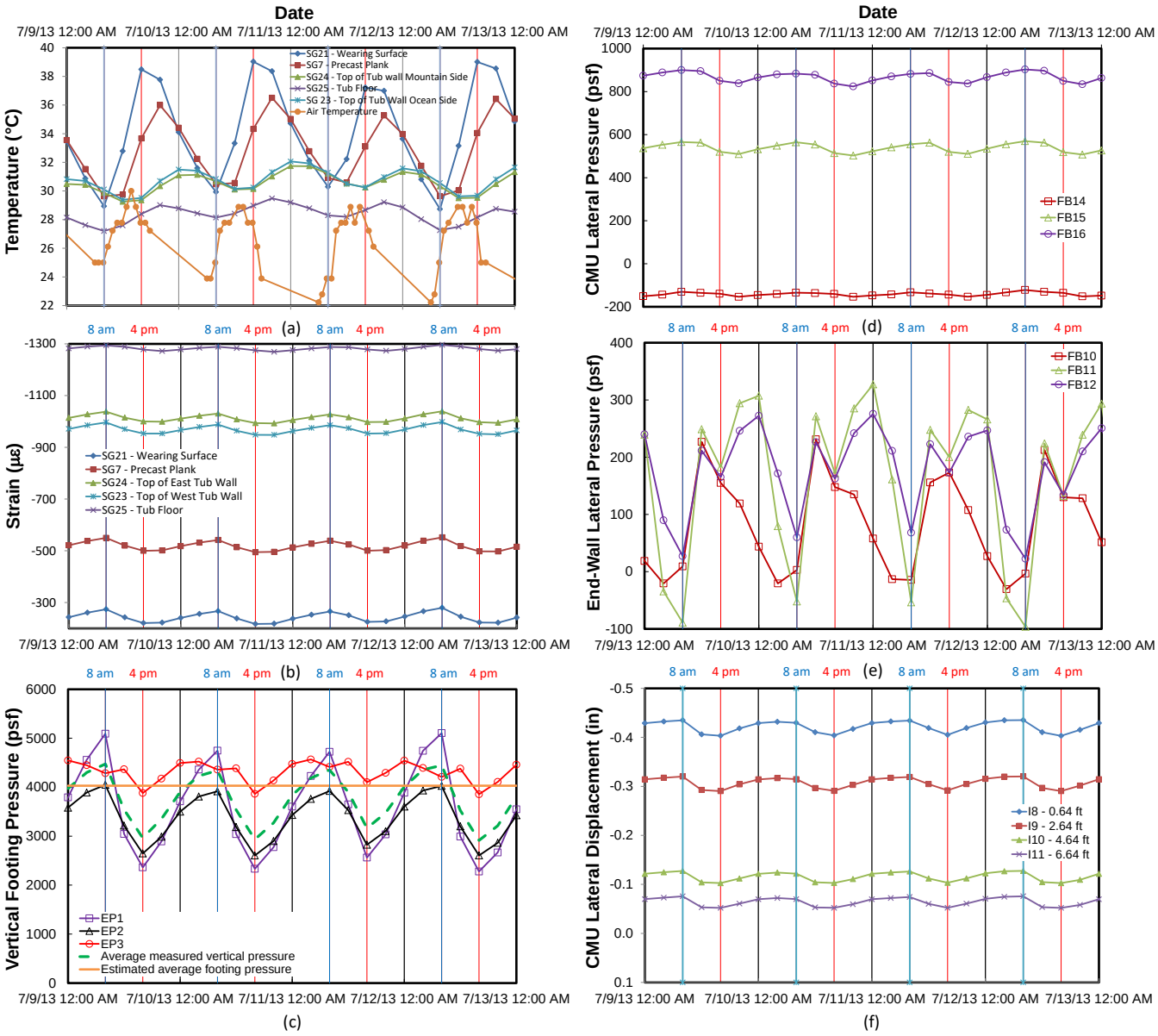

Figure 30 (a) Temperature; (b) strain; (c) footing vertical pressure; (d) CMU lateral pressure; (e) end-wall lateral pressure; and (f) CMU lateral displacement vs time

4 FINITE ELEMENT ANALYSIS

4.1 LUSAS Overview

Finite Element (FE) analysis of the Kauaula Stream GRS-IBS was conducted using the London University Structural Analysis System (LUSAS) software. Although LUSAS is primarily a structural analysis software, the addition of soil constitutive models allows users to analyze and design soil and structure interactions projects such as bridge abutments, retaining walls, tunnels and dams (LUSAS, 2016).

This section describes the FE model, boundary conditions and assumptions made, the properties of each different material component in the model and the way loads are input in LUSAS.

4.2 2D Plane Strain vs. 3D Modeling

As mentioned in Section 3.1, the Kauaula Stream bridge is skewed (31°), super-elevated (4%) and has a 0.5% downward slope from Abutment 1 to Abutment 2. To truly model the bridge and wing walls requires a 3D analysis, which is complex and time consuming. For the sake of simplicity, the skew, super-elevation and slope are ignored allowing only half the bridge to be modeled using a 2D plane strain analysis. Figure 31 depicts all the components in the 2D plane strain model.

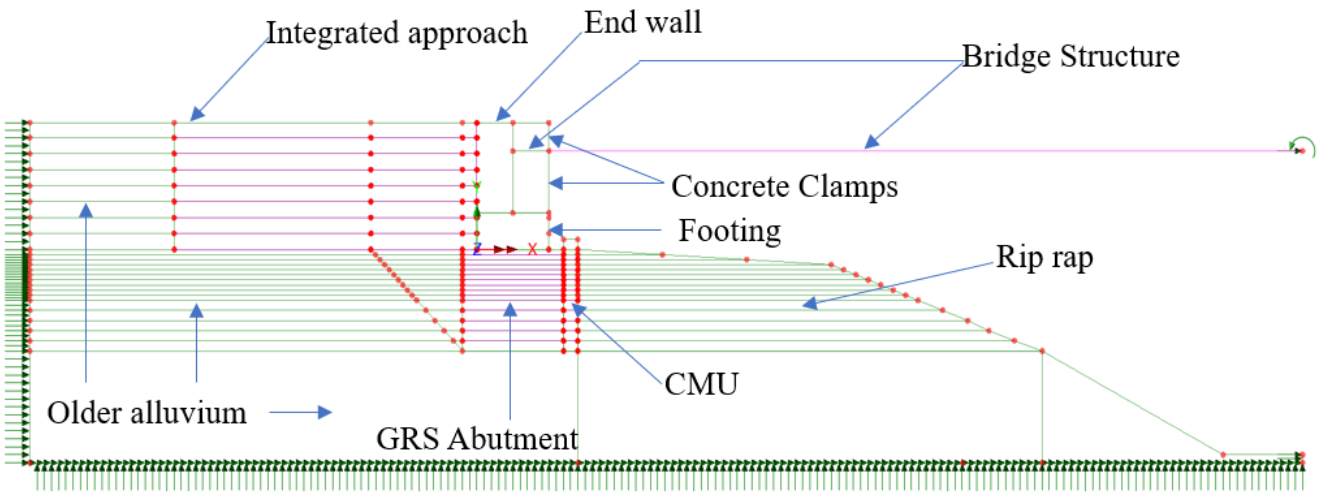

(a)

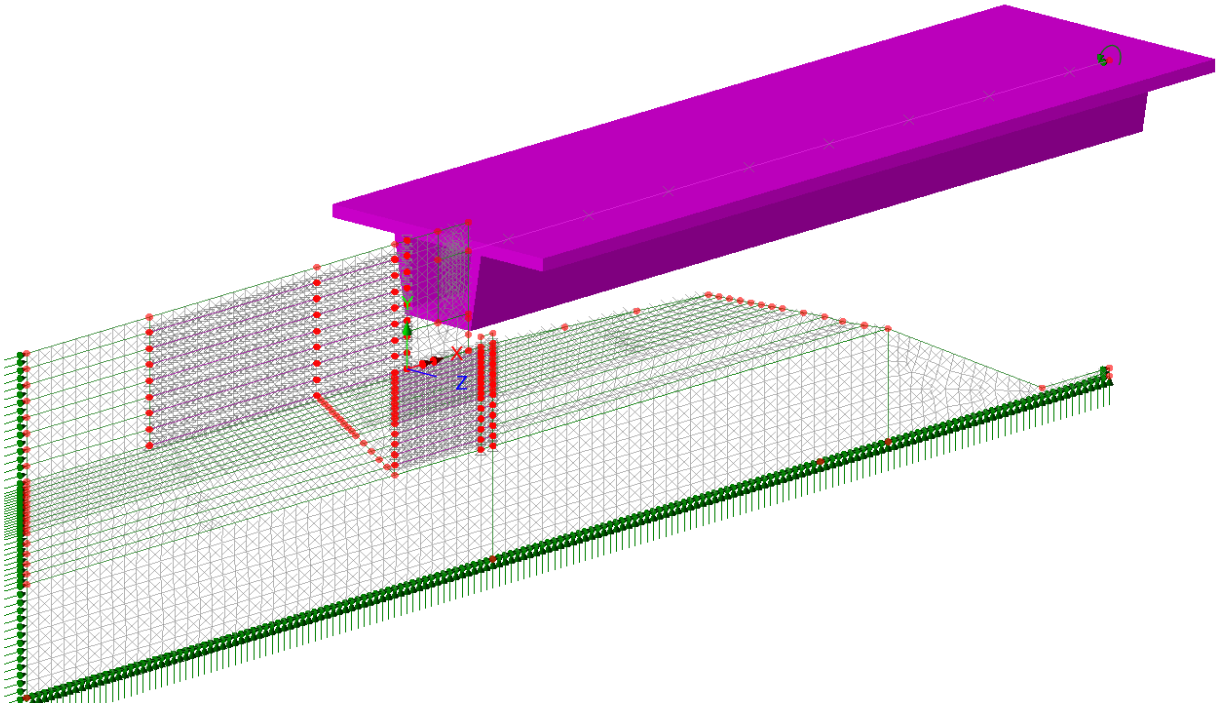

(b)

Figure 31 LUSAS 2D plain strain model (a) elevation view, (b) isometric view

4.3 Modeling of Non-Concrete Materials

Non-concrete materials include soils and geotextile. Their properties are described in this section.

4.3.1 Soil

All soils are modeled as a bi-linear elasto-plastic Mohr-Coulomb material with properties shown in Table 5. The geomaterial that influences the GRS-IBS behavior the most is the GRS abutment backfill that is directly below the footing. Properties of the older alluvium and riprap have less of an influence since they are located farther way. Friction angle, ϕ_{peak}, of the fill soil was measured based on large scale direct shear tests on specimens that are 12 in. x 12 in. x 8 in. (Figure 20). The dilation angle (ψ) of the GRS backfill was derived based on Bolton's (1986) expression $\phi_{peak} = \phi_{crit} + 0.8\psi$ and the measured ϕ_{crit} = 49° and ϕ_{peak} = 53.8°. For the older alluvium and riprap, ψ was calculated assuming $\psi = \phi_{peak}$ - 30°. A small cohesion is specified to aid in numerical stability.

LUSAS allows for the Young's modulus of the GRS backfill to increase linearly with depth. Using Duncan and Chang's (1970) hyperbolic model, the initial tangent modulus, E_i, can be estimated as follows:

$$E_i = k\left(\frac{\sigma_3}{p_a}\right)^n \quad (10)$$

where k = modulus number, p_a = atmospheric pressure and n = modulus exponent. It is not uncommon to assume that a soil's secant Young's modulus at 50% strength (E_{50}) is half the initial tangent modulus (PLAXIS, 2014). Therefore, the Young's moduli, E_{50}, above and below the footing can be approximated by plotting E_{50} with depth with the aid of Equation 11 and by performing a linear regression of the calculated data points as shown in Figure 32.

$$E_{50} = \tfrac{1}{2}E_i = \tfrac{1}{2}k\left(\frac{\sigma_3}{p_a}\right)^n = \tfrac{1}{2} * 600\left(\frac{\sigma_3}{p_a}\right)^{0.4} = 300\left(\frac{\sigma_3}{p_a}\right)^{0.4} \quad (11)$$

where σ_3 = minor principal stress = horizontal stress, k = 600 for a GW backfill with a unit weight of 150 pcf and n = 0.4 (Duncan et al., 1980 – see Table 4).

.

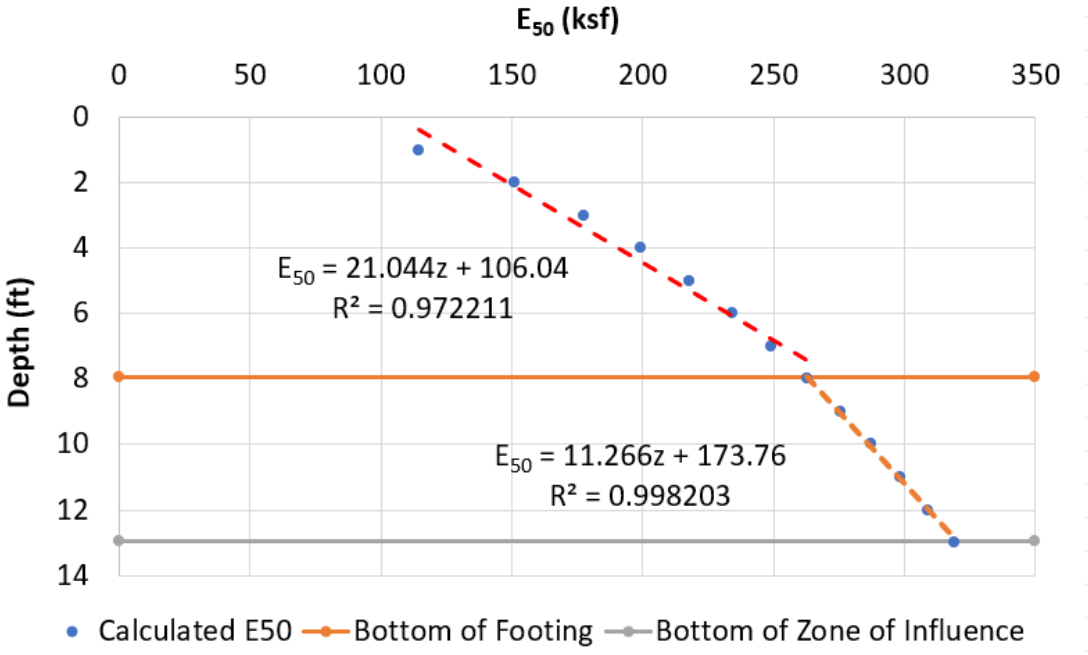

Figure 32 Linear regression of E_{50} vs. depth z

4.3.2 Geotextile

It is sufficient to model the geotextile as linear elastic since it is nowhere near being torn under working stresses. In this case, an axial stiffness, *EA*, for the geotextile is needed where *E* = Young's modulus and *A* = cross-sectional area. *EA* can be derived as follows. The load-deformation relationship of a geotextile in a uniaxial tension test is commonly expressed as load/width vs. strain. Since *E* is the slope of the load/area vs. strain curve, the slope of load/width vs. strain curve is *E**thickness. In plane strain, the width is taken as 1 unit of length, hence *E***A* = *E**thickness*1 = slope of load/width vs. strain curve. The tensile strength at 5% strain of the geotextile in the cross-machine direction is 2400 lb/ft (Tencate, 2014). Hence, *EA* = 2400/0.05 = 48,000 lbs/unit length of abutment wall. This value is derived from in-air wide width tensile tests. As shown in sections 2.1.1 through 2.1.4, there is a proliferation of papers

showing that the in-air stiffness can be less than the in-soil stiffness due to the effects of confining stress in non-woven geotextiles. However, due to a lack of woven geotextile test data and since it is not known how much of the increase in stiffness is due to friction between the geotextile and the confining medium, the effects of confining pressure on geotextile stiffness is not considered herein.

4.3.3 Joint Elements

Joint elements are utilized at the CMU-soil, footing-soil, geotextile-soil and CMU-geotextile interfaces with interface friction angles, $\delta = \frac{2}{3}\phi$ (= 35.9^0 for concrete cast with formwork) (Potyondy, 1961), ϕ (= 53.8^0 for concrete cast directly against soil) (Potyondy, 1961), $4/5\phi$ (= 43^0) (Martin et al., 1984) and 33^0 (slightly less than $\frac{2}{3}\phi$ since the geotextile is smoother than soil), respectively. Joint elements are bi-linear elasto-plastic. The linear elastic shear stiffness, k_s, was estimated assuming fully plastic behavior at a displacement $\Delta = 0.1$ inch as follows:

$$k_s = \sigma \tan \delta / \Delta \quad (12)$$

where σ = normal stress. For the geotextile-soil, footing-soil and CMU-geotextile interfaces, σ = vertical stress while for the CMU-soil interface, σ = horizontal stress at the respective elevations.

LUSAS also requires specification of a normal stiffness for joint elements. Theoretically, the normal stiffness should approach infinity. Therefore, a large normal stiffness (6×10^7 lb/ft^3) was assigned based on the work by Nakai (*2013*).

4.4 Concrete Components

Concrete components include bridge superstructure, clamps for the bridge "stick" model, end wall, footing, and CMU facing. The bridge "stick" is embedded in the upper and lower clamps sitting on top of the abutment footing. The clamps merely serve to receive the "stick" model. These components are all modeled as linear elastic materials. Apart from CMU blocks, all concrete components were assigned a coefficient of thermal expansion equal to $6 \times 10^{-6}/^0$C (Table 6).

4.4.1 Bridge Superstructure

Half of the 110-ft bridge span (divided through the centerline) is modeled in the 2D plane strain analysis. The bridge span is defined as the distance between the front faces of the end walls of each abutment. Since the end wall is 2.5 ft thick and the footing is 5 ft wide, the bridge span is defined as the distance between the middle of the abutment footings. The "stick" model of the bridge superstructure consists of a 2.5-ft clamped section and a 52.5-ft un-clamped section.

4.4.2 Clamps for Bridge "Stick" Model

The two blocks serving as "clamps" have 0 unit weight because the bridge weight is accurately provided by the "stick" model. The clamps are assigned a modified Young's modulus such that

the sum of the flexural stiffness of the two clamps and the bridge stick equals that of the unclamped bridge stick (to the right) as follows:

$$E_1I_1 = E_2I_2 + E_3(I_3 + A_3 y_3^2) + E_4(I_4 + A_4 y_4^2) \quad (13)$$

where *E*, *I*, *A* and *y* are the Young's modulus, centroidal moment of inertia, area and distance from the centroid of that element to the centroidal axis of the superstructure, respectively, and the subscripts *1*, *2*, *3* and *4* refer to the unclamped bridge stick, clamped bridge stick, and top and bottom clamp blocks, respectively. The parallel axis theorem requires inclusion of the Ay^2 terms.

4.4.3 Footing

A 5-ft-wide and 2.25-ft-high concrete footing with a unit weight of 150 pcf (Table 6) is placed on the GRS abutment. The footing has a full moment connection with the end wall and concrete clamps.

4.4.4 End Wall

The same material properties as the footing are used for the 2.5-ft-wide end wall located between the integrated approach and the superstructure (Table 6).

4.4.5 CMU

Unit weight of CMU is weight/gross volume and gross volume includes the void volume in the hollow tile concrete blocks (Table 6).

Table 6 Model parameters

Material	Young's Modulus (psf)	Poisson's Ratio	Unit Weight (pcf)	Cohesion (psf)	Friction Angle (°)	Dilation Angle (°)	Coefficient of Thermal Expansion ($°C^{-1}$)
Mohr-Coulomb							
Fill above footing	$21.044 \times 10^3 z + 106.04 \times 10^3$	0.2	151	0.01	53.8	6	NA
Fill below footing	$11.26 \times 10^3 z + 173.76 \times 10^3$						
Alluvium	1.04×10^6	0.3	160	0.01	55	25	NA
Riprap	1.04×10^6	0.3	160	0.01	55	25	NA
Linear Elastic							
CMU	5.80×10^8	0	93.5	NA	NA	NA	NA
Concrete footing	5.80×10^8	0.21	150	NA	NA	NA	6×10^{-6}
Endwall	5.80×10^8	0.21	150	NA	NA	NA	6×10^{-6}
Bridge (un-clamped portion)	734×10^6	0.21	160	NA	NA	NA	6×10^{-6}
Bridge (clamped portion)	1.41×10^8						
Concrete clamps	1.41×10^8	0.21	0	NA	NA	NA	6×10^{-6}

4.5 Boundary Conditions

The bottom horizontal of the model is fixed, the soil on the left-hand vertical side is on rollers, and the top right corner of the superstructure is fixed in the x-direction, free in the y-direction from translating and fixed in the z-direction from rotating.

4.6 Modeling Construction Sequence

The finite element model was built using the following steps and then thermally loaded at the last step:

1. Turn on gravity for the sloping ground leading into the stream.
2. Build the GRS abutment by placing the CMU, backfilling behind the CMU and laying the geotextile on top.
3. Repeat Step 2 for the bottom 5 courses.
4. For the next 5 courses, repeat Step 2 but add a geotextile at the mid-depth of each course.
5. Repeat Step 4 for the top 5 courses.
6. Place riprap in front of the CMU.
7. Place footing on top of the GRS.
8. Place clamps, bridge stick model and end wall on footing.
9. Place integrated approach behind end wall layer by layer.
10. Apply thermal loading to the superstructure (see Section 4.7).

4.7 Modeling Temperature Effects

Figure 33 shows a cross-section of the bridge superstructure where the measured temperatures vary over the depth of the bridge superstructure. The temperatures also vary with time. Such a measured temperature variation can be applied to the superstructure in LUSAS by considering that the strain caused by a change in temperature, T, can be estimated as follows:

$$\varepsilon = \alpha T \tag{14}$$

where ε = strain and α = coefficient of thermal expansion of the superstructure. Assuming that plane cross-sections remain plane after bending, the corresponding stress in the superstructure, σ, is related to the strain as follows:

$$\sigma = \varepsilon E = \alpha T E \tag{15}$$

where E is the Young's modulus of the superstructure concrete. The superstructure can be divided into a number of tributary areas depending on the shape of the temperature profile and depending on the change in shape of the cross-section. The force at each tributary area, i, can be calculated as follows:

$$F_i = \sigma_i A_i = \alpha T_i E A_i \tag{16}$$

where A_i is the tributary area for that force. All the forces can be integrated over the entire superstructure depth to obtain an equivalent temperature, T_{eq}, which imposes an equivalent axial force of magnitude ΣF_i on the superstructure as follows:

$$T_{eq} = \Sigma F_i/(\alpha E \Sigma A_i) \quad (17)$$

The superstructure will experience the effects of both axial load and bending due to the nature of the measured temperature distribution. To estimate the effects of bending, the moment of each tributary force about the neutral axis must be estimated.

$$M_i = F_i y_i \quad (18)$$

where y_i = moment arm of tributary force, F_i, about the neutral axis. The equivalent temperature gradient, G_{eq}, which produces the effects of the required equivalent moment (ΣM_i) can be estimated as follows:

$$G_{eq} = \Sigma M_i/(\alpha E \Sigma I_i) \quad (19)$$

where I_i = moment of inertia of tributary area i. The calculated equivalent temperatures and gradients based on the July 9-13, 2013 measured temperatures are presented in Figures 34a and 34b, respectively. It can be seen that they both have a near-sinusoidal form.

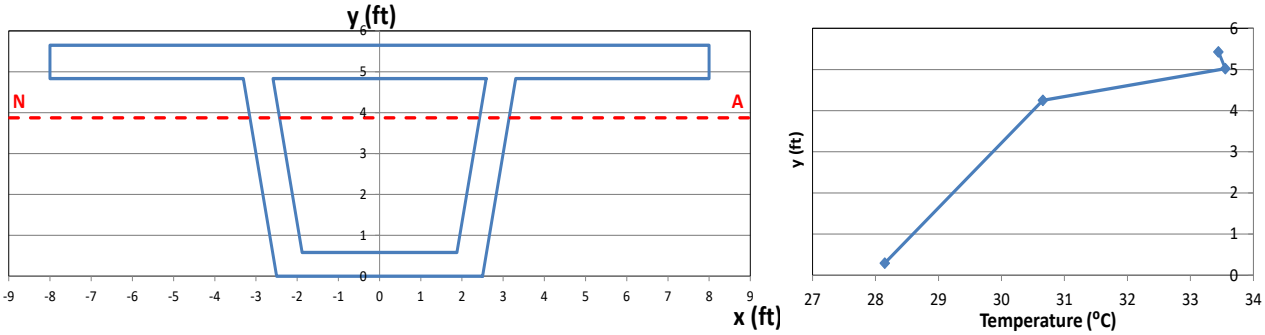

Figure 33 Superstructure cross-section and measured temperature distribution at midnight on 7/9/2013

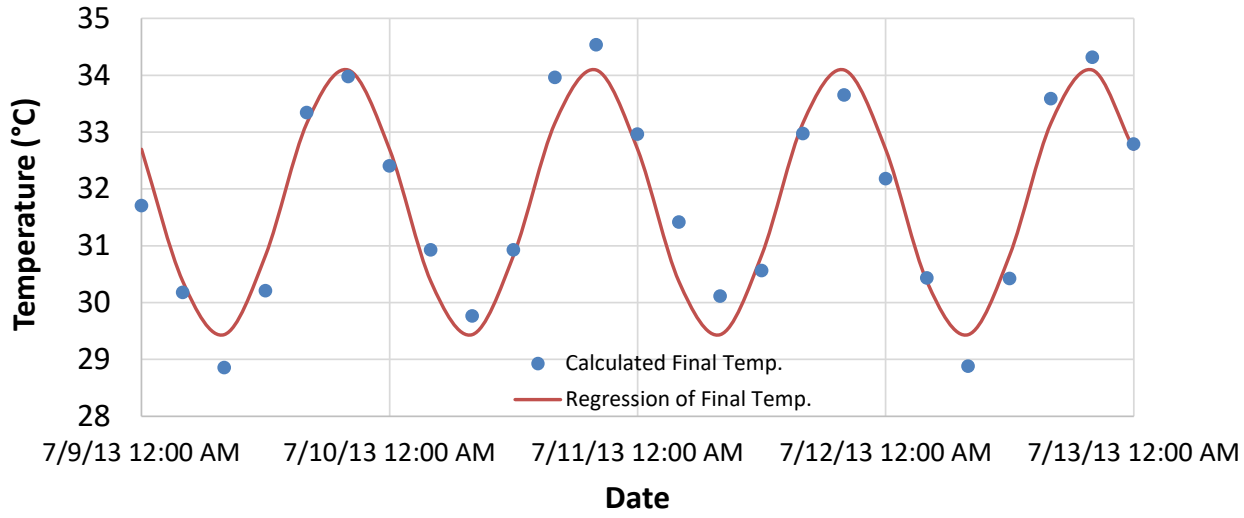

(a)

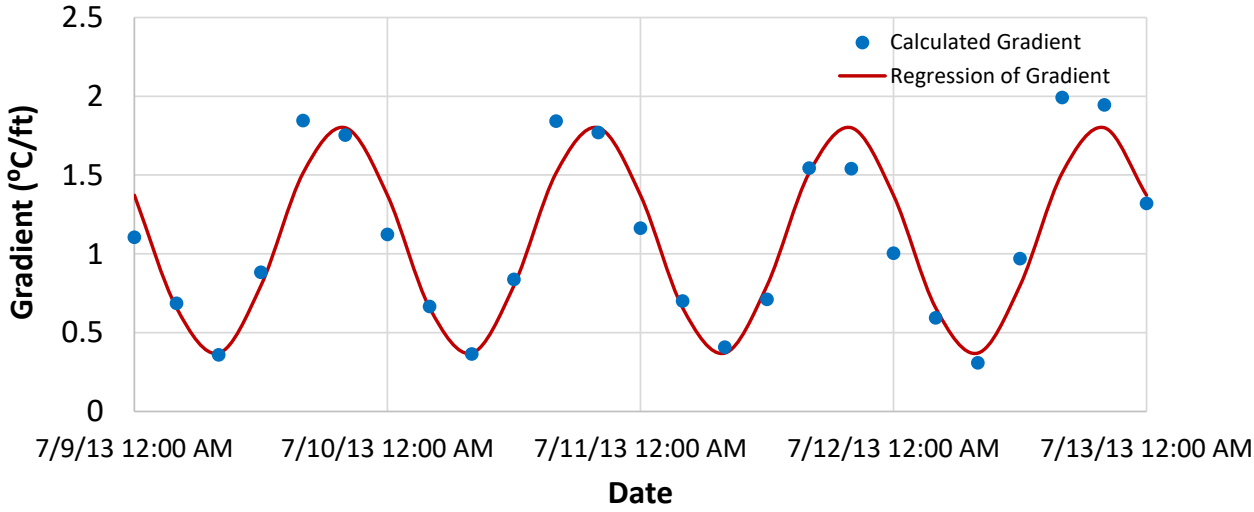

(b)

Figure 34 (a) Calculated equivalent temperature based on measured temperatures and a best-fit sine curve to fit the calculated points, (b) calculated equivalent gradient based on measured temperatures and a best-fit sine curve to fit the calculated points

Sinusoidal variation of both the equivalent temperatures and gradients can be easily applied using the load factor option in LUSAS. Assuming a load factor of -1 represents the trough while a load factor of +1 corresponds to the peak of the sine curve, the initial and final values of temperature (T_I and T_F) and gradient (G_I and G_F) which are needed as input parameters in LUSAS can be solved as follows:

$$-1*T_F - T_I = T_{min} \quad (20)$$

$$+1*T_F - T_I = T_{max} \quad (21)$$

where T_{min} and T_{max} are the trough and peak temperatures, respectively. From equations 22 and 23, T_F and T_I can be obtained.

$$T_I = -(T_{max} + T_{min})/2 = -31.76^{o}C \quad (22)$$

$$T_F = (T_{max} - T_{min})/2 = 2.34^{o}C \quad (23)$$

Similarly,

$$G_I = -(G_{max} + G_{min})/2 = -1.08^{o}C/ft \quad (24)$$

$$G_F = (G_{max} - G_{min})/2 = 0.72^{o}C/ft \quad (25)$$

Rather than applying these calculated equivalent temperatures and gradients based on measured temperatures, it is more correct to calculate a set of equivalent temperatures and gradients based on measured strains (Figure 35). This is due to the fact that:

1. Thermal effects in a post-tensioned superstructure are complicated affecting not only volume changes in the concrete but also forces in the post-tensioned tendons;
2. The initial strains are not zero when the strain gages are first zeroed. They evolve from initial pour due to concrete creep and shrinkage, post-tensioning and thermal loading; and
3. Thermal effects are time-dependent and non-instantaneous.

Therefore, the measured strain, ε_{mi}, can be used in place of αT_i in Equation 16 as shown in Equation 26 below.

$$F_i = \varepsilon_{mi} E A_i \quad (26)$$

Equations 17 through 21 still apply. The resulting equivalent temperatures and gradients for July 9-13, 2013 are shown in Figures 36a and 36b, respectively. Similarly, using equations 22 through 25, T_I, T_F, G_I, and G_F were calculated to be 164°C, 3.79°C, -22.2 °C/ft and 0.968°C/ft, respectively. It can be seen that the equivalent temperatures and gradients based on measured strains are markedly different than those based on measured temperatures.

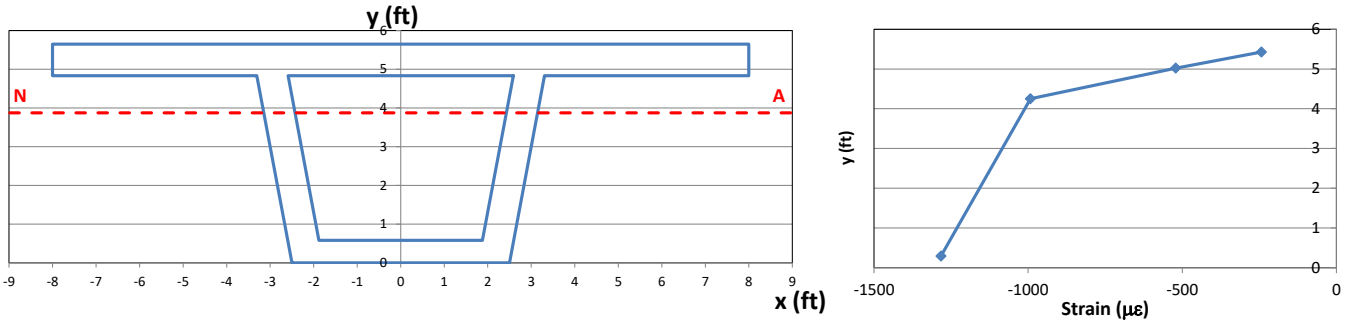

Figure 35 Superstructure cross-section and measured strain distribution at midnight on 7/9/2013

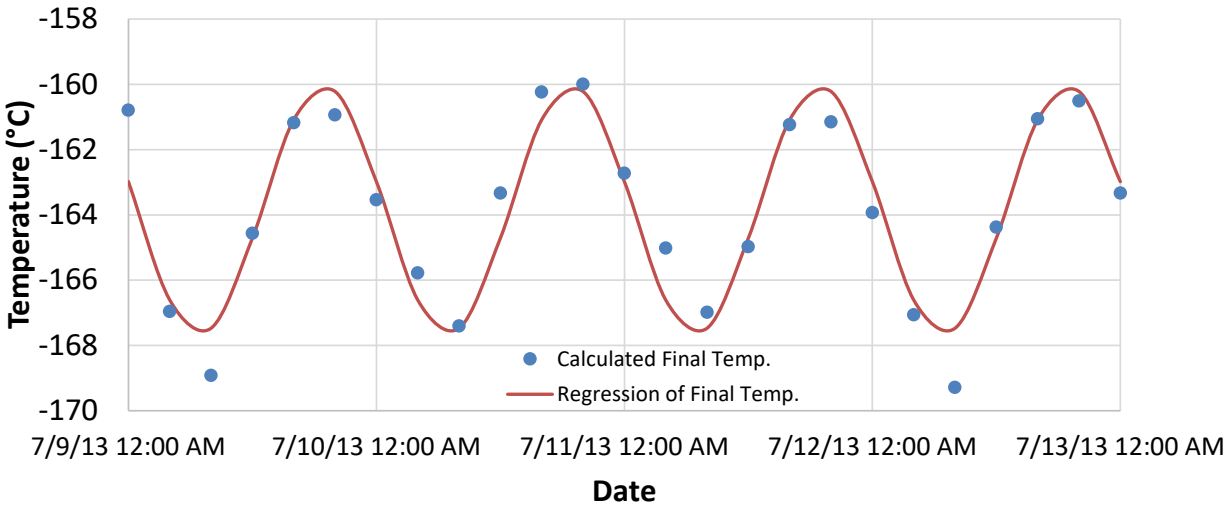

(a)

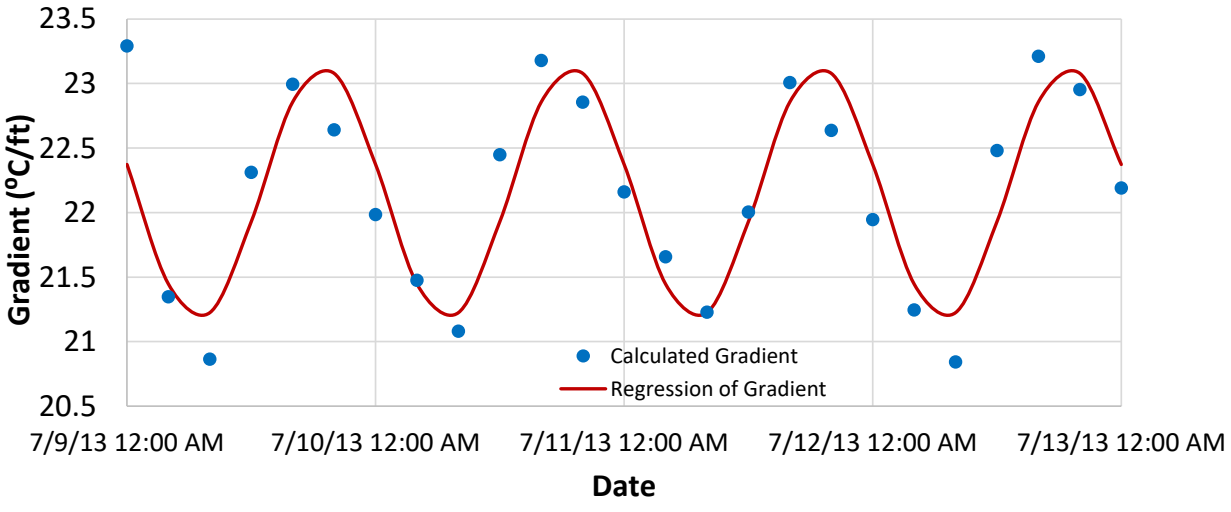

(b)

Figure 36 (a) Calculated equivalent temperature based on measured strains and a best-fit sine curve to fit the calculated points, (b) calculated equivalent gradient based on measured strains and a best-fit sine curve to fit the calculated points

5 RESULTS

A numerical analysis of the GRS-IBS was first performed by applying the measured temperatures in the strain gages to the respective locations in the superstructure along with utilizing an appropriate coefficient of thermal expansion for the superstructure concrete. These results are presented in Section 5.1. These results reveal that the approach of applying measured temperatures to the superstructure is not adequate in that temperature changes do not affect only volume change, but they also affect the forces in the post-tensioning cables. Also, thermal effects are complicated by the fact that temperature change in the superstructure is time-dependent and not instantaneous. A more novel way of modeling the bridge behavior is presented in Section 5.2.

5.1 Application of Measured Superstructure Temperature

As discussed in Section 4.7, the measured superstructure temperatures were applied to the finite element model as initial and final temperatures and gradients, the values of which are shown in equations 22 through 25. Figure 37 shows the calculated vertical pressures below the 5-ft-wide abutment footing for load factors -1, 0 and +1, which correspond to hours of 8 a.m., 2 p.m. (also 2 a.m.) and 8 p.m., respectively. Figure 38 presents a comparison of the calculated and measured vertical pressures at the toe (EP1), middle (EP2) and heel of the footing (EP3), during a 24-hour period. The calculated pressure fluctuation at the toe of the footing between 8 a.m. and 8 p.m. is 240 psf (Figure 38a), which is less than 1% of the monitored field fluctuation of 2,500 -3,000 psf (Figure 30c). Figure 37 also illustrates that the point of rotation of the footing is approximately in the middle of the 5-ft-wide footing, which is contradictory to the monitored field data.

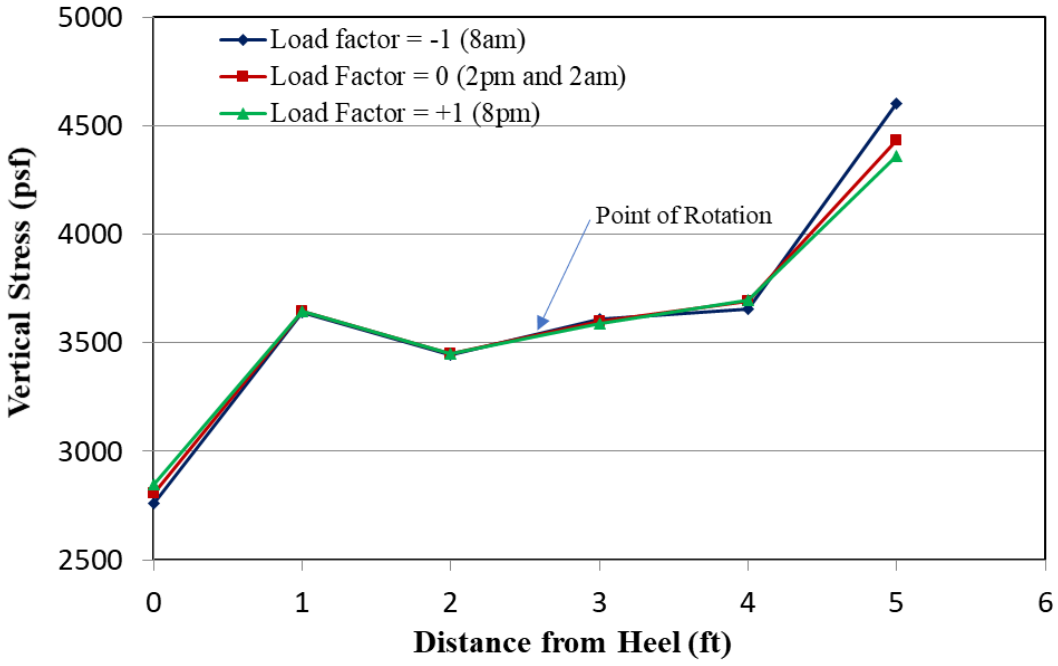

Figure 37 Calculated vertical stresses along the 5-ft footing width at load factors -1, 0 and +1

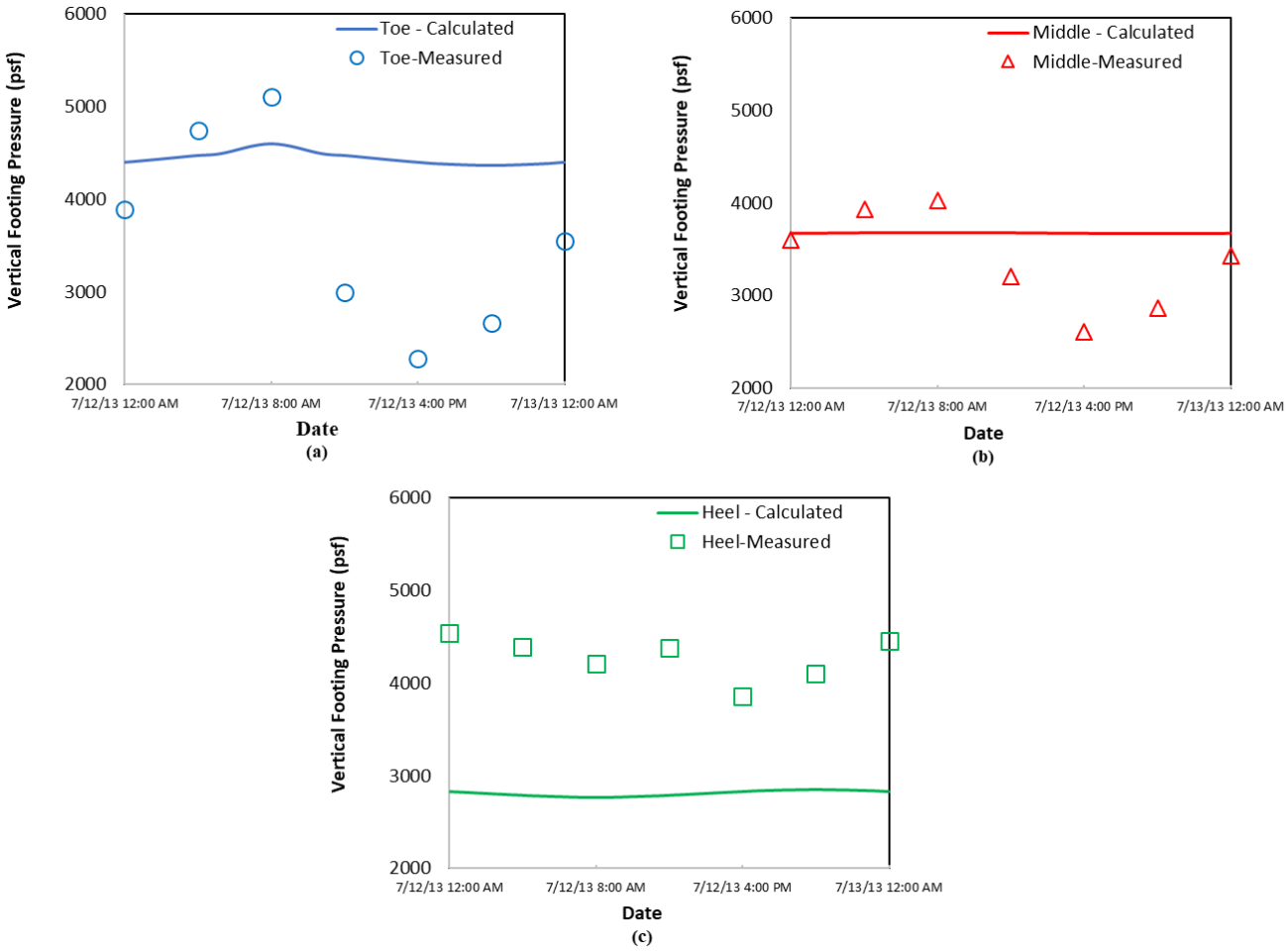

Figure 38 Calculated and measured vertical pressures at (a) toe, (b) middle (c) heel

5.1.1 Modification of Model to Incorporate the Effects of the Wing Walls Footings

From the instrumentation results, it can be inferred that the footing rotates about a point outside the abutment footing footprint; i.e.; within the wing walls. The wing walls cannot be physically represented in a 2D plane strain model. However, the stiffness of the wing wall footings can be idealized by replacing the wing wall and bridge footings with an equivalent rectangular footing of the same length but with a modified width B (Figure 39). B can be estimated by setting the moment of inertia of the equivalent rectangular footing ($I_{rect\ XX}$) equal to the sum of the moments of inertia of the bridge and wing wall footings with the aid of the parallel axis theorem as follows:

$$I_{rect\ XX} = I_{bridge\ footing\ XX} + 2I_{wing\ wall\ footing\ XX} \quad (27)$$

where

$$I_{rect\ XX} = LB^3/12 \quad (28)$$

$$I_{bridge\ footing\ XX} = LB_f^3/12 + LB_f(B/2 - B_f/2)^2 \quad (29)$$

$$I_{wing\ wall\ footing\ XX} = B_wL_w^3/12 + L_wB_w(B_f + L_w/2 - B/2)^2 \quad (30)$$

B, B_f, B_w, L and L_w are defined in Figure 39. B was estimated to be 15.7 ft using equations 27 through 30.

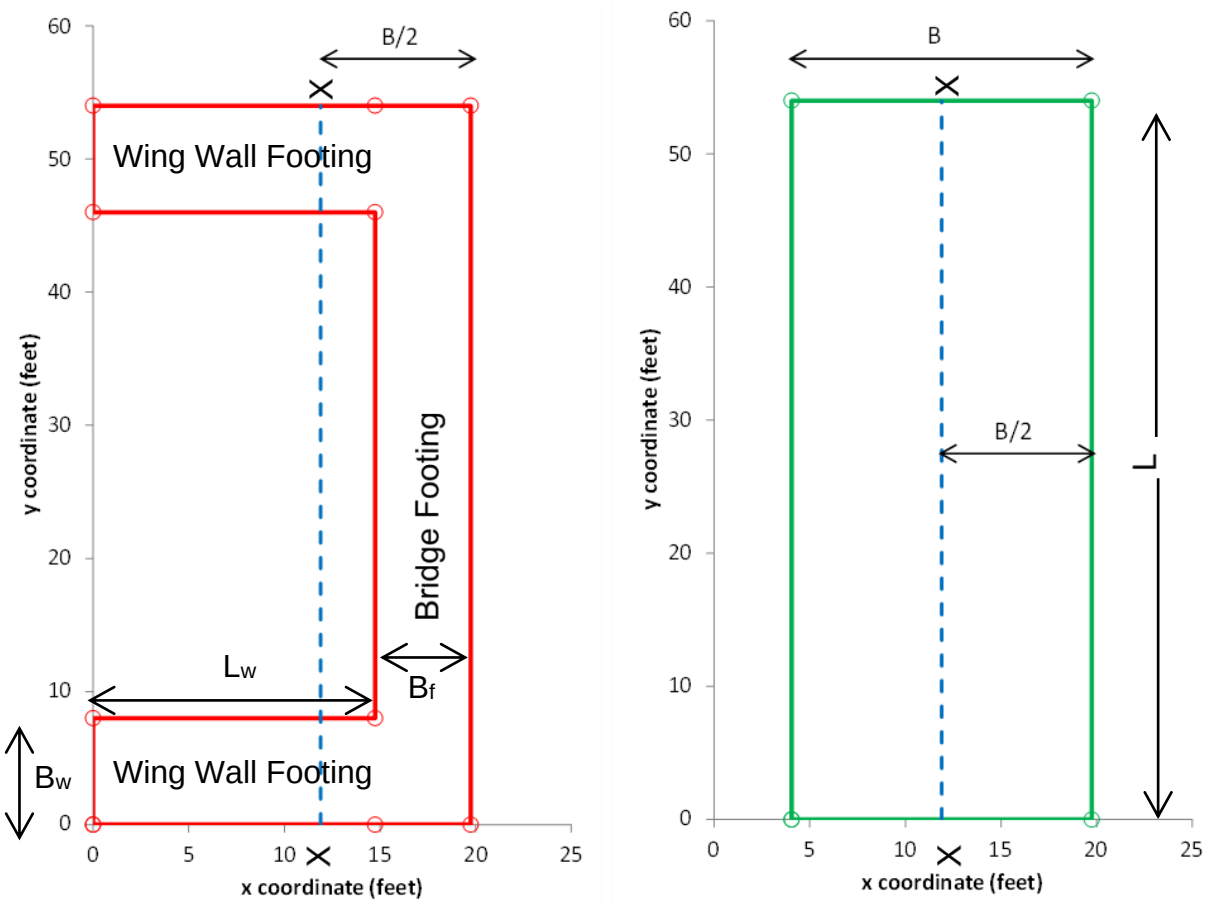

Figure 39 Equivalent rectangular footing to replace wing wall and abutment footings

The numerical analysis was rerun using this equivalent rectangular footing. Figure 40 shows the vertical pressures along the right-most 5 ft of the equivalent footing. It can be seen that the vertical pressures at the toe, middle and heel of the footing are now all in phase just like the measured trend. However, there is another problem and that is the maximum footing pressure fluctuates between 3,500 and 4,800 psf corresponding to only a 1,300 psf fluctuation as opposed to the measured of 2,500 – 3,000 psf.

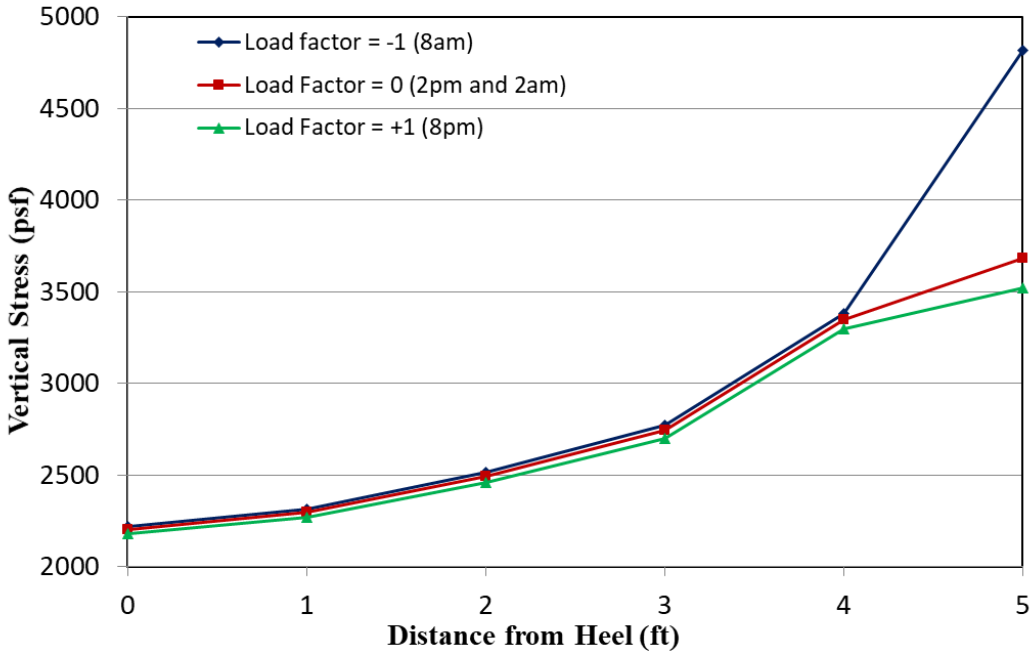

Figure 40 Vertical stresses of the right-most 5 ft of the equivalent footing at load factors -1, 0 and +1

5.1.2 Modification of Bearing Stresses from Equivalent Footing Model

From the numerical analysis, the vertical pressures on the right-most 5 ft of the equivalent footing (especially at the middle and heel) are too low compared to the measured values (Figure 41). This is because the area of the equivalent rectangular footing (right hand side of Figure 39) is bigger than the combined area of the wing wall and abutment footings by a factor of 1.675 even though they have identical stiffnesses. To compare the calculated and measured pressures on an even keel, the calculated pressures at the locations of the toe, middle and heel of the original 5-ft-wide footing are multiplied by 1.675 and replotted as a function of time in Figure 42 (a, b and c) along with the measured values.

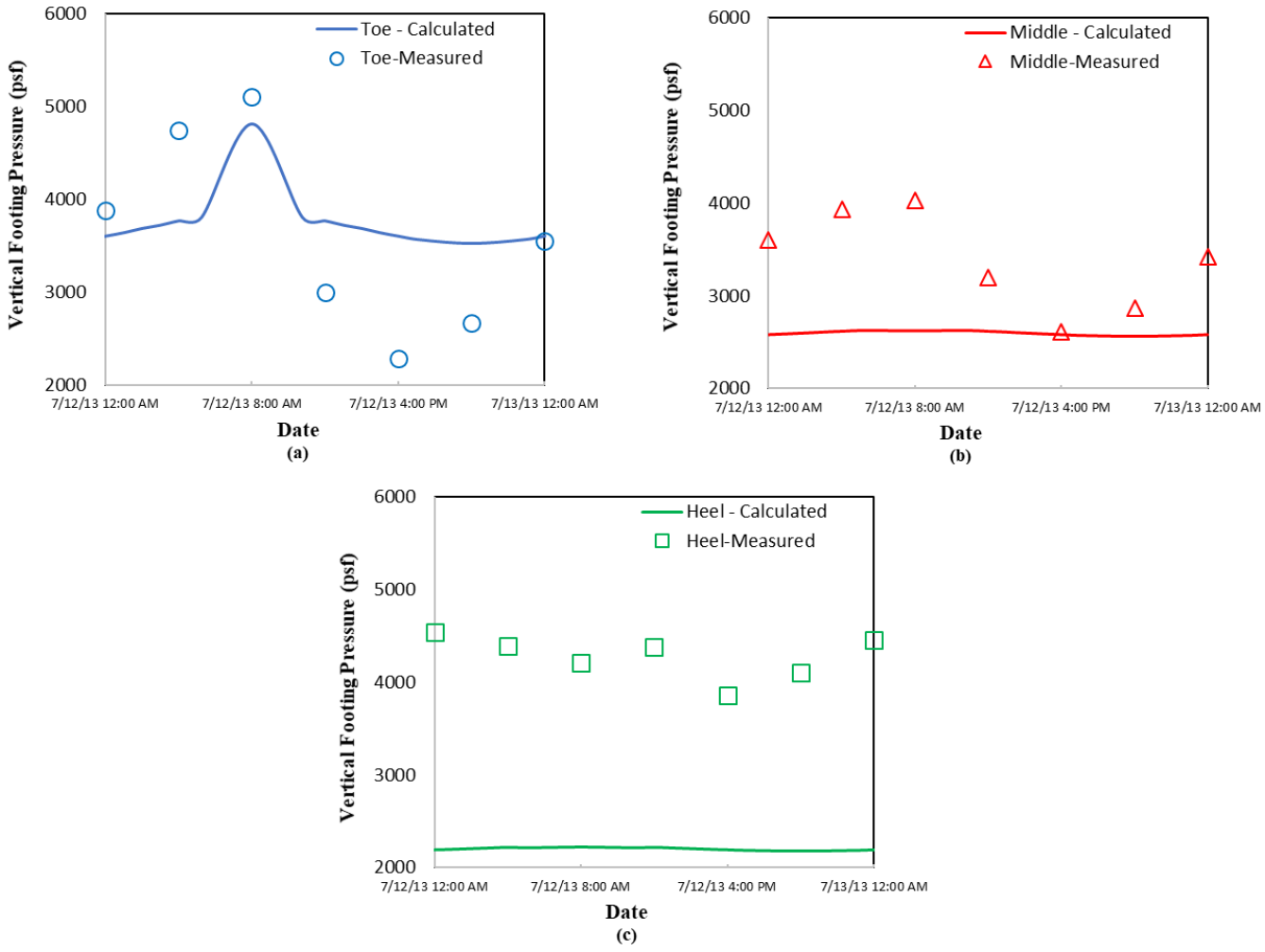

Figure 41 Calculated and measured vertical pressures of the right-most 5 ft of the equivalent footing before applying 1.675 correction factor at the (a) toe, (b) middle and (c) heel

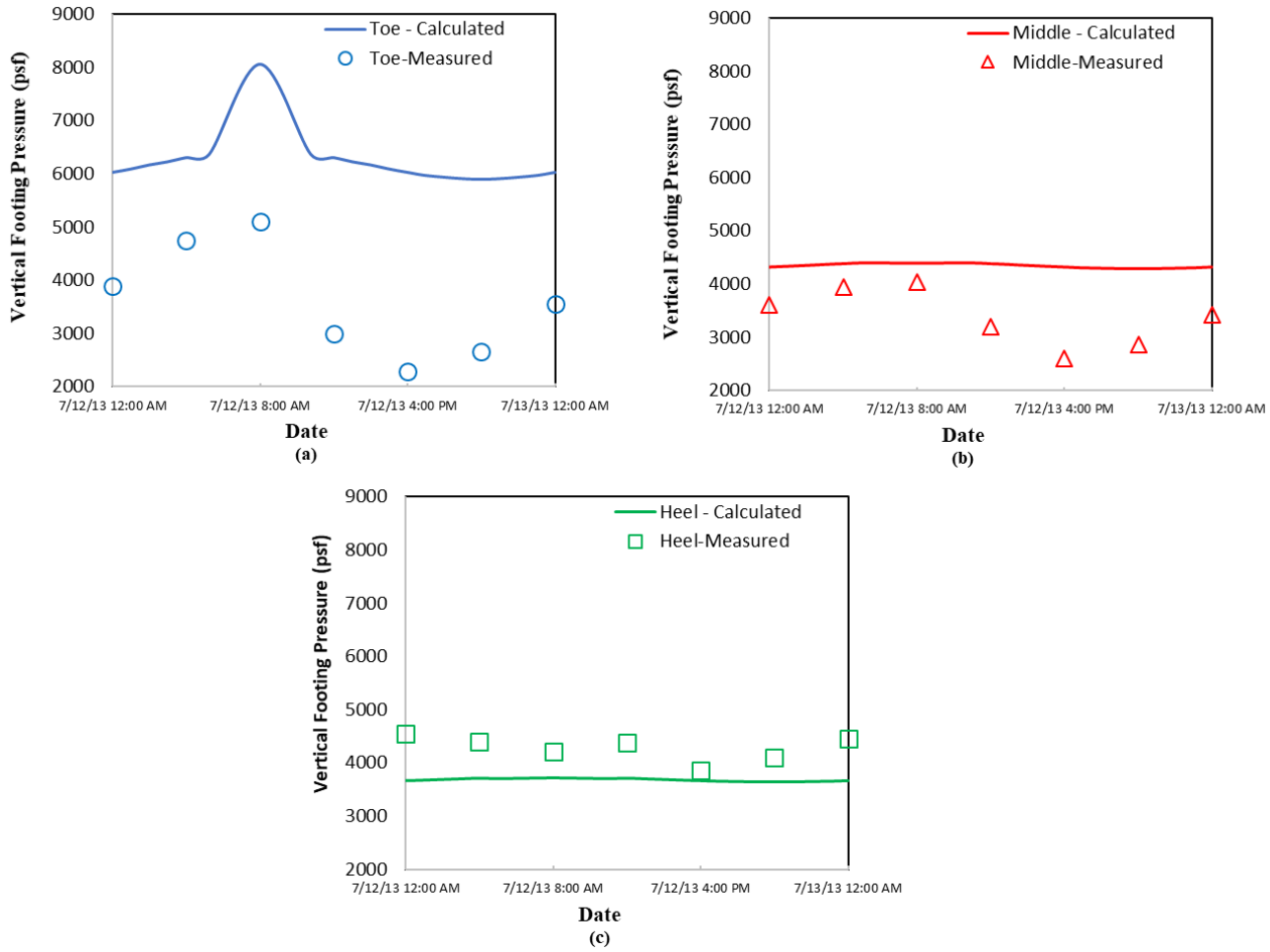

Figure 42 Calculated and measured vertical pressures of the right-most 5 ft of the equivalent footing after applying 1.675 correction factor at the (a) toe, (b) middle and (c) heel

5.2 Application of Measured Superstructure Strains

Calculated pressures depicted in Figure 42 still do not adequately capture the trends and fluctuation of the measured values (Figure 42). Specifically, the calculated pressure fluctuation at the toe of the footing, when applying measured temperature, is 2,169 psf, which is still not in the measured range of 2,500 psf – 3,000 psf. The reason has already been previously explained. Thus, in an attempt to obtain a more accurate analysis, measured superstructure strains were input to the model in terms of equivalent values of initial and final temperatures and gradients as described in Section 4.7.

By applying measured strains, calculated vertical pressures beneath the footing have better correlation with the measured field values as shown in Figure 43.

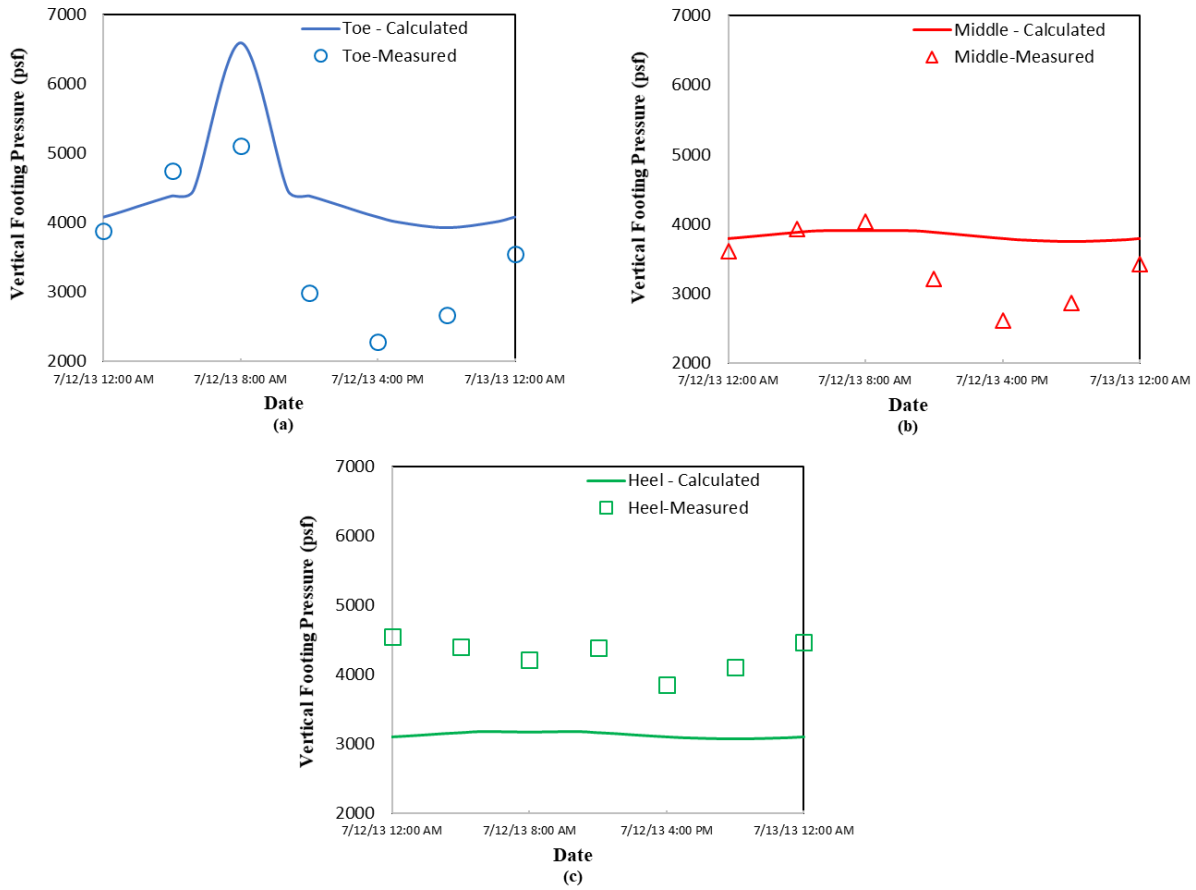

Figure 43 Calculated and measured vertical pressures of the right-most 5 ft of the equivalent footing after application of measured strains at the (a) toe, (b) middle and(c) heel

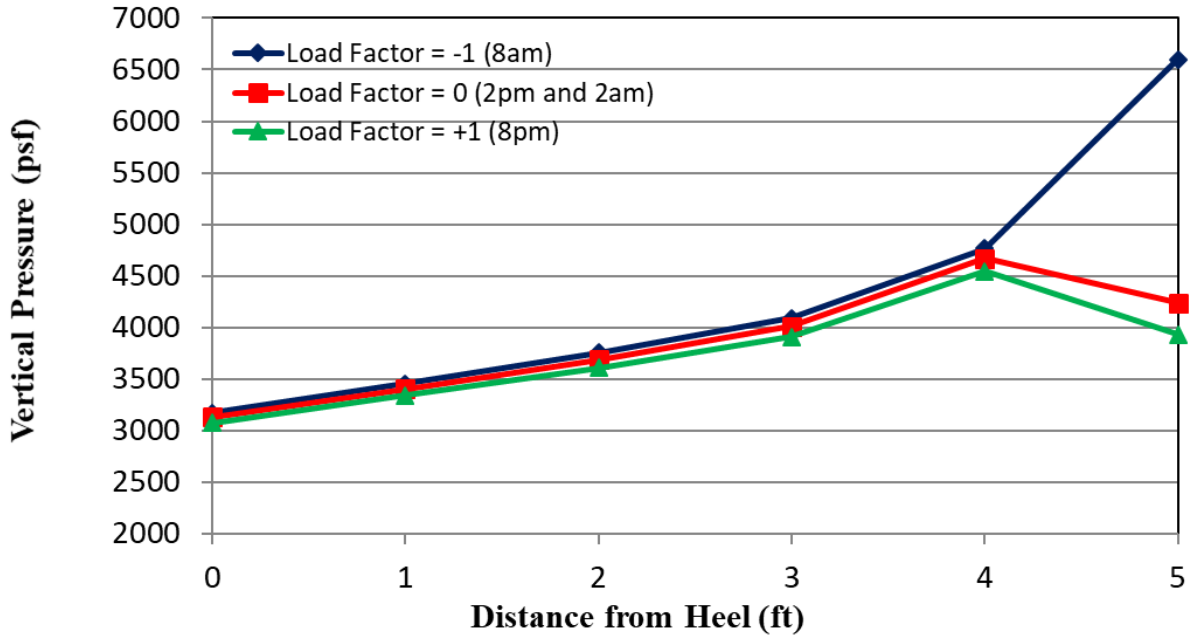

Figure 44 Vertical pressures of the right-most 5 ft of the equivalent footing at load factors -1, 0 and +1 after application of strains with 1.675 correction factor

Figures 43 and 44 shows that:

1. Using an equivalent rectangular footing, the model can replicate the cyclic behavior of the bridge due to thermal-induced axial load and bending.
2. After applying the adjustment factor of 1.675, the average footing pressure over the right-most 5-ft of the equivalent footing is about 4,000 psf, approximately equal to the average dead load stress.
3. The toe, middle and heel pressures are all in phase (Figure 44); i.e.; they all go up and down simultaneously indicating that the point of rotation during flexure lies outside the footing, consistent with the measured values.
4. The difference between the peak and trough vertical bearing pressures at the toe due to thermal effects is approximately 2,670 psf, in line with what was observed in the field (between 2,500 and 3,000 psf).
5. The pressures at the toe and middle tend to be over-estimated while the pressures at the heel appear to be underestimated. It is surmised that this may be due to the fact that the bridge was idealized to be flat when in fact it has a 0.5% slope down to this abutment.

The calculated peaks and troughs of the lateral pressures behind the end wall (figures 45a through 45c) follow the measured trend although they are less pronounced. However, the

calculated end wall lateral pressures are on average within the range of the measured values, which lends credence to the analysis methodology.

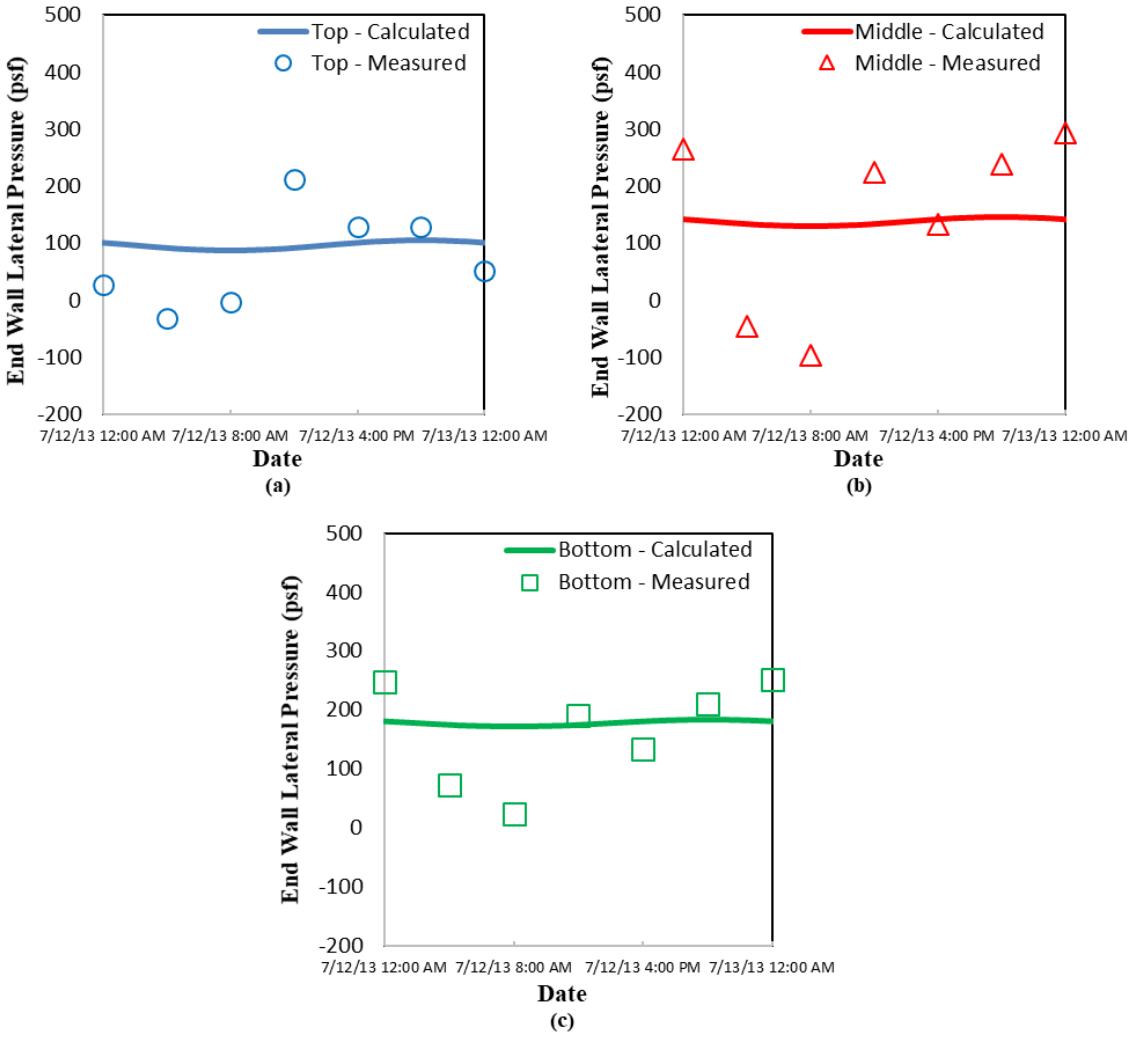

Figure 45 Calculated and measured end wall lateral pressures at (a) top, (b) middle and (c) bottom

While the fit between calculated and measured values in figures 43 through 45 may not be perfect, the key behavioral elements of the bridge footing and end wall have been captured despite using a simple 2D analysis with soil stiffness parameters derived based on widely published values (Duncan et al., 1980) rather than experimental (triaxial test) data. It is worth mentioning that to test the GW backfill, a 7.5-inch diameter triaxial specimen is needed [assume sample is not scalped or the parallel gradation technique (Lowe, 1964; Marachi et al., 1972; Verdugo et al., 2003; Varadajan et al., 2003; Verdugo and Hoz, 2006) is not utilized] because the maximum particle size is 1.25 inches. Testing of such large size specimens is beyond the scope of this work.

5.2.1 CMU Lateral Pressures and Deflection

The model with the 15.7-ft-wide equivalent footing underestimated the vertical pressures by a factor of 1.675. Consequently, the calculated CMU lateral pressures and deflections will also be underestimated. It is not easy to obtain a correction factor to apply to the CMU lateral pressures and deflections from the 15.7-ft-wide equivalent footing analysis, but as a crude approximation, the lateral behavior of the CMU for the original 5-ft-wide footing model subjected to "measured strains" can be viewed in the absence of results from a more reliable model. They are plotted in figures 46 and 47, which show that the lateral pressures and deflections of the CMU blocks followed the trends and values of the instrumentation results quite reasonably well. This agreement is not surprising since the only fault with the 5-ft-wide footing analysis is that the point of rotation lies incorrectly within the footing but the toe pressures, which should influence the CMU lateral pressures and deflections most, are trending reasonably correctly in terms of magnitude over a 24-hour cycle.

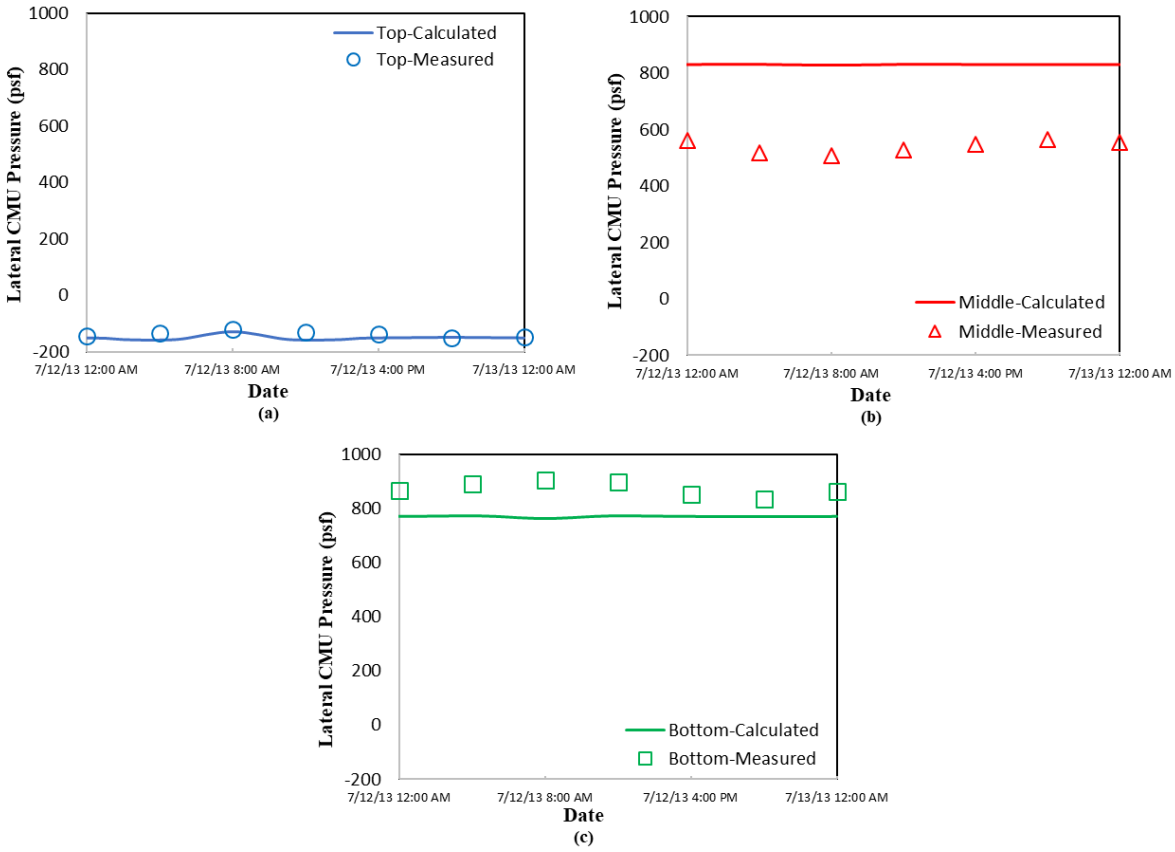

Figure 46 Calculated and measured CMU lateral pressures at (a) top, (b) middle and (c) bottom

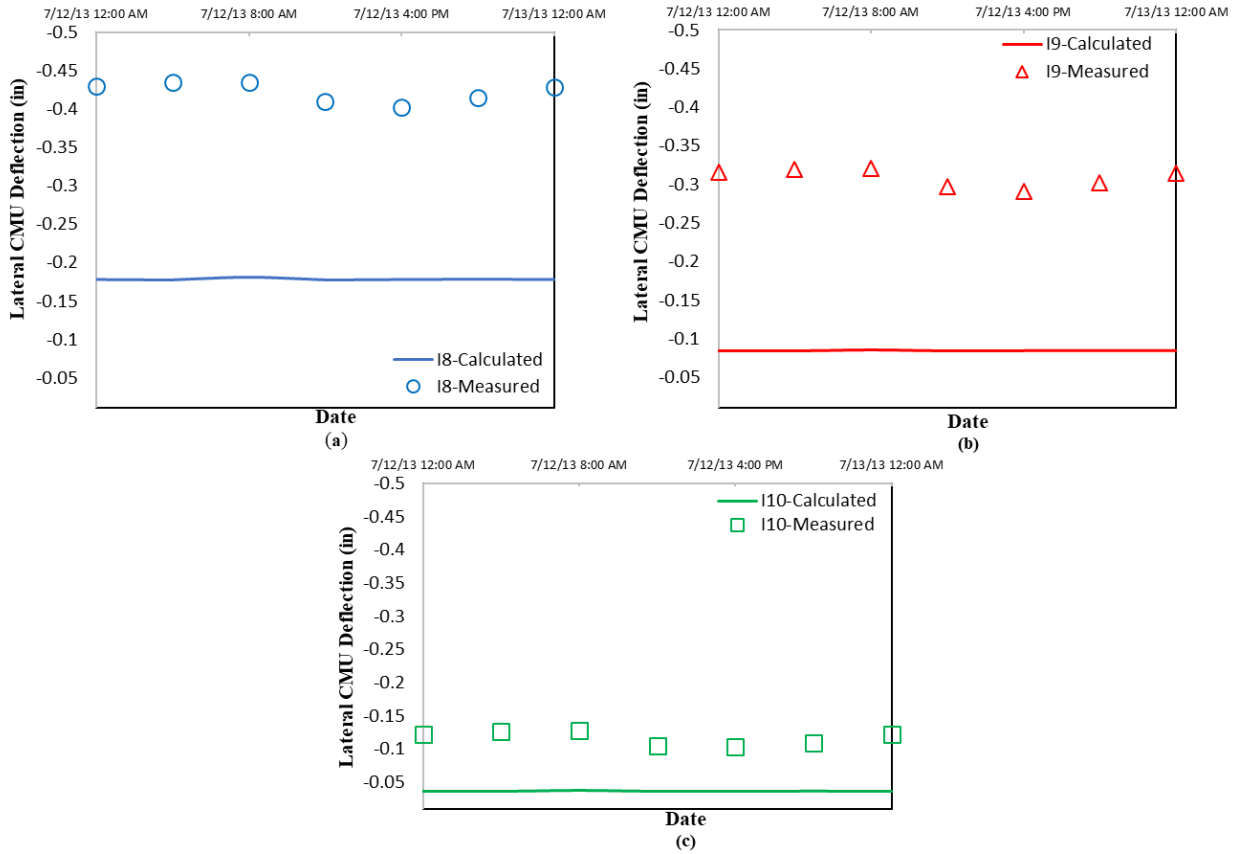

Figure 47 Calculated and measured CMU lateral deflection at inclinometers (a) I8, (b) I9 and (c) I10

6 INVESTIGATION OF THERMAL EFFECTS ON THE BEHAVIOR OF THE BRIDGE WITH A LONGER SPAN

FHWA (Adams et al., 2011) currently suggests a maximum span length of 140-ft for a GRS-IBS. This is because it is generally believed that the longer the span length, the more severe the thermal effects will be on the bridge behavior. In Section 5, numerical analyses results of the 110-ft-long Kauaula Stream bridge were discussed. The bearing pressures due to thermal loading were deemed acceptable. This section presents the behavior of a similar GRS-IBS with the span length doubled to 220-ft. Modifications to the 110-ft-span model are minimized for the sake of simplicity. The modifications are described along with a discussion of the results of the analysis.

6.1 Modified Numerical Model

For a bridge with a rectangular cross-section, doubling the superstructure span requires its depth to be doubled to keep the maximum stresses in the superstructure constant. Since redesigning the cross-section of the tub girder and the geometry of the numerical model is time consuming, the same cross-section was used but its span was doubled to study the thermal effects on a 220-ft-long GRS-IBS. The following assumptions/modifications are necessary:

1. The tub girder depth is doubled. This is a conservative modification since a properly redesigned tub girder depth would be slightly less than double because the tub cross-section is more efficient in resisting bending than a rectangular cross-section;

2. The moment of inertia of the bridge superstructure is assumed to be 8 times more. While this amplification factor is true for a rectangular cross-section since $I = \frac{BD^3}{12}$, where *B* and *D* are width and depth of the rectangle and since doubling *D* results in *I* increasing eight-fold, it should be less for a tub for the same reason as discussed in Item 1 above.

Superstructure

The span of the superstructure, which is assumed to be the distance between the front faces of the end walls, was increased by stretching the bridge stick model from 110-ft to 220-ft. Like the 110-ft GRS-IBS, only half the span length is analyzed since the bridge is assumed to be symmetrical. Since the stick model remained unchanged, the unit weight of the superstructure was doubled and its moment of inertia increased eight-fold to account for the deeper cross-section.

End Wall and Concrete Clamps

The heights of the end wall and concrete clamps have to be also doubled to be consistent with the tub girder, but they were not since the same superstructure model for the 110-ft-long GRS-IBS was utilized. Instead, the unit weight of the end wall was doubled. To analyze bending with the correct flexural stiffness, the Young's modulus of the end wall was multiplied by 8 since the

height is half of what it should be. Just as in the 110-ft model, the thickness of the end wall was maintained at 2.5 ft. The back face of the end wall coincides with the heel of the footing.

The concrete clamps were assigned a zero unit weight since the unit weight of the stick model has already been doubled and since the stick model is embedded in the clamps. The Young's modulus of the clamps was recalculated to be 1.27 X 10^9 psf using Equation 13.

Approach Fill and Abutment Fill

Consistent with a doubling of the tub girder depth, the height of the approach fill should theoretically also be doubled. Since the same height of the approach fill is utilized in the 220-ft-long model, the unit weight of the approach fill was doubled. Consequently, the Young's moduli of both the approach fill and the GRS abutment fill were modified since E_{50} is dependent on the confining stress/height. Figure 48 shows the revised linear regression parameters for the Young's modulus above the footing (approach fill) and below the footing (GRS abutment fill) where the approach fill height has been doubled.

In Figure 48, the top of the approach fill is at elevation 0 ft whereas in the LUSAS model, the elevation of the bottom of the footing is set at 0 ft. To account for the 15.891 ft difference in reference elevation, E_{50} was input as E_{50} = 29.85 (7.95 - z) + 130 and E_{50} = 7.97 (15.891 - z) + 220 for the approach fill and GRS abutment fill, respectively. It should be noted that, in LUSAS, z is positive above the footing and negative below the footing.

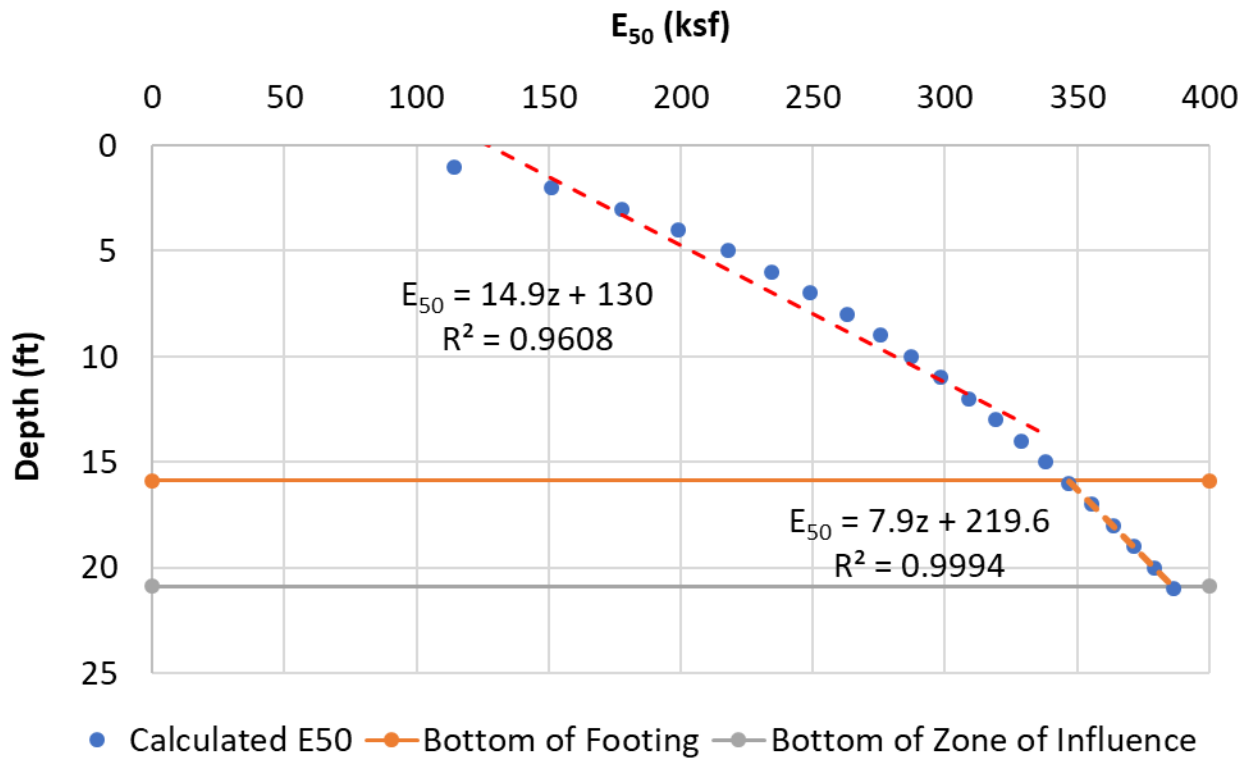

Figure 48 Linear regression of E_{50} vs. depth (z) for 220-ft-span bridge

Joint Elements

With an increase in the height of the approach fill, the vertical stresses and, consequently, the horizontal stresses also increase. This affects the stiffnesses of all joint elements except for those at the CMU-geotextile and CMU-riprap interfaces. Thus, the joint element stiffnesses were recalculated in accordance with Equation 12 by adjusting σ accordingly.

Application of Initial and Final Temperature Gradient

Since the cross-sectional geometry of the 110-ft model was used to represent the 220-ft span GRS-IBS, values of the initial and final temperature and gradient from the 110-ft model are also applicable to the longer span counterpart.

If the temperatures and gradients were applied along the entire stick model, tensile stresses were observed in the lower clamp elements. This is deemed unreasonable because the weight of the bridge "stick" should cause mostly compression (negative stresses) in the lower clamp elements but instead, tension (positive stress) was observed in these elements. It was found that this tension can be eliminated by applying the temperature and gradient only to the unclamped portion of the superstructure. Figure 49 shows the results. It can be observed that compressive stress prevails throughout the lower clamp apart from the portion of the clamp above the toe of the footing and in the end wall.

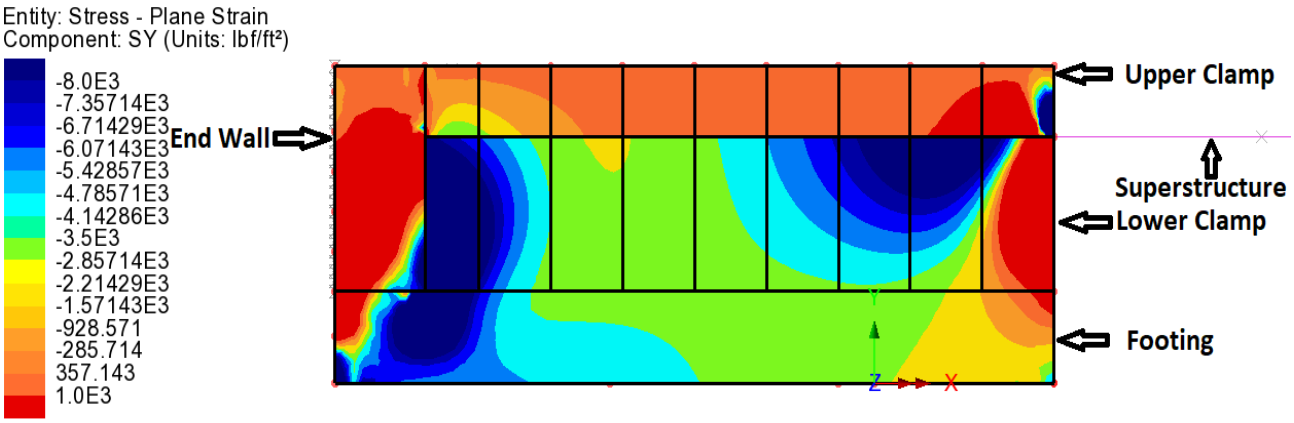

Figure 49 Stress distribution in the upper and lower clamps and end wall

Footing

The footing was 5-ft-wide for the 110-ft-span GRS-IBS. The footing was widened to 20-ft for the 220-ft-long GRS-IBS. Since both the superstructure height and span length were doubled, the footing width was quadrupled to yield approximately the same average bearing pressure as that of the 110-ft bridge model. An average bearing pressure of close to 4,000 psf (4,586 psf) on the GRS was roughly preserved for the longer span bridge.

Wing Wall Footing and Equivalent Rectangular Footing

To take into account the additional stiffness provided by the wing wall footings, the same wing wall dimensions and footings for the 110-ft-long model was assumed for the 220-ft-long model. An equivalent rectangular footing width was recalculated using equations 27 through 30 with B_f (Figure 39) = 20 ft. The equivalent rectangular footing was calculated to be 28.1-ft wide, yielding a corresponding area correction factor of 1.153. This factor was used to scale the bearing pressures for the 28.1-ft wide equivalent rectangular footing to that for the 20-ft-wide abutment footing plus the two wing wall footings.

6.2 Results

Figure 50 shows the vertical pressure along the rightmost 20-ft of the equivalent footing corresponding to the "actual" footing. The three curves represent the three different load factors of -1 (8 a.m.), 0 (2p.m. and 2 a.m.), and +1 (8 p.m.). The vertical pressures at the toe, middle and heel of the footings for the 110-ft-long and 220-ft-long bridges are plotted for comparison in Figure 51.

The following points can be observed from figures 50 and 51.

1. Unlike the 110-ft-long GRS-IBS, the point of rotation for the 220-ft-long GRS-IBS remained within the footing footprint. Figure 50 shows that the toe and heel pressures are out of phase and the point of rotation is located about 6 ft from the heel. This suggests that the bending stiffness attributed to the wing wall footings is smaller for the 220-ft span bridge. This is reasonable since the width of the abutment footing has increased four-fold in the longer span bridge implying a smaller contribution of the wing wall footing to the overall foundation bending stiffness.

2. Unlike the 110-ft-long GRS-IBS, the pressure diagram is now loaded more heavily at the heel (Figure 50) as opposed to being toe-heavy for the 110-ft-long GRS-IBS (Figure 44). This is probably due to the twice as tall end wall exerting its presence at the heel and the smaller relative contribution of the wing wall footings to the bridge's rotational behavior in the longer span model.

3. After applying the correction factor of 1.153, the average footing pressure over the right-most 20-ft of the equivalent footing is still roughly about 4,000 psf (4,586 psf).

4. The difference between the peak and trough vertical bearing pressure at the toe due to thermal effects is approximately 3,450 psf which is only slightly higher than in the 110-ft-long GRS-IBS. This pressure fluctuation in the GRS abutment fill is still below the shakedown limit based on the permanent deformation tests by Song and Ooi (2010).

From the analysis results, it can be seen that GRS abutments are able to support a 220-ft span bridge without exceeding the shakedown limit (> 4,380 psf). Therefore, GRS-IBS of a similar

variety with span lengths longer than the 140-ft limit as suggested by FHWA (Adams et al., 2011) can be safely used in portions of Hawaii with a climate similar to Lahaina.

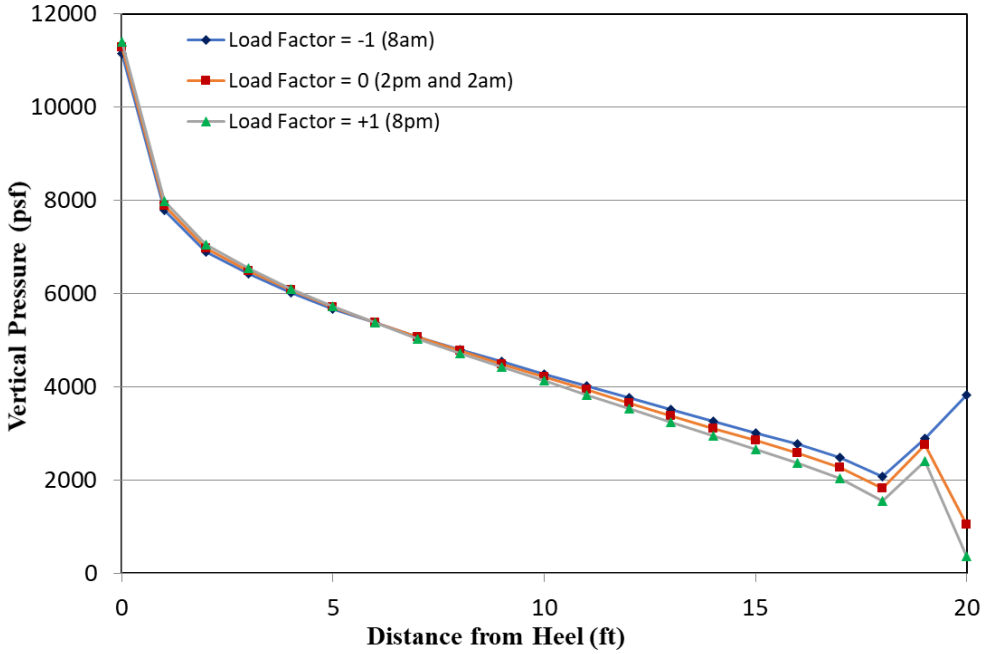

Figure 50 Calculated vertical pressures along the rightmost 20-ft of the equivalent footing at load factors -1, 0 and +1

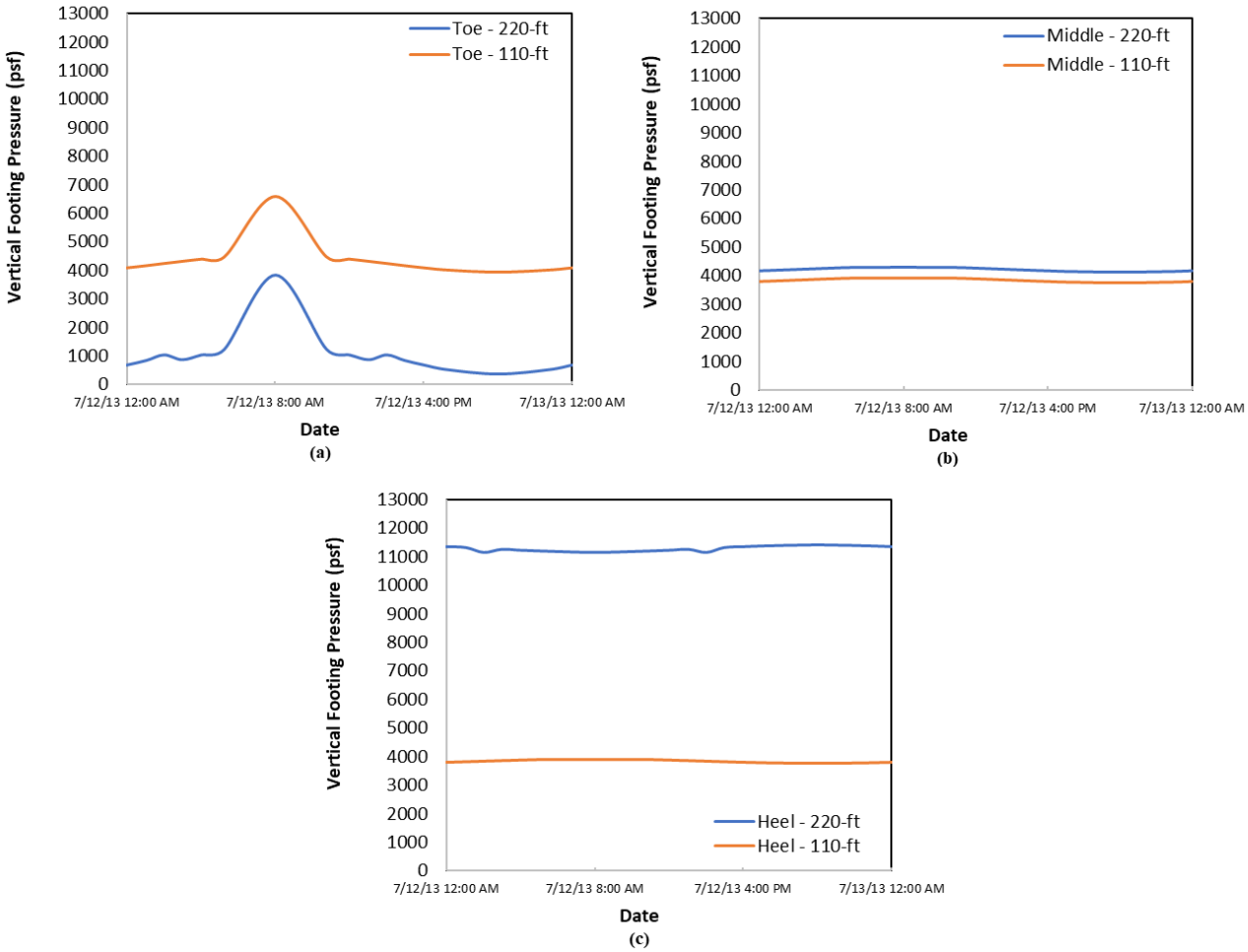

Figure 51 Calculated vertical pressures at (a) toe, (b) middle and (c) heel of the footing for 110-ft-long and 220-ft-long bridges

7 SUMMARY AND CONCLUSION

7.1 Project Summary

A methodology has been presented to analyze a GRS-IBS in Hawaii that was observed to undergo cyclic straining of the superstructure due to meteorological factors. The upper and lower reaches of the superstructure saw the highest and lowest strain fluctuation, respectively. These non-uniform strains impose not only axial loading on the superstructure but also bending, which in turn caused the vertical pressures beneath the footing and lateral pressures behind the end walls and facing to fluctuate cyclically as well. Measured vertical footing pressure closest to the stream experienced the greatest daily pressure fluctuation (≈ 2,500 – 3,000 psf), while the one nearest the end wall experienced the least. A finite element analysis of the same bridge was performed by applying an equivalent temperature and gradient to the superstructure over the coldest and hottest periods of a day to simulate the axial load and bending cycles to see if the field measured values of pressures are reasonable and verifiable. This methodology is novel in the sense that the effects of axial load and bending of the superstructure are simulated using measured strains rather than measured temperatures. The measured strains embody the effects of volume and shape changes in the superstructure concrete, the effects of temperature lag over the bridge depth and the associated changes of the forces in the post-tensioning tendons.

7.2 Conclusions on Bearing Pressures

The following conclusions are offered from this analysis:

1. Application of measured temperatures yield bearing pressures lower than measured in the GRS-IBS footing. Application of measured strains was found to yield bearing pressures more consistent with measured values.

2. An equivalent rectangular footing can substitute for an abutment and two wing wall footings to numerically model the thermally induced cyclic behavior of a GRS-IBS provided an appropriate area correction factor is applied to yield an average footing pressure equal to the average dead load stress.

3. The toe, middle and heel pressures are all in phase; i.e.; they all go up and down simultaneously indicating that the point of rotation during flexure lies outside the footing, consistent with the measured values.

4. The difference between the peak and trough vertical bearing pressures at the toe due to thermal effects is in line with what was observed in the field.

5. The pressures at the toe and middle tend to be over-estimated while the pressures at the heel appear to be underestimated. It is surmised that this may be due to the fact that the bridge was idealized to be flat when in fact it has a 0.5% slope down to this abutment.

7.3 Conclusions on CMU Lateral Pressures and Deflections

The lateral behavior of the CMU blocks cannot be garnered from the analysis with the equivalent rectangular footing because the vertical pressures in the GRS are underestimated. Even though the equivalent rectangular footing has the same stiffness as the abutment footing and the two wing wall footings, it has a larger footing area. The adjustment factor for vertical stress is simply the ratio of the sum of the areas of the wing wall and abutment footings to that of the equivalent rectangular footing. However, the same factor cannot be applied to correct the horizontal stresses in the CMU.

In lieu of results from a more reliable model, the lateral behavior of the CMU can be approximated by looking at the results of the numerical analysis for the 5-ft-wide footing without the wing walls. Even though the point of rotation for this analysis lies incorrectly within the footing, the toe pressures trend reasonably correctly. Since the toe pressures influence the CMU behavior the most due to their proximity, the lateral behavior of the CMU can be garnered from the results of the analysis with the 5-ft-wide footing. The calculated lateral pressures and deflections of the CMU blocks followed the trends and values of the instrumentation results reasonably well. This agreement is not surprising since the toe pressures, which influence the CMU lateral pressures and deflections most, are trending reasonably correctly in terms of magnitude over a 24-hour cycle. This lends credence to the analysis methodology.

7.4 Conclusions on Thermal Effects on a Bridge with a Longer Span

The analysis of the longer span bridge also shows that the GRS abutment does not exceed its shake down limit of 4,380 psf. Thus, the same variety of GRS-IBS can be used to support a superstructure with a span length of 220-ft in weather conditions similar to Lahaina, Maui.

7.5 Main Contributions

The simple methodology of using measured strains instead of measured temperature and a coefficient of thermal expansion adopted and described herein can be useful to engineers who are interested in estimating thermally induced cyclic bearing pressures of GRS-IBS and the associated cyclic-induced settlement in a GRS abutment.

7.6 Recommendations for Future Studies

The study of thermal effects on a longer span GRS-IBS was performed by making some simplifying assumptions since redesigning the cross-section of the tub girder and the geometry of the numerical model is time consuming. The same stick model for the 110-ft-long span was used in the 220-ft-long analysis. For a bridge with a rectangular cross-section, doubling the superstructure span requires its depth to be doubled to keep the maximum stresses in the superstructure constant. This doubling is a conservative modification since a properly redesigned tub girder depth would be slightly less than double because the tub cross-section is more efficient in resisting bending than a rectangular cross-section. Also, the moment of inertia of the bridge superstructure is assumed to be 8 times more. The unit weight of the GRS

approach fill was also doubled because its height remained the same as the 110-ft model. A properly redesigned superstructure should ideally be utilized for the 220-ft-span GRS-IBS with a higher approach fill to more correctly investigate thermal effects on increased span length.

8 REFRENCES

Adams, M., Nicks, J., Stabile, T., Wu, J., Schlatter, W. and Hartmann, J. (2011). *Geosynthetic Reinforced Soil Integrated Bridge System—Interim Implementation Guide* (No. FHWA-HRT-11-026;). Retrieved from Federal Highway Administration website: https://www.fhwa.dot.gov/publications/research/infrastructure/structures/11026/11026.pdf

Alzamora, D. (2018). Turning skeptics into adopters. *Public Roads*, *82*, 36–41.

Bolton, M. D. (1986). The strength and dilatancy of sands. *Géotechnique*, *36*(1), 65–78. https://doi.org/10.1680/geot.1986.36.1.65

Christopher, B.R., Holtz, R.D. and Bell, W.D. (1986). New tests to determine the in-soil stress-strain properties of geotextiles. *Proceedings of the third International Conference on Geotextile.* Vienna, Austria, 683-688.

Duncan, J. M., Byrne, P., Wong, K. S. and Mabry, P. (1980). *Strength, Stress-Strain and Bulk Modulus Parameters for Finite Element Analyses of Stresses and Movements in Soil Masses*. Berkeley, Calif: College of Engineering, Office of Research Services, University of California.

Duncan, J. M. and Chang, C.-Y. (1970). Nonlinear Analysis of Stress and Strain in Soils. *Journal of the Soil Mechanics and Foundations Division*, *96*(5), 1629–1653.

Hirata and Associates, Inc. (2009). Geotechnical Investigation Honoapiilani Highway Realignment, Phase 1B-1 from Lahainaluna Road To Hokiokio Place Lahaina, Maui, Hawaii.

Kokkalis, A. and Papacharisis, N. (1989). Simple laboratory method to estimate the in-soil behaviour of geotextiles. *Geotextiles and Geomembranes*, *8*, 147–157. https://doi.org/10.1016/0266-1144(89)90025-3

KSF, Inc. (2011). Honoapiilani Highway Realignment Phase 1B-1, Lahainaluna Road to Hokiokio Place. Value Engineered Design Drawings.

Ling, H. I., Wu, J. T. H. and Tatsuoka, F. (1992). Short-term strength and deformation characteristics of geotextiles under typical operational conditions. *International Journal of Rock Mechanics and Mining Sciences and Geomechanics Abstracts*, *29*(6), 185–219. https://doi.org/10.1016/0148-9062(92)91916-S

Lowe, J. (1964) Shear strength of coarse embankment dam material. *Procs., 8th Congress on Large Dams*, 745-761.

LUSAS. (2016) Modeler reference manual Version 15.2. London, UK: Author.

Marschi, N. D., Chan, C. K. and Seed, H. B. (1972). Evaluation of Properties of Rockfill Materials. *Journal of the Soil Mechanics and Foundations Division*, *98*(1), 95–114.

McGown, A., Andrawes, K.Z. and Kabir, M.H. (1982). Load -Extension Testing of Geotextiles Confined In-Soil. *Procs., 2nd International Conference on Geotextile*, Las Vegas, U.S.A., 793-798.

Nakai, T. (2013). *Constitutive modeling of geomaterials: Principles and applications*. Boca Raton: Taylor & Francis.

Ooi, P.S.K., Adams, M.T. and Lawrence, J.B. (2019a). Behavior of a geosynthetic reinforced soil integrated bridge system due to thermal effects. *Proc., Geosynthetics*.

Ooi, P. S. K., Adams, M. T. and Lawrence, J. B. (2019b). Long-Term Behavior of a Geosynthetic Reinforced Soil Integrated Bridge System in Hawaii. *Transportation Research Record*, *2673*(2), 571–582.

PLAXIS. (2014) Material Models Manual. Netherlands: Author.

Potyondy, J. G. (1961). Skin Friction between Various Soils and Construction Materials. *Géotechnique*, *11*(4), 339–353. https://doi.org/10.1680/geot.1961.11.4.339

Song, Y. and Ooi, P.S,K. (2010). Interpretation of Shakedown Limit from Multistage Permanent Deformation Tests. *Transportation Research Record: Journal of the Transportation Research Board*, *2167*(1), 72-82.

Tencate. (2014) Tencate Mirafi PET70/70 specification sheet. Accessed 2014.

Varadarajan, A., Sharma, K. G., Venkatachalam, K. and Gupta, A. K. (2003). Testing and Modeling Two Rockfill Materials. *Journal of Geotechnical and Geoenvironmental Engineering*, *129*(3), 206–218. https://doi.org/10.1061/(ASCE)1090-0241(2003)129:3(206).

Verdugo, R. and De La Hoz, K. (2006). Strength and stiffness of coarse granular soils. *Procs., Geotechnical Symposium*, Rome, March 16 & 17.

Verdugo, R., Gesche, R. and De La Hoz, K.(2003). Metodologia de evaluacion de parametros de Resistencia al corte de suelos granulares gruesos. *Procs., 12th Pan American Conference on Soil Mechanics & Geotechnical Engineering*, Cambridge, MA, Vol. 1. 691-696.

Werkmeister, S. (2003). *Permanent Deformation Behaviour of Unbound Granular Materials in Pavement Constructions*. Technische Universität Dresden.

APPENDIX A: BORING LOGS (HIRATA AND ASSOCIATES, 2009)

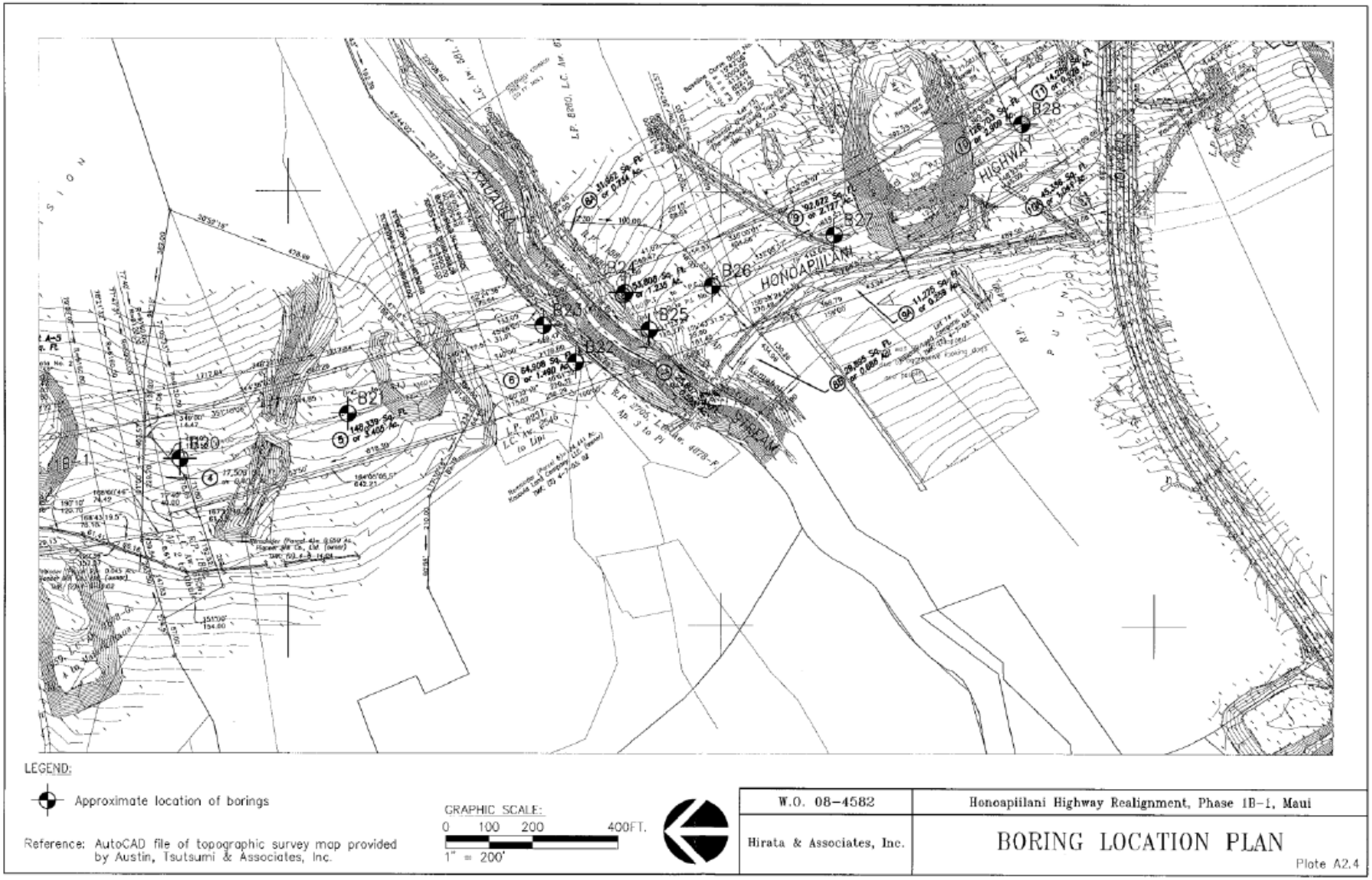

HIRATA & ASSOCIATES, INC.

BORING LOG

W.O. 08-4582

BORING NO. B22 DRIVING WT. 140 lb. START DATE 4/23/09
SURFACE ELEV. 116± DROP 30 in. END DATE 4/28/09

DEPTH	GRAPH	SAMPLE	BLOWS PER FOOT	DRY DENSITY (PCF)	MOIST. CONT. (%)	DESCRIPTION
0						Clayey SILT (ML) – Reddish brown, slightly moist, stiff, with sand and gravel. Boulder at one foot.
			19/6" 50/5"	95	6	
5			10/No Penetration			COBBLES AND BOULDERS – Mottled brown, dense to very dense, in a matrix of silt, sand, and gravel. (Older Alluvium) Begin HQ coring at 6 feet. 70% Recovery from 6 to 11 feet.
10						70% Recovery from 11 to 16 feet.
15			50/4" 10/No Penetration			88% Recovery from 16 to 21 feet.
20						72% Recovery from 21 to 26 feet.
25			10/No Penetration			88% Recovery from 26 to 31 feet.
30						COBBLES AND BOULDERS – Mottled brown, medium hard to hard, in a matrix of cemented silt, sand, and gravel. (Older Alluvium) Plate A4.31

HIRATA & ASSOCIATES, INC.

BORING LOG

W.O. 08-4582

BORING NO. B22 (Continued) DRIVING WT. 140 lb. START DATE 4/23/09
SURFACE ELEV. 116± DROP 30 in. END DATE 4/28/09

DEPTH	GRAPH	SAMPLE	BLOWS PER FOOT	DRY DENSITY (PCF)	MOIST. CONT. (%)	DESCRIPTION
30						35% Recovery from 31 to 36 feet.
35						100% Recovery from 36 to 41 feet.
40						
45						COBBLES AND BOULDERS – Mottled brown, dense to very dense, in a matrix of silt, sand, and gravel. (Older Alluvium) 70% Recovery from 41 to 46 feet.
50			10/No Penetration			COBBLES AND BOULDERS – Mottled brown, medium hard to hard, in a matrix of cemented silt, sand, and gravel. (Older Alluvium) 100% Recovery from 46 to 51 feet.
55						83% Recovery from 51 to 56 feet.
60			90/10"		26	COBBLES AND BOULDERS – Mottled gray, dense to very dense, in a matrix of silt, sand, and gravel. (Older Alluvium) 70% Recovery from 56 to 61 feet.

Plate A4.32

HIRATA & ASSOCIATES, INC.

BORING LOG

W.O. 08-4582

BORING NO. B22 (Continued) DRIVING WT. 140 lb. START DATE 4/23/09

SURFACE ELEV. 116± DROP 30 in. END DATE 4/28/09

DEPTH	GRAPH	SAMPLE	BLOWS PER FOOT	DRY DENSITY (PCF)	MOIST. CONT. (%)	DESCRIPTION
60			10/No Penetration			
						End boring at 61 feet.
						Neither groundwater nor seepage water encountered.
65						
70						
75						
80						
85						
90						

Plate A4.33

HIRATA & ASSOCIATES, INC.

BORING LOG

W.O. 08-4582

BORING NO. B23 DRIVING WT. 140 lb. START DATE 4/14/09
SURFACE ELEV. 120± DROP 30 in. END DATE 4/16/09

DEPTH	GRAPH	SAMPLE	BLOWS PER FOOT	DRY DENSITY (PCF)	MOIST. CONT. (%)	DESCRIPTION
0			18	84	8	Clayey SILT (ML) – Reddish brown, slightly moist, medium stiff to stiff, with sand and gravel.
			15	105	9	
5			10/No Penetration			COBBLES AND BOULDERS – Mottled brown, dense to very dense, in a matrix of silt, sand, and gravel. (Older Alluvium) Begin HQ coring at 5.5 feet. 47% Recovery from 5.5 to 8 feet.
						80% Recovery from 8 to 13 feet.
10						
						58% Recovery from 13 to 18 feet.
15						
						92% Recovery from 18 to 21 feet.
20						
						87% Recovery from 21 to 26 feet.
25						
						COBBLES AND BOULDERS – Mottled gray, medium hard to hard, in a matrix of cemented silt, sand, and gravel. (Older Alluvium) 90% Recovery from 26 to 31 feet.
30						Plate A4.34

HIRATA & ASSOCIATES, INC.

BORING LOG

W.O. 08-4582

BORING NO. B23 (Continued) DRIVING WT. 140 lb. START DATE 4/14/09

SURFACE ELEV. 120± DROP 30 in. END DATE 4/16/09

DEPTH	GRAPH	SAMPLE	BLOWS PER FOOT	DRY DENSITY (PCF)	MOIST. CONT. (%)	DESCRIPTION
30						90% Recovery from 31 to 36 feet.
35						100% Recovery from 36 to 41 feet.
40						100% Recovery from 41 to 46 feet.
45						100% Recovery from 46 to 51 feet.
50						100% Recovery from 51 to 56 feet.
55						100% Recovery from 56 to 61 feet.
60						

Plate A4.35

HIRATA & ASSOCIATES, INC.

BORING LOG

W.O. 08-4582

BORING NO. B23 (Continued) DRIVING WT. 140 lb. START DATE 4/14/09
SURFACE ELEV. 120± DROP 30 in. END DATE 4/16/09

DEPTH	GRAPH	SAMPLE	BLOWS PER FOOT	DRY DENSITY (PCF)	MOIST. CONT. (%)	DESCRIPTION
60						100% Recovery from 61 to 66 feet.
65						100% Recovery from 66 to 71 feet.
70						100% Recovery from 71 to 76 feet.
75						100% Recovery from 76 to 81 feet.
80						78% Recovery from 81 to 84 feet.
85						End boring at 84 feet. Neither groundwater nor seepage water encountered.
90						Plate A4.36

HIRATA & ASSOCIATES, INC.

BORING LOG

W.O. 08-4582

BORING NO. B24 DRIVING WT. 140 lb. START DATE 9/8/08

SURFACE ELEV. 116± DROP 30 in. END DATE 9/12/08

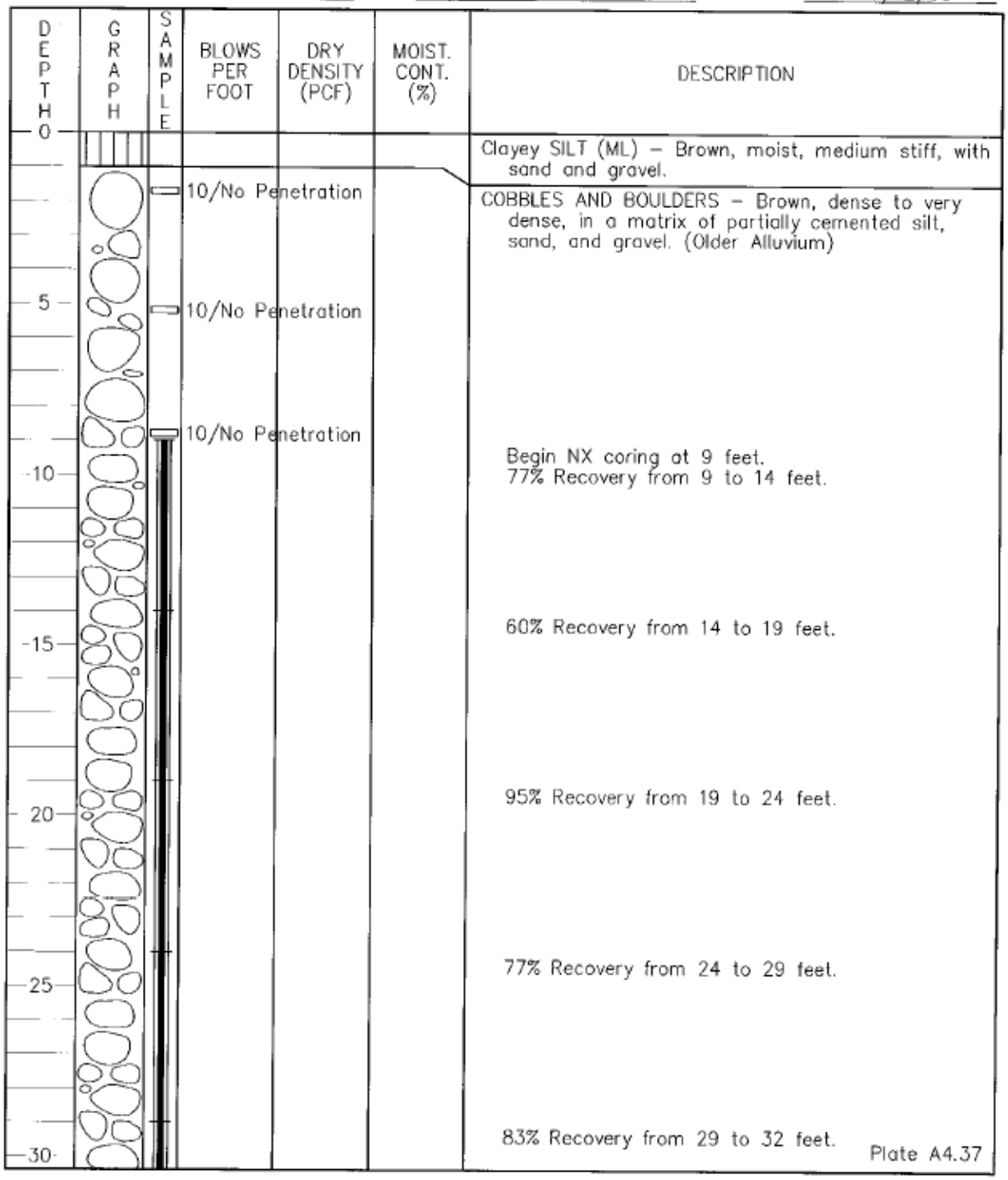

Plate A4.37

HIRATA & ASSOCIATES, INC.

BORING LOG

W.O. 08-4582

BORING NO. B24 (Continued) DRIVING WT. 140 lb. START DATE 9/8/08
SURFACE ELEV. 116± DROP 30 in. END DATE 9/12/08

DEPTH	GRAPH	SAMPLE	BLOWS PER FOOT	DRY DENSITY (PCF)	MOIST. CONT. (%)	DESCRIPTION
30						72% Recovery from 32 to 35 feet.
35						COBBLES AND BOULDERS – Mottled gray, medium hard to hard, in a matrix of cemented silt, sand, and gravel. (Older Alluvium) 78% Recovery from 35 to 40 feet.
40						COBBLES AND BOULDERS – Mottled brown, dense to very dense, in a matrix of silt, sand, and gravel. (Older Alluvium) 92% Recovery from 40 to 45 feet.
45						77% Recovery from 45 to 50 feet.
50						75% Recovery from 50 to 52 feet.
55						COBBLES AND BOULDERS – Mottled brown, medium hard to hard, in a matrix of cemented silt, sand, and gravel. (Older Alluvium) 97% Recovery from 52 to 55 feet. 95% Recovery from 55 to 60 feet.
60						Plate A4.38

HIRATA & ASSOCIATES, INC.

BORING LOG

W.O. 08-4582

BORING NO. B24 (Continued) DRIVING WT. 140 lb. START DATE 9/8/08

SURFACE ELEV. 116± DROP 30 in. END DATE 9/12/08

DEPTH	GRAPH	SAMPLE	BLOWS PER FOOT	DRY DENSITY (PCF)	MOIST. CONT. (%)	DESCRIPTION
60						100% Recovery from 60 to 65 feet.
65						100% Recovery from 65 to 70 feet.
70						100% Recovery from 70 to 75 feet.
75						100% Recovery from 75 to 80 feet.
80						COBBLES AND BOULDERS – Mottled brown, dense to very dense, in a matrix of silt, sand, and gravel. (Older Alluvium) 87% Recovery from 80 to 85 feet.
85						End boring at 85 feet. Neither groundwater nor seepage water encountered.
90						Plate A4.39

HIRATA & ASSOCIATES, INC.

BORING LOG

W.O. 08-4582

BORING NO. B25 DRIVING WT. 140 lb. START DATE 5/11/09

SURFACE ELEV. 111± DROP 30 in. END DATE 5/13/09

DEPTH	GRAPH	SAMPLE	BLOWS PER FOOT	DRY DENSITY (PCF)	MOIST. CONT. (%)	DESCRIPTION
0						Clayey SILT (ML) – Reddish brown, slightly moist, stiff, with sand and gravel.
			10/No Penetration			COBBLES AND BOULDERS – Mottled brown, dense to very dense, in a matrix of silt, sand, and gravel. Partially cemented from 2 to 10 feet, medium hard to hard. (Older Alluvium)
5						
10						Begin HQ coring at 9 feet. 70% Recovery from 9 to 14 feet.
15			12		31	
						100% Recovery from 16 to 19 feet.
20						100% Recovery from 19 to 24 feet.
25			50/2"		10	92% Recovery from 24 to 29 feet.
30			50/3"		12	67% Recovery from 29 to 34 feet.

Plate A4.40

HIRATA & ASSOCIATES, INC.

BORING LOG

W.O. 08-4582

BORING NO. B25 (Continued) DRIVING WT. 140 lb. START DATE 5/11/09

SURFACE ELEV. 111± DROP 30 in. END DATE 5/13/09

DEPTH	GRAPH	SAMPLE	BLOWS PER FOOT	DRY DENSITY (PCF)	MOIST. CONT. (%)	DESCRIPTION
30						
						58% Recovery from 34 to 39 feet.
35						
			10/No Penetration			92% Recovery from 39 to 44 feet.
40						
						70% Recovery from 44 to 49 feet.
45						
			25/6" 10/No Penetration		21	
50						83% Recovery from 50 to 54 feet.
55						83% Recovery from 54 to 59 feet.
60			10/No Penetration			COBBLES AND BOULDERS – Brown, medium hard to hard, in a matrix of cemented silt, sand, and gravel. (Older Alluvium) Plate A4.41

HIRATA & ASSOCIATES, INC.

BORING LOG

W.O. 08-4582

BORING NO. B25 (Continued) DRIVING WT. 140 lb. START DATE 5/11/09

SURFACE ELEV. 111± DROP 30 in. END DATE 5/13/09

DEPTH	GRAPH	SAMPLE	BLOWS PER FOOT	DRY DENSITY (PCF)	MOIST. CONT. (%)	DESCRIPTION
60						100% Recovery from 59 to 64 feet.
65						End boring at 64 feet. Neither groundwater nor seepage water encountered.
70						
75						
80						
85						
90						Plate A4.42

APPENDIX B: TECHNIAL SHEET (TENCATE, 2014)

TENCATE Mirafi®

TENCATE GEOSYNTHETICS
Americas

Mirafi® PET70/70

Mirafi® PET70/70 geotextile is composed of high tenacity polyester multifilament yarns which are woven into a stable network such that the yarns retain their relative position. Mirafi® PET70/70 geotextile is inert to biological degradation and resistant to naturally encountered chemicals, alkalis, and acids.

TenCate Geosynthetics Americas is accredited by a2La (The American Association for Laboratory Accreditation) and Geosynthetic Accreditation Institute – Laboratory Accreditation Program (GAI-LAP).

Mechanical Properties	Test Method	Unit	Minimum Average Roll Value	
			MD	CD
Tensile Strength (at ultimate)	ASTM D4595	lbs/ft (kN/m)	4800 (70.0)	4800 (70.0)
Tensile Strength (at 5% strain)	ASTM D4595	lbs/ft (kN/m)	1080 (15.8)	2400 (35.0)
Tensile Strength (at 10% strain)	ASTM D4595	lbs/ft (kN/m)	3360 (49.0)	4800 (70.0)
Creep Reduced Strength	ASTM D5262	lbs/ft (kN/m)	2880 (42.0)	
Long Term Design Strength[1,2]	GRI GT-7	lbs/ft (kN/m)	2280 (33.2)	
Factory Sewn Seam	ASTM D4884	lbs/ft (kN/m)	2400 (35.0)	
Permittivity	ASTM D4491	sec^{-1}	0.10	
Apparent Opening Size (AOS)[3]	ASTM D4751	U.S. Sieve (mm)	40 (0.43)	
UV Resistance (at 250 hours)	ASTM D4355	% strength retained	50	

[1] Machine Direction
[2] Long Term Allowable Design values are for sand, silt and clay
[3] ASTM D4751: AOS is a Maximum Opening Diameter Value
Note: To obtain Secant Modulus, divide tensile strength by the appropriate strain level
(i.e. Secant Modulus at 5% = 1080/0.05=21,600 lb/ft)

Physical Properties	Unit	Typical Value
Roll Dimensions (width x length)	ft (m)	15 x 300 (4.5 x 91.5)
Roll Area	yd^2 (m^2)	500 (418)
Estimated Roll Weight	lb (kg)	234 (107)

Creep Reduced Strength (ASTM D5262), Long Term Design Strength (GRI GT-7), Factory Sewn Seam (ASTM D4884) and UV Resistance (ASTM D4355) are not covered by our current A2LA accreditation.

Made in USA

365 South Holland Drive
Pendergrass, GA 30567

Tel 706 693 2226
Tel 888 795 0808

Fax 706 693 4400
www.tencate.com

FGS000035
ETQM6

TENCATE materials that make a difference

GAI-LAP-25-97

Testing Lab 1291.01 & 1291.02